August Chełkowski Institute of Physics
Faculty of Science and Technology
Doctoral School of the University of Silesia in Katowice

Doctoral Thesis

Measurements of strangeness production in heavy-ion collisions in the NA61/SHINE experiment

mgr Yuliia Balkova

Thesis supervisor:
dr hab. Seweryn Kowalski
Thesis co-supervisor:
dr hab. Szymon Puławski

Chorzów, 2024

Abstract

"Measurements of strangeness production in heavy-ion collisions in the NA61/SHINE experiment"

One of the goals of studying high-energy heavy-ion collisions at facilities such as the Super Proton Synchrotron (SPS), Relativistic Heavy Ion Collider (RHIC), and the Large Hadron Collider (LHC) is to investigate the properties of the quark-gluon plasma (QGP). Particularly, strangeness production in heavy-ion collisions is a long-standing and actively researched topic, offering crucial insights into the properties of strongly interacting matter.

This thesis presents a study of strangeness production in heavy-ion collisions, concentrating on Λ baryon production in central ^{40}Ar+^{45}Sc collisions. The data for this analysis was acquired by the NA61/SHINE experiment at CERN. The analysis was performed for three beam momentum values: 40A, 75A, and 150A GeV/c ($\sqrt{s_{NN}}$ = 8.77, 11.94, and 17.3 GeV, respectively). It is the first measurement of Λ baryon production in ^{40}Ar+^{45}Sc collisions in the SPS energy range.

Λ baryons are neutral particles, thus, they are typically studied via their charged decay products. In this study, Λ baryons are identified by their weak decay channel $\Lambda \longrightarrow p + \pi^-$ with a branching ratio of 63.9%. The analysis is based on reconstructing the invariant mass of particle pairs considered as potential decay products. The results are corrected for losses due to the geometrical acceptance of the detector, reconstruction inefficiency, applied selections, branching ratio, and feed-down from the decays of heavier hyperons, using detailed Monte Carlo simulation. The quality of the results is confirmed by the dedicated checks, e.g., mean lifetime measurement. The main outcomes of this thesis are the double-differential spectra of Λ baryons produced in central Ar+Sc collisions in rapidity-transverse momentum phase space as well as rapidity spectra and mean multiplicities. The obtained experimental results are compared with particle production models and world data from proton-proton and nucleus-nucleus collisions.

Streszczenie

"Pomiar produkcji dziwności w zderzeniach ciężkich jonów w eksperymencie NA61/SHINE"

Głównym celem badań zderzeń ciężkich jonów przy wysokich energiach z wykorzystaniem akceleratorów Super Proton Synchrotron (SPS), Relativistic Heavy Ion Collider (RHIC) oraz Large Hadron Collider (LHC) jest badanie właściwości plazmy kwarkowo-gluonowej (QGP). Produkcja dziwności w zderzeniach ciężkich jonów jest szczególnie ważnym i intensywnie badanym tematem, dostarczającym kluczowych informacji na temat właściwości materii silnie oddziałującej.

Niniejsza praca przedstawia badania produkcji dziwności w zderzeniach ciężkich jonów, koncentrując się na produkcji barionów Λ w centralnych zderzeniach ^{40}Ar+^{45}Sc. Dane wykorzystane w pracy zostały zebrane w ramach eksperymentu NA61/SHINE w CERN. Analiza została przeprowadzona dla trzech pędów wiązki: 40A, 75A oraz 150A GeV/c ($\sqrt{s_{NN}}$ = 8.77, 11.94 oraz 17.3 GeV odpowiednio). Jest to pierwszy pomiar produkcji barionów Λ w zderzeniach ^{40}Ar+^{45}Sc w zakresie energii SPS.

Bariony Λ są cząstkami neutralnymi, dlatego zazwyczaj bada się je opierając się na naładowanych produktach ich rozpadu. W niniejszej analizie bariony Λ są identyfikowane przez ich kanał rozpadu słabego $\Lambda \longrightarrow p + \pi^-$ z prawdopodobieństwem rozpadu wynoszącym 63.9%. Analiza opiera się na studiowaniu rekonstrukcji masy niezmienniczej par cząstek uważanych za potencjalne produkty rozpadu barionu Λ. Wyniki są poprawione na efekty związane z akceptacją geometryczną i niewydajnością rekonstrukcji śladów, selekcją zastosowaną w analizie, prawdopodobieństwem rozpadu oraz na bariony Λ pochodzące z rozpadów cięższych hiperionów, wykorzystując symulacje Monte Carlo. Poprawność analizy została potwierdzona poprzez dodatkowe testy, np. pomiar średniego czasu życia barionu Λ.

Głównymi wynikami tej pracy doktorskiej są podwójnie różniczkowe widma krotności barionów Λ wyznaczone w funkcji pośpieszności oraz pędu poprzecznego, rozkłady pośpieszności oraz średnie krotności barionów Λ. Uzyskane wyniki eksperymentalne są porównywane z wybranymi modelami produkcji cząstek oraz dostępnymi danymi światowymi z zderzeń proton-proton i jądro-jądro.

Contents

Introduction

This thesis presents a study of strangeness production in heavy-ion collisions, concentrating on Λ baryon production in central ^{40}Ar+^{45}Sc collisions. The data analyzed was acquired by the NA61/SHINE experiment at CERN and covers three beam momenta: 40A, 75A, and 150A GeV/c. The study explores Λ baryon production through the measurement of the double-differential spectra in rapidity and transverse momentum phase space, rapidity spectra, and mean multiplicities. Since it is the first measurement of Λ baryon production in a medium-size system like Ar+Sc within the SPS energy range, these results are crucial for understanding the system-size dependence of Λ baryon production properties and their relation to the onset of deconfinement.

The structure of this thesis is organized in the following way. Chapter 1 provides an overview of the Standard Model of particle physics, focusing on the key concepts related to the quark-gluon plasma and the broader motivation of the study. Chapter 2 describes the scientific program and setup of the NA61/SHINE experiment, focusing on the specific configuration utilized for the Ar+Sc data-taking campaign. Chapter 3 explains the analysis procedure used to obtain the results subsequently presented in Chapter 4. Chapter 4 also includes the comparison of obtained results with predictions of selected particle production models and available world data from proton-proton and nucleus-nucleus collisions. Finally, Chapter 5 concludes the thesis with a summary and suggestions for future research.

Author's contribution

I have been an active member of the NA61/SHINE collaboration since 2018, taking on various roles over the years. During numerous data-taking campaigns, I monitored and controlled the data-taking conditions, ensuring smooth operations throughout

the shifts. In most of these campaigns, I was also an on-call beam expert responsible for steering the beam to the experiment and managing the beam counters. Last year, I served as the run coordinator and took charge of offline quality assurance.

I actively participated in the NA61/SHINE upgrade campaign during the Long Shutdown 2 (2018-2022) at CERN. Particularly, I tested the Domino Ring Sampler (DRS) boards at the University of Geneva and participated in the commissioning and maintenance of the DRS system within the experiment. After the upgrade, it acquires data from Beam Counters, Beam Position Detectors, Time-of-Flight detectors, and the Projectile Spectator Detector.

From the analysis point of view, I fully developed the code used for my analysis, implemented all of the methodologies and obtained the results, which is described in Chapters 3 and 4. During the analysis process, I coordinated the so-called V^0 task force, working closely with colleagues at the Rudjer Boskovic Institute in Zagreb to improve the V^0 modules used in the reconstruction chain to identify V^0 particles. Moreover, I performed several data reconstruction campaigns for Ar+Sc data sets and became an integral part of the data reconstruction team, contributing to the broader data analysis efforts within the collaboration. Additionally, I conducted one of the Monte Carlo simulation production campaigns for Ar+Sc collisions.

Beyond my hardware and software work, I briefly participated in the outreach team of the NA61/SHINE experiment, helping to communicate the significance of our research to a wider audience.

Chapter 1

Theoretical overview

1.1 Standard Model of Particle Physics

The *Standard Model* (SM) is a comprehensive theoretical framework that encompasses the description of the properties of the elementary particles and their interactions [1]. The success of the SM predictions has been validated through numerous experimental results, culminating in the discovery of the Higgs boson at the Large Hadron Collider (LHC) at the European Organisation for Nuclear Research (CERN) in 2012 [2, 3].

The SM categorizes the elementary particles into *fermions* (particles with half-integer spin) and *bosons* (particles with integer spin), the former being constituents of matter, and the latter being the force carriers. The experimentally measured properties of the elementary particles, including their mass, electric charge and spin, are summarized in Fig. 1.1.

The SM includes three out of the four fundamental interactions: electromagnetic, weak, and strong. Gravity is described by General Relativity [5] and is yet to be incorporated into the SM. Each of these three interactions is mediated by corresponding spin 1 particles: the electromagnetic force by *photons* (γ), the weak force by W^+, W^- and Z^0 *bosons*, and the strong force by *gluons* (g). The range of the electromagnetic force is infinite, while the weak and strong forces are short-ranged with ranges of about 10^{-18} m and 10^{-15} m, respectively. The short range of the strong force is due to the confinement property, which is introduced later in this section. On the other hand, the short range of the weak interaction is caused by the massive nature of the bosons that mediate the weak interaction: unlike the massless photons and gluons,

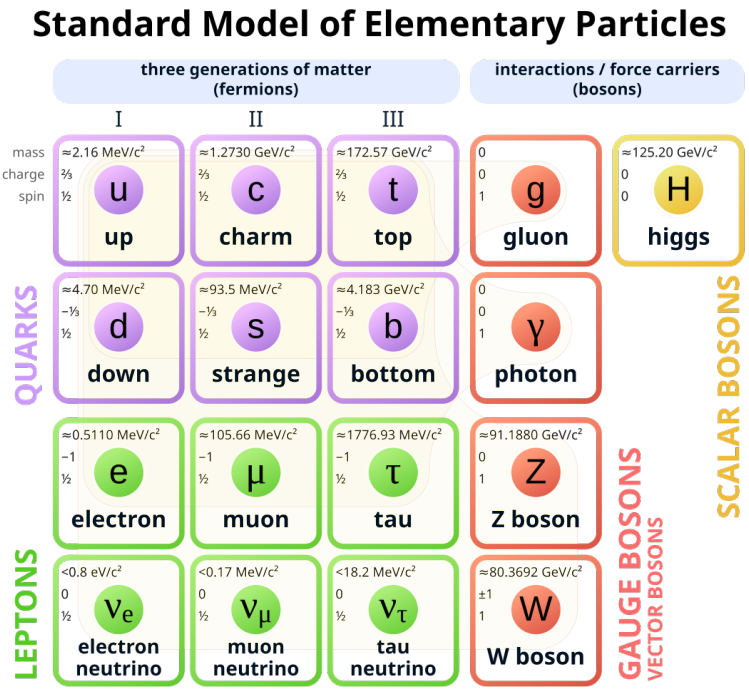

Figure 1.1: Summary of the properties of the elementary particles as described by the Standard Model (figure taken from Ref. [4]).

the W and Z bosons are very heavy and short-lived [6]. At the so-called *Fermi scale* (energy scale around 246 GeV), the electromagnetic and weak interactions are unified within the *electroweak theory* [7–9]. From the theoretical point of view, the consistency of the electroweak theory with the non-zero mass of the W and Z bosons has required the existence of another – spin 0 – boson. It is the *Higgs boson*, which is responsible for the mass generation of most of the fundamental particles through the *Higgs mechanism* [10–12].

Fermions are distinguished into three so-called *generations*, each containing two *quarks* and two *leptons*. Overall, there are six *flavours* of the quarks: up (u), down (d), charm (c), strange (s), top (t), and bottom (b, also referred to as beauty), as well as six flavours of the leptons: electron (e), electron neutrino (ν_e), muon (μ), muon neutrino (ν_μ), tau (τ), and tau neutrino (ν_τ). Each quark and lepton has its matching *antiparticle* with the same mass and spin but inverted charges of the fundamental interactions (such as the electric charge). Quarks participate in all known fundamental interactions, while leptons do not participate in the strong interaction. Additionally, neutrinos do not participate in electromagnetic interaction as they are electrically

neutral.

The electromagnetic and strong interactions conserve the flavours of quarks and leptons. In contrast, the weak interaction allows certain transitions that do not conserve the flavour. The *"charged"* weak interaction (mediated by the charged W bosons) couples *up-type* fermions to their *down-type* counterparts, i.e. up quarks to down quarks or charged leptons to neutrinos. It is also responsible for the fact that the heavy quarks and charged leptons of the second and third generations are unstable and eventually decay to their first-generation counterparts. Instead, the *"neutral"* weak interaction (mediated by the Z boson) conserves the flavour. Importantly, "charged" weak interaction has non-zero couplings between the three generations of quarks. The coupling strength of a given up-type quark to a given down-type quark is given by the unitary 3×3 Cabibbo-Kobayashi-Maskawa (CKM) matrix [13, 14]. It has nine matrix elements V_{ij}, where $i = (u, c, t)$ and $j = (d, s, b)$. The probability of a transition between a quark of a type i and a quark of a type j is proportional to the squared matrix element $|V_{ij}|^2$. The diagonal elements of this matrix (V_{ud}, V_{cs} and V_{tb}) describe the coupling between the two quarks within the same generation, and their values are experimentally found to be close to unity, e.g. $|V_{ud}| = 0.97367 \pm 0.00032$ [6]. At the same time, the off-diagonal elements that link the quarks of different generations are small but non-zero. For example, the absolute value of the matrix element that describes the coupling of u and s quarks is $|V_{us}| = 0.22431 \pm 0.00085$ [6]. The non-zero value of the off-diagonal matrix elements allows the transition between quark generations; however, such transitions are suppressed. It means that, for instance, the strange quark cannot decay into the charm quark, a member of the same generation, due to energy conservation. However, a decay of the strange quark into the up quark is allowed, although with a suppression due to the off-diagonal transition.

For what concerns the strong interactions between quarks, they are described by the *Quantum Chromodynamics* (QCD). QCD introduces the concept of *colour charge*, which is equivalent to an electric charge in Quantum Electrodynamics (QED). Each quark carries a quantum number called "colour" that can take one of the three values (red, green or blue); similarly, antiquarks carry one of the corresponding anti-colours (anti-red, anti-green or anti-blue). Furthermore, gluons carry a pair of colour and anti-colour, which results in an important difference between the QCD and QED: the self-interaction of gluons due to their non-zero colour charge, in contrast to photons that do not directly interact with other photons due to their zero electric charge.

The values of the so-called *effective coupling constant* α_s, which expresses the strength of the interaction, depend on the four-momentum transfer Q^2 in such interaction process, as illustrated in Fig. 1.2. The α_s becomes large at small values of transferred momenta (corresponding to large distances), which is responsible for *quark confinement*. It explains the fact that the quarks and gluons cannot be observed as individual particles but are instead confined within colourless bound states – *hadrons*. The colourless state can be achieved either by binding together pairs of quarks and antiquarks, colours of which cancel each other (*mesons*), or a set of three quarks of three different colours (baryons). Recently, there was also found experimental evidence for exotic states, which are more complicated colourless combinations of quarks and antiquarks, such as *tetraquarks* (two quarks and two antiquarks, e.g. [15, 16]) and *pentaquarks* (four quarks and one antiquark, e.g. [17, 18]). The protons and neutrons, bound states of the first-generation quarks, along with electrons and neutrinos, account for the stable matter in the Universe. At the same time, as the value of transferred momentum increases (corresponding to short distances), α_s decreases, allowing quarks to behave almost as free particles at high energies, which is known as *asymptotic freedom*.

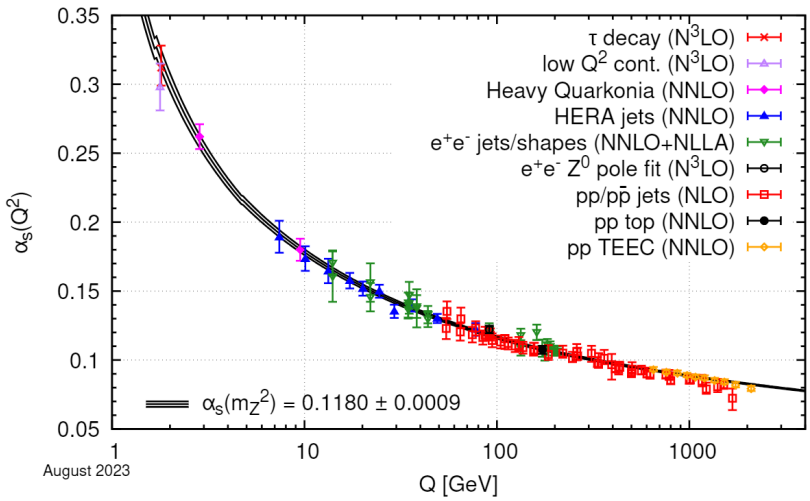

Figure 1.2: Summary of the measurements of strong coupling constant α_s as a function of energy scale Q compared to current PDG average (figure taken from Ref. [6]).

1.2 Quark-gluon plasma in heavy-ion collisions

At sufficiently high energies, quarks and gluons are no longer confined within hadrons, which leads to the formation of a new, deconfined phase of nuclear matter – *quark-gluon plasma* (QGP) [19, 20]. The existence of the latter was experimentally confirmed by experiments conducted at the European Organization for Nuclear Research (CERN) [21, 22] and Brookhaven National Laboratory (BNL) [23–26]. The study of QGP properties is strongly motivated by the assumption that this state existed in the very early Universe – about $10^{-12} - 10^{-6}$ seconds after the Big Bang, and during the expansion and cooling of the Universe, a transition to the confined hadronic phase occurred [27]. Moreover, this research has implications for neutron star studies, as it has been suggested that the extreme densities in the core of neutron stars could lead to the formation of QGP [19].

As for any type of matter, there are specific conditions under which a phase transition would occur. In the case of strongly interacting matter, these are summarized in the QCD phase diagram schematically illustrated in Fig. 1.3 in terms of the temperature T and baryon chemical potential μ_B. The latter is the energy required to create a given excess in the number of quarks over the number of antiquarks.

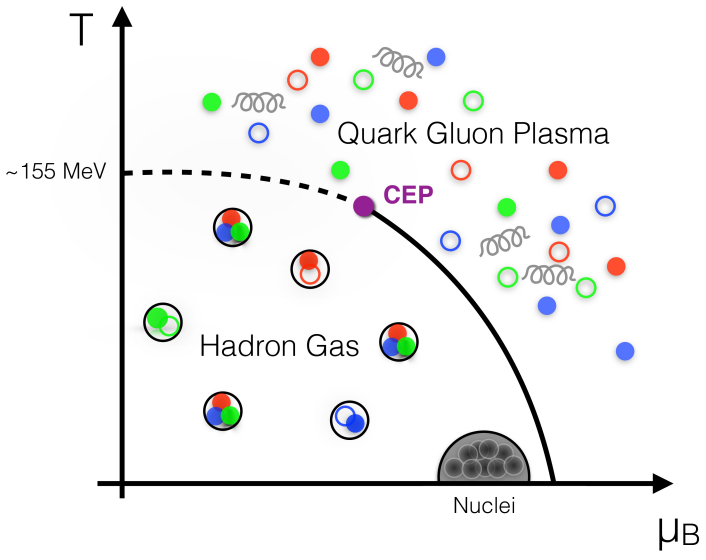

Figure 1.3: A schematic QCD phase diagram in terms of the baryon chemical potential μ_B and temperature T (figure taken from Ref. [28]). The solid line indicates the first-order phase boundary between the hadron gas and quark-gluon plasma phases, which may end in a critical endpoint CEP. At point CEP, the phase transition turns into a crossover, shown as the dotted line.

Numerical QCD calculations indicate that at values of μ_B close to 0, the phase transition is a crossover [29], meaning that the transition between phases occurs gradually as the temperature changes. It should then transform into a first-order phase transition for higher μ_B values, leading to the presence of a critical end point (marked in Fig. 1.3 as CEP), although its exact position is not yet established neither theoretically nor experimentally [30].

Naturally, the creation of QGP in a laboratory is a necessity in order to study its properties systematically in a controlled environment. Relativistic heavy-ion collisions offer this opportunity, considering that the critical temperature and the energy density required for the QGP formation are recreated. The theoretically established evolution of the heavy-ion collision for this case is schematically illustrated in Fig. 1.4.

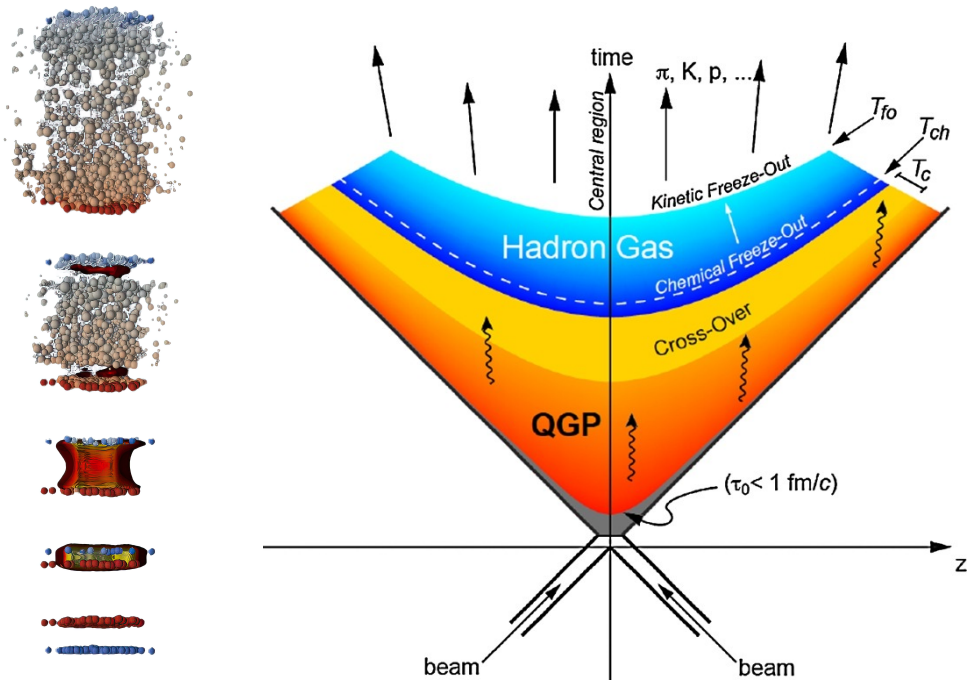

Figure 1.4: A schematic diagram of a heavy-ion collision evolution in case of quark-gluon plasma formation (figures taken from Ref. [31] (*left*) and Ref. [32] (*right*)). The evolution begins with a hot pre-equilibrium fireball, progressing through the formation of a quark-gluon plasma (QGP), and eventually undergoing a crossover phase transition into a hadron gas. Throughout this process, the fireball emits various particles (shown by arrows), passing through key temperature stages: T_c (critical temperature), T_{chem} (chemical freeze-out temperature), and T_{kin} (kinetic freeze-out temperature) – see text for further details.

Two Lorentz-contracted ions collide, creating a so-called *fireball* filled with quarks and gluons. Its expansion serves as the primary cooling mechanism, and once the temperature reaches the pseudo-critical temperature T_c, the *hadronization* process begins; thus, QGP and created hadrons coexist briefly in a mixed phase. As the temperature drops further to T_{chem}, the inelastic interactions between particles stop, and hadron production yields become settled, which is known as *chemical freeze-out*. Following this, the system enters the hadronic phase, where particles undergo elastic interactions that continue until *kinetic freeze-out* at the corresponding temperature T_{kin}, and after that, the hadrons propagate to the detectors with fixed momenta. The exact values of all the temperatures mentioned above are unknown and depend on the model.

The study of the hadron production dependence on the collision system size allows to investigate the nature of particle production mechanisms, including potential contributions from QGP formation. Particularly, it is useful to consider the heavy-ion collision as a superposition of individual nucleon-nucleon collisions the way it is done within the Wounded Nucleon Model (WNM) [33]. In this model, as shown in Fig. 1.5, the nuclei proceed towards each other with the distance between the trajectories of their respective geometrical centres defined by an impact parameter b. If the value of b is small, then the collision is labelled as *central*, contrary to a *peripheral* collision, where the impact parameter has a large value. The nucleons that interact during the collision are called *participants*, while non-interacting ones are known as *spectators*. Moreover, the nucleons that take part in inelastic interactions, are referred to as *wounded nucleons*. Their corresponding quantities N_{part}, N_{spec}, and N_W (in literature also $\langle W \rangle$) can be calculated from such geometry-defining parameters as the impact parameter and atomic masses of colliding nuclei in addition to the nucleon-nucleon interaction cross-sections. Importantly, for some fixed-target experiments, the number of spectators related to the projectile nucleus is estimated based on the measurements by the hadron calorimeter, and thus, the collision centrality can be evaluated.

Crucially, within the WNM, it is possible to roughly estimate the multiplicity (i.e. number) of particles of a given kind produced in a heavy-ion collision knowing the corresponding multiplicity in a proton-proton collision using the formula:

$$n_{A+A} = \frac{1}{2} \cdot N_W \cdot n_{p+p} \,, \tag{1.1}$$

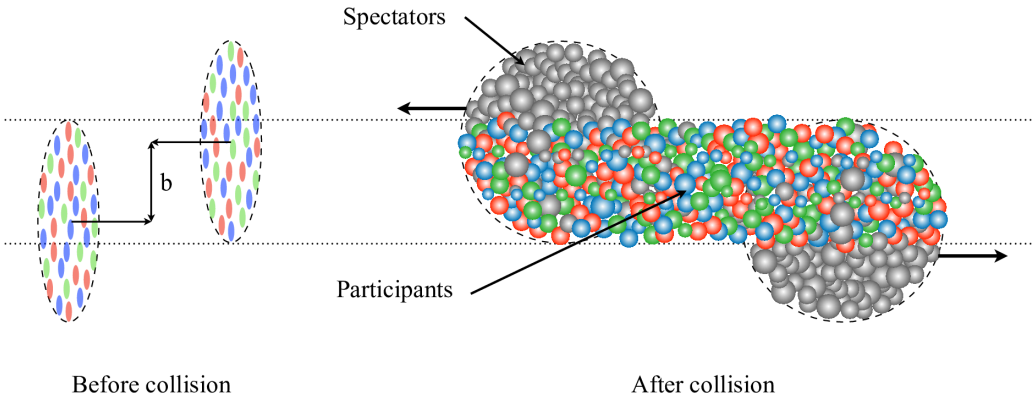

Figure 1.5: A geometrical view of a heavy-ion collision (figure taken from Ref. [34]). The impact parameter b is shown along with spectator and participant nucleons.

where n_{A+A} and n_{p+p} are the respective multiplicities of a given particle produced in nucleus-nucleus (A+A) and proton-proton (p+p) collisions, and N_W is the mean number of wounded nucleons in the nucleus-nucleus collision. WNM with its statistical approach remains a valuable reference for understanding particle production in nucleus-nucleus collisions.

1.3 Strangeness enhancement as a quark-gluon plasma signature

One may rightfully ask whether QGP forms in every heavy-ion collision. Since, among other reasons, it is impossible to directly access the fireball due to its short lifetime ($\sim 10^{-22}$ seconds), it is crucial to establish a set of QGP *signatures* – observables that are minimally affected by hadronization and can provide insight into the properties of the QGP. Moreover, these signals ought to be distinguished from the backgrounds produced in the hot hadronized phase as well as final-state interactions. Nonetheless, as a result of extensive theoretical efforts, such observables were identified, with the *strangeness enhancement* being one of the first to be proposed [35–37].

According to those, the idea of strangeness enhancement is based on the consideration that in the case of the QGP formation, strangeness is easily created through the pair production of strange and anti-strange quarks. The fundamental processes

involved are the fusion of two gluons (g) or two light quarks (q):

$$\begin{aligned} g + g &\rightarrow s\bar{s}, \\ q + \bar{q} &\rightarrow s\bar{s} \quad (q = u, d). \end{aligned} \tag{1.2}$$

These reactions occur at a much lower energy cost in QGP than in hadronic collisions. The energy threshold for strangeness production in a QGP is about two masses of strange quark: $2m_s \approx 200$ MeV, while in hadronic reactions, it is around 670 MeV due to the limitation to the production of hadrons such as kaons and Λ baryons. Because of this, when QGP forms, strange quarks can be produced abundantly and quickly, leading to an enhancement in the production of strange hadrons, particularly multi-strange baryons (such as Ξ and Ω) and their antiparticles, compared to what is seen in p+p or p+A collisions [35, 36].

Numerous experiments have observed enhanced strangeness production in A+A collisions with respect to p+p and p+A collisions. Early experiments at AGS and SPS focused on particles with a single strange quark (i.e. kaons, Λ, $\bar{\Lambda}$) in smaller collision systems involving oxygen, sulphur and gold nuclei. These measurements established an enhancement of kaon and Λ production relative to pions, compared to p+p and p+A collisions [38–40]. Following these initial findings, the experiments shifted towards the measurement of multi-strange (anti-)baryons in S+A and p+A collisions, which allowed to confirm the Ξ baryon production enhancement [41]. Eventually, studies with lead beams by the experiments at SPS systematically explored this effect.

Fig. 1.6 illustrates the system size dependence of the strangeness enhancement for baryons and antibaryons as measured by the NA57 experiment in lead-lead collisions [42]. Here, the strangeness enhancement is defined as the ratio of mid-rapidity yields per participant nucleon for Pb+Pb and p+Be collisions. One can observe a distinct hierarchy of the enhancements: the higher the strangeness content of the baryon, the stronger the enhancement. It has been argued that this behaviour is consistent with the formation of QGP and, at the same time, is difficult to explain using hadron transport models.

In turn, Fig. 1.7 shows the energy dependencies of the ratio of the mean multiplicities of kaons and pions and the strangeness enhancement factor E_S as observed by NA49

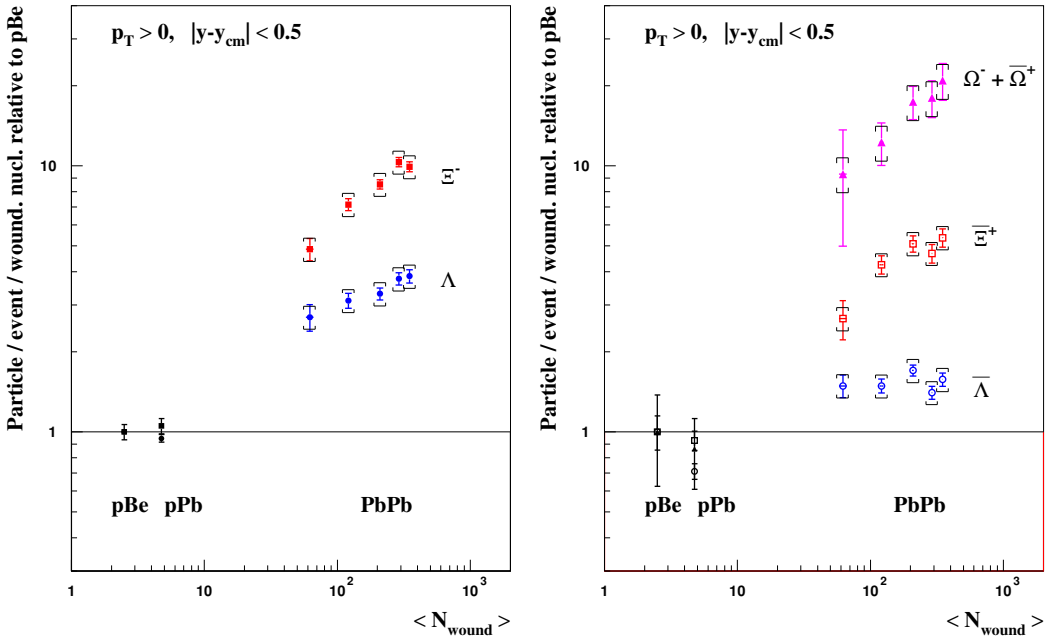

Figure 1.6: Strangeness enhancement for baryons (*left*) and antibaryons (*right*) measured by the NA57 experiment in Pb+Pb collisions as a function of the number of wounded nucleons (figure taken from Ref. [42]). The normalized yields for p+Be and p+Pb data are consistent within error limits in agreement with N_W scaling, and Pb+Pb data show significant centrality dependence of enhancements for all particles except for $\bar{\Lambda}$. This behavior is argued to be consistent with QGP formation.

experiment in lead-lead collisions [43]. In this case, the factor E_S is defined as

$$E_S = \frac{\langle \Lambda \rangle + \langle K + \overline{K} \rangle}{\langle \pi \rangle} \,, \tag{1.3}$$

where $\langle \Lambda \rangle$, $\langle K + \overline{K} \rangle$, and $\langle \pi \rangle$ are the mean multiplicities of Λ baryons, charged and neutral kaons, and pions, respectively. A sharp maximum in both quantities at SPS energies can be seen, followed by a plateau for RHIC energies, contrary to the results from p+p collisions, where no peak is found. According to the Statistical Model of the Early Stage (SMES) [44], a transition to QGP occurs when the critical temperature T_c is reached, which results in a characteristic drop in the strangeness-to-entropy ratio as seen in the experimental data.

Recent studies indicate that certain phenomena associated with heavy-ion collisions, particularly strangeness enhancement, can also occur in high-energy high-multiplicity

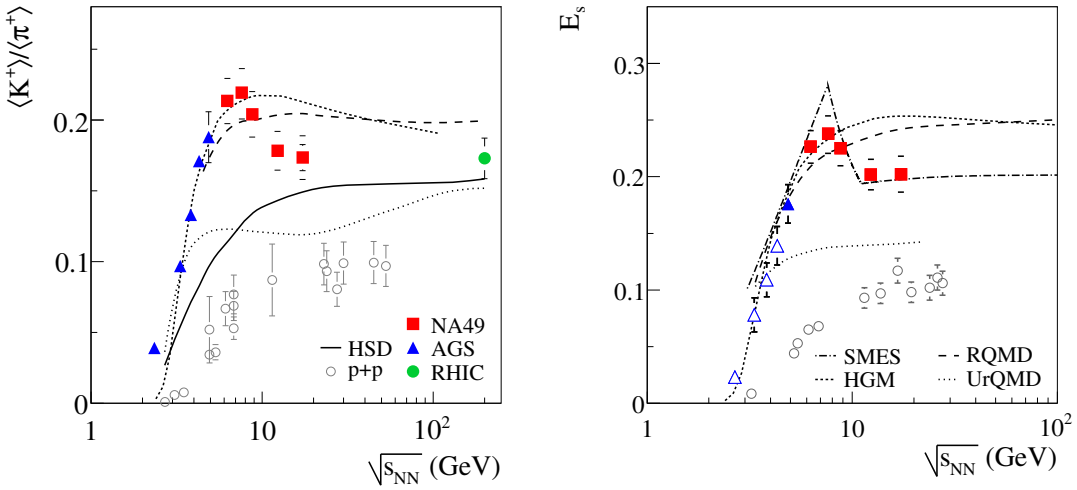

Figure 1.7: Energy dependence of $\langle K^+ \rangle \langle \pi^+ \rangle$ ratio (*left*) and strangeness enhancement E_S (*right*, as defined by Eq. 1.3) observed by the NA49 experiment in Pb+Pb collisions (figures taken from Ref. [43]). Both quantities exhibit a sharp maximum at SPS energies, followed by a plateau towards RHIC energies, unlike p+p collisions, which show no peak. This behaviour is suggested to be compatible with transition to QGP.

p+p collisions [45]. It has been consequently suggested that QGP formation depends on the entropy content of the system, which is related to hadron multiplicity, rather than its size [46].

Continuation of the study of strangeness enhancement in medium-sized collision systems appears to be crucial for further understanding of how the system size influences the observed enhancement. Medium-size systems bridge the gap between small p+p and large Pb+Pb systems, and yet, the present data is rather scarce. Furthermore, these studies serve as valuable tests for theoretical models, helping to distinguish between initial-state effects and the collective properties of QGP.

Chapter 2

NA61/SHINE experiment

The data from ^{40}Ar+^{45}Sc collisions, analyzed in this thesis, was acquired by the fixed-target experiment NA61/SHINE at CERN. It is a fixed-target experiment located at the H2 beamline of the North Area of CERN. The acronym stands for **S**PS **H**eavy **I**on and **N**eutrino **E**xperiment. The scientific interests of the experiment is quite broad and includes charged and neutral hadron production measurements for three different programs.

The program on strong interactions physics aims to study the QCD phase diagram through a two-dimensional scan of phase space in the beam momentum and the system size, as shown on the left panel of Fig. 2.1. This scan includes data on p+p, Be+Be, Ar+Sc, Xe+La, and Pb+Pb collisions, at beam momenta ranging from 13A to 150A GeV/c.The selection of projectile and target nuclei was determined by the CERN accelerator chain capabilities and the physico-chemical properties of the materials. As can be seen on the right panel of Fig. 2.1, the collected data covers a significant portion of the QCD phase diagram. The chemical freeze-out temperatures for available data were estimated using the hadron gas model [47].

Apart from heavy-ion-related activities, the experiment provides crucial reference measurements for neutrino and cosmic rays physics. The neutrino physics program covers analyses of proton-nucleus collisions to allow the calculation of the beam composition and initial neutrino fluxes for experiments at J-PARC and Fermilab facilities [48–51]. The cosmic-ray physics program focuses on hadron-nucleus collisions to improve the modelling of cosmic ray showers [52–55], and measurements of nuclear fragmentation cross-sections for the development of primary cosmic ray prop-

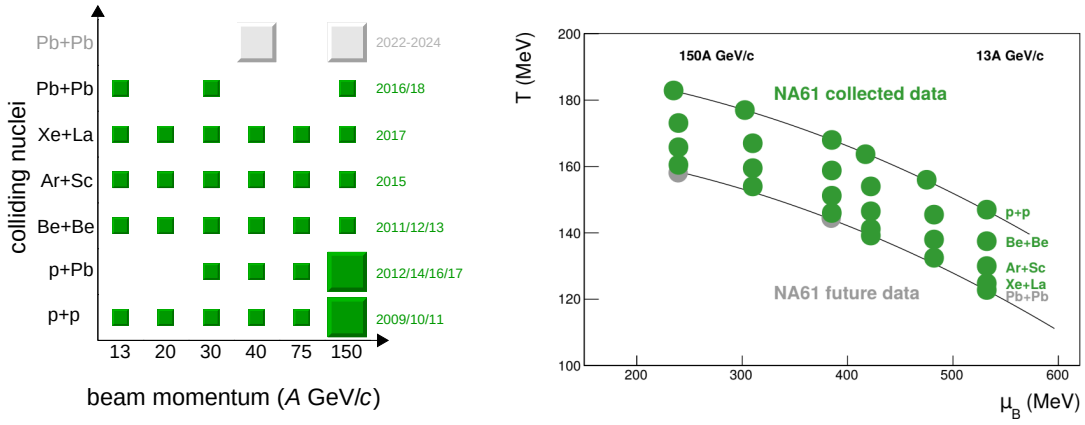

Figure 2.1: *Left*: summary of the two-dimensional scan in collision energy and system size, performed by the NA61/SHINE experiment. Green indicates already collected data, while grey marks data that has been taken recently or will be taken in the future. Box size reflects statistics of collected data. *Right*: region of the QCD phase diagram covered by NA61/SHINE measurements, with chemical freeze-out temperatures estimated using the hadron gas model [47].

agation models [56, 57].

The next section, Sec. 2.1, gives a general overview of the NA61/SHINE experimental setup during Ar+Sc data taking. Further two sections, Sec. 2.2 and 2.3, describe the beam acceleration chain and target used during the data taking. Sec. 2.4 focuses on the detector subsystems crucial for performing the analysis presented in this thesis, namely, the detectors included in the trigger system as well as the Time Projection Chambers. The information from these detectors is used for the event and track selection criteria described in Chapter 3.

2.1 Overview of experimental setup

A schematic layout of the NA61/SHINE detector during Ar+Sc data taking along with the utilized coordinate system is shown in Fig. 2.2. The coordinate system is a right-handed Cartesian system with its origin at the centre of the second vertex magnet (for historical reasons). The z-axis aligns with the beamline, the x-axis is horizontal, and the y-axis is vertical, pointing upward. A thorough description of the detector setup can be found in Ref. [58].

The major part of the detector setup is a set of four large-volume Time Projection

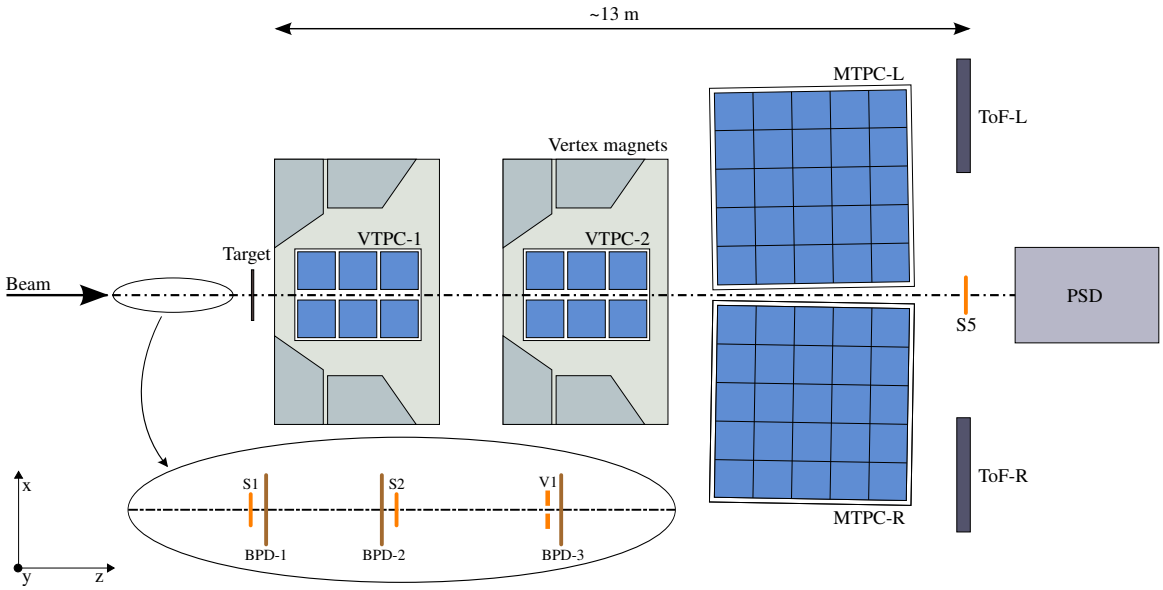

Figure 2.2: A schematic layout of the NA61/SHINE experiment [58] showing the detector components used during Ar+Sc data taking. The beam instrumentation is presented in the inset. The chosen coordinate system is shown in the bottom left corner: the incoming beam direction follows the z-axis, with the magnetic field bending charged particle trajectories in the horizontal $x - z$ plane, while the drift direction in the TPCs aligns with the vertical y-axis.

Chambers (TPCs) labelled VTPC-1, VTPC-2, MTPC-L, and MTPC-R. Two chambers, VTPC-1 and VTPC-2, are placed inside two superconducting magnets downstream of the target. Two other chambers, MTPC-L and MTPC-R, are positioned downstream of the VTPC-2. Additionally, two Time-of-Flight detectors, ToF-L and ToF-R, are situated behind the MTPCs. The setup is also equipped with the Projectile Spectator Detector (PSD), a high-resolution forward hadron calorimeter.

2.2 Beam

The NA61/SHINE experiment utilizes the beams delivered by the CERN accelerator complex. Specifically, the heavy ion acceleration chain is indicated in Fig. 2.3 by dark grey arrows.

It commences with the Electron Cyclotron Resonance (ECR) ion source, where the ions are generated and accelerated to the energy of 2.5A keV. During the next stage, the ions undergo acceleration by the Radio-Frequency Quadrupole (RFQ) and reach

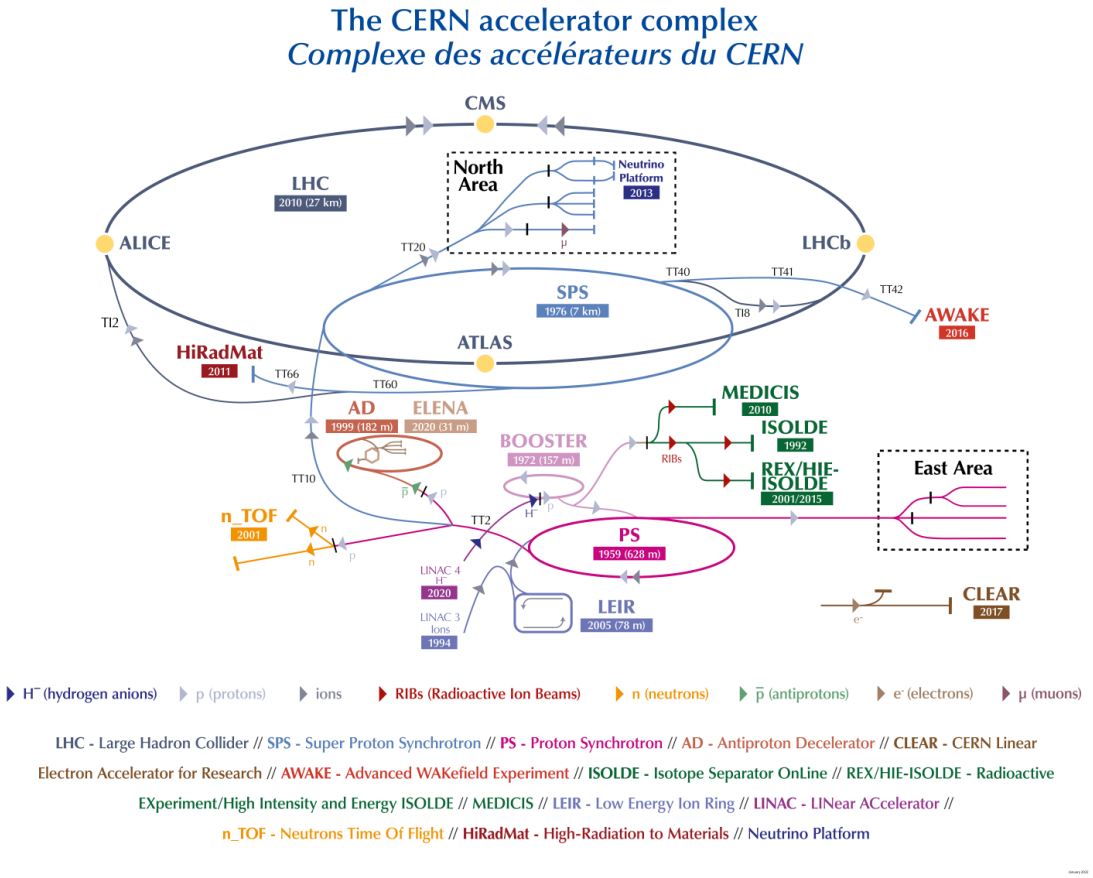

Figure 2.3: The CERN accelerator complex as of 2022 (not to scale) [59].

the energy of 250A keV. Afterwards, the ions enter the LINAC3 linear accelerator, where the ion energy is brought up to 4.2A MeV. The ion beam is then injected into the Low Energy Ion Ring (LEIR), which accelerates ions to the energy of 72A MeV. Later, the ions are extracted towards the Proton Synchrotron (PS), where they are accelerated to the energy 5.9A GeV and fully stripped by 1 mm thick aluminium foil. Finally, the ions are injected into the Super Proton Synchrotron (SPS). The SPS delivers beams in a wide ion beam energy range between 13A GeV and 160A GeV. The lower limit for beam momentum is determined by beam stability and quality, while the capabilities of the beamline magnets constrain the upper limit. After that, the beam is directed to the H2 secondary beamline, which leads to the NA61/SHINE experiment, as shown in Fig. 2.4. It consists of bending dipole and focusing quadrupole magnets along with collimators and beam detectors. The collimators allow for restricting the transverse size of the beam and adjusting its intensity. The beam detectors along the beamline are used to monitor the beam position and beam spot size.

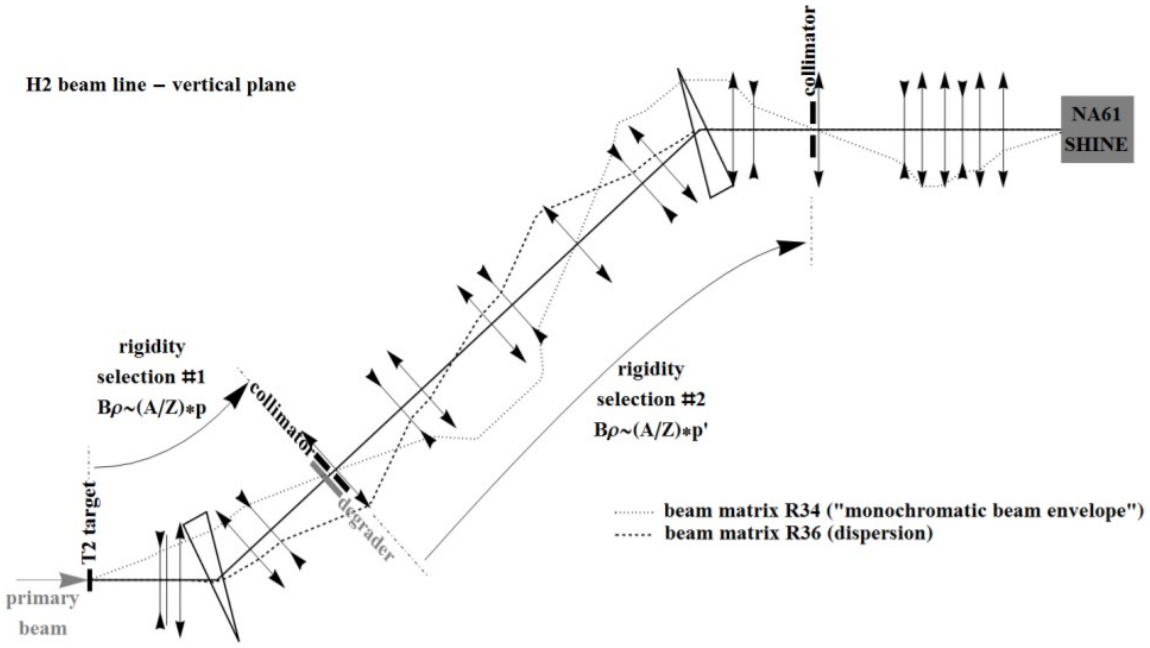

Figure 2.4: Schematic view of the vertical plane of the H2 beamline (not to scale) [58]. The arrows correspond to the beamline magnets, and the dotted line shows the calculated beam trajectory.

Initially limited to primary lead ions, CERN initiated a new project [60] aiming at the delivery of primary ion beams to fulfil the experimental demands, particularly for ^{40}Ar beams [61]. After successful preparation and commissioning [62], the argon run took place in early 2015.

2.3 Target

The experimental target consisted of six plates of ^{45}Sc, each with 2x2 cm^2 area and 1 mm thickness. It was at $z = -580$ cm of the NA61/SHINE coordinate system within a dedicated helium box, which serves to reduce off-target interactions with air. The target composition was measured using the Wavelength Dispersive X-Ray Fluorescence (WDXRF) technique at Jan Kochanowski University in Kielce. It was found to have 99.29% purity with minor contaminants, such as Ti (0.157%), Al (0.144%), Fe (0.130%) and others (totalling 0.279%). The influence of target impurities on multiplicity distributions was analyzed using simulation tools. The effect was estimated to be less than 0.2% [63] and, therefore, was neglected as a contribution to total sys-

tematic uncertainty.

The data were collected with two target configurations: with the target inserted (target IN) and with the target removed (target OUT). Around 90% of the total dataset was acquired with the target IN configuration. Target OUT data were taken to account for off-target interactions of beam ions.

2.4 Detector

2.4.1 Beam detectors and trigger system

The beam instrumentation of the experiment, shown in the inset of Fig. 2.2, is used to determine the charge, position and timing of incoming beam particles. Throughout the Ar+Sc taking, this group of detectors included scintillator detectors S1 and S2, a veto scintillator detector V1, along with beam position detectors BPD-1, BPD-2, and BPD-3. All mentioned beam detectors were located upstream of the target to define the beam parameters, while an additional scintillating detector, S5, was positioned downstream and used as the interaction detector. The parameters of these detectors are outlined in Table 2.1.

Table 2.1: Summary of the parameters of the beam detectors used during Ar+Sc data taking. Positions are given in the NA61/SHINE coordinate system.

detector	dimensions [mm]	hole [mm]	z position [m]
S1	$60 \times 60 \times 2$		–36.42
S2	$40 \times 40 \times 2$		–14.42
V1	$\varnothing = 100 \times 10$	$\varnothing = 10$	–6.72
S5	$\varnothing = 20 \times 1$		9.80
BPD-1	$48 \times 48 \times 32.6$		–36.20
BPD-2	$48 \times 48 \times 32.6$		–14.90
BPD-3	$48 \times 48 \times 32.6$		–6.70
Target			–5.80

A telescope of three Beam Position Detectors (BPDs) is responsible for the trajectory measurement of the incoming beam particles, to enable the reconstruction of the main interaction vertex. These detectors are proportional chambers filled with a mixture of 85% Ar and 15% CO_2. Each detector consists of two planes of orthogonal readout strips, allowing the position measurement of beam particles in the $x - y$

plane.

To identify and record events of interest for further analysis, the trigger systems are typically employed. The detectors used in the trigger system during Ar+Sc data taking are shown in Fig. 2.5. The detectors marked in green were used in coincidence, while those in red were utilized in anti-coincidence mode. Four trigger configurations were set during this data taking: *beam* trigger, *central interaction* trigger, *beam halo* trigger, and *minimum bias interaction* trigger. The trigger definitions are summarized in Table 2.2 and remained consistent throughout the entire data taking period.

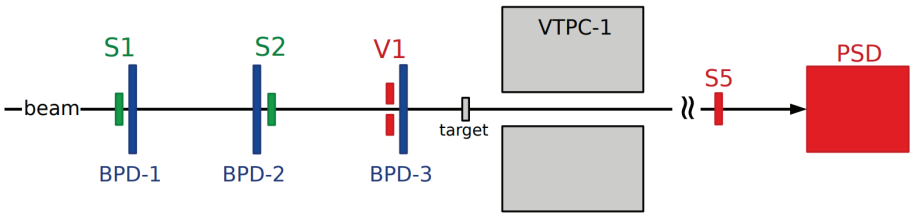

Figure 2.5: A schematic layout of the beam and trigger detectors used during Ar+Sc data taking (horizontal cut in the beam plane, not to scale) [64]. Subdetectors marked in green were used in coincidence, while those marked in red were utilized in anti-coincidence mode in the trigger logic.

Table 2.2: Summary of the trigger definitions used during Ar+Sc data taking.

name	definition	description	fraction of data
T1	$S1 \cdot S2 \cdot \overline{V1}$	beam	1.16%
T2	$S1 \cdot S2 \cdot \overline{V1} \cdot \overline{S5} \cdot \overline{PSD}$	central interaction	92.61%
T3	$S1 \cdot S2$	beam halo	0.18%
T4	$S1 \cdot S2 \cdot \overline{V1} \cdot \overline{S5}$	minimum bias interaction	7.13%

The last column presents the fraction of data corresponding to an unbiased sample of a specific trigger configuration. Most of the recorded data consists of central interaction triggers, with a small amount collected with beam and minimum bias triggers, primarily for monitoring and cross-section analysis. The sum of all fractions exceeds 100%, as, for instance, some T1 triggers also fall under the group of T2 triggers.

The S1 and S2 detectors are the two first scintillator detectors on the beamline. The S1 detector is equipped with four photomultiplier tubes (PMT) attached perpendicularly to the beam trajectory on each side of the scintillator. It allows for a precise timing measurement irrespective of the beam position. The trigger logic always uses the S1 and S2 signals in coincidence to identify beam particles, which cross both de-

tectors. The next scintillator detector on the beamline is veto scintillator detector V1, which has a hole in the middle. It is used in anti-coincidence (veto) mode in the trigger logic, which allows triggering on the central part of the beam, eliminating the beam halo and products of beam interaction with beamline elements. The last scintillator detector on the beamline, S5, is positioned downstream of the target. In the event of a beam particle interaction, no Ar beam signal is registered in S5, so the S5 signal is used in the trigger logic in anti-coincidence mode.

The Projectile Spectator Detector (PSD) is the last detector along the beamline, placed downstream of MTPCs and centred in the transverse plane on the deflected position of the beam. It is a zero-degree hadron calorimeter, which measures the energy deposit of projectile spectators, i.e. non-interacting nucleons. In more *central* events, spectators carry less energy, thus, less energy is deposited in the PSD. Therefore, it allows the *centrality* selection of the collisions by imposing an upper limit on the measured forward energy.

The schematic layout of the PSD front view is shown in the left panel of Fig. 2.6. The detector includes 44 modules, of which the central part contains 16 modules with a transverse size of 10 $\times$ 10 cm^2, while the outer part consists of 28 modules with a transverse size of 20 $\times$ 20 cm^2. The single module, illustrated in the right panel of Fig. 2.6, consists of 60 pairs of 16 mm thin lead plates and 4 mm thin scintillator plates, with a total longitudinal length of 120 cm.

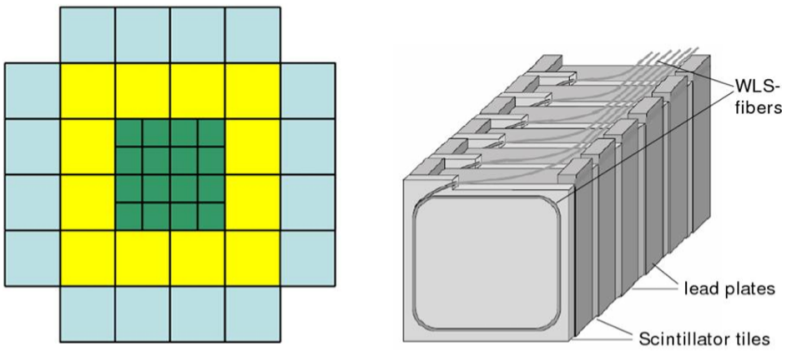

Figure 2.6: Left: a schematic layout of the PSD front, right: a schematic layout of a single PSD module [58].

During the data taking, the summed signal from 16 central modules was used in the T2 trigger configuration (see Table 2.2) for online identification of the most central interactions. Furthermore, the measured forward energy was utilized in the analysis

to select the 10% most central Ar+Sc collisions as explained in Chapter 3.

2.4.2 Time Projection Chambers

The key element of the detector setup is a set of four large-volume Time Projection Chambers (TPCs): VTPC-1, VTPC-2, MTPC-L, and MTPC-R. The essential parameters of the listed chambers are summarized in Table 2.3.

Table 2.3: Summary of the parameters of the Time Projection Chambers used during Ar+Sc data taking.

	VTPC-1	VTPC-2	MTPC-L/R
size $(L \times W \times H)$ [cm]	$250 \times 200 \times 98$	$250 \times 200 \times 98$	$390 \times 390 \times 180$
gas mixture	Ar/CO_2 (90/10)	Ar/CO_2 (90/10)	Ar/CO_2 (95/5)
drift length [cm]	66.60	66.60	111.74
drift voltage [kV]	13	13	19
number of sectors	2×3	2×3	5×5
number of padrows	72	72	90
number of pads/TPC	26886	27648	63360

Two Vertex TPCs (VTPC-1 and VTPC-2) are positioned downstream of the target inside superconducting magnets with a maximum total bending power of 9 Tm. The magnetic field in both magnets points down, causing trajectories of positively and negatively charged particles produced during the interaction to bend toward the $+x$ and $-x$ direction (see Fig. 2.2), respectively. Measuring the track curvature allows to determine particle momentum and the sign of its charge. The Main TPCs (MTPC-L and MTPC-R) are the largest chambers positioned symmetrically on each side of the beamline downstream of VTPC-2. The MTPCs are designed to provide precise specific energy loss ($\mathrm{d}E/\mathrm{d}x$) measurements with high resolution for accurate particle identification. More information on particle identification in this analysis is available in Chapter 3.

Chapter 3

Analysis procedure

This chapter summarizes the analysis workflow, which was used to obtain the results on Λ baryon production in central Ar+Sc collisions at 40A, 75A, and 150A GeV/c ($\sqrt{s_{NN}}$ = 8.77, 11.94, and 17.3 GeV, respectively).

The chapter begins with a brief description of the reconstruction chain and the simulation procedure (Sec. 3.1). Then, the event, track and candidate selection criteria are discussed in Sec. 3.2 and 3.3. The signal extraction method is subsequently described (Sec. 3.4), followed by the selection criteria optimization procedure (Sec. 3.5). Afterwards, the calculation of corrected yields, including the correction factors based on Monte Carlo simulated data, together with the statistical uncertainties, is explained in Sec. 3.6. Sec. 3.7 details calculating the systematic uncertainties. Finally, the quality checks made to ensure the accuracy of the analysis procedure are covered in Sec. 3.8. The analysis results are presented in Chapter 4.

3.1 Data processing and Monte Carlo simulations

Before the analysis, the collected data undergoes calibration and reconstruction. The data is arranged in the form of *events*, each representing a single collision, and includes digitized signals from all subsystems of the detector setup. The data before any manipulation is referred to as *raw* data. The reconstruction chain converts the raw signals to the particle trajectories and their associated properties.

The detector effects, such as its geometrical acceptance and reconstruction efficiency, are corrected for during the analysis using Monte Carlo simulated data (for details,

see Sec. 3.6). This section gives a brief description of both the reconstruction chain and the Monte Carlo simulation procedure.

3.1.1 Reconstruction chain

The reconstruction chain consists of several consecutive steps, typically corresponding to a particular subdetector: BPD, TPC, TOF, and PSD. Additionally, the fitting of the vertices is performed.

Firstly, the BPD reconstruction is conducted. The positions of the beam ions measured by three BPDs in $x - y$ plane are retrieved from the raw data. These points are fitted with a straight line to determine the trajectory of the beam ions.

Afterwards, the reconstruction of the tracks in the TPC volumes is done. Firstly, the TPC pads and time slices are checked for signal quality. If signals are found in neighbouring pads and time slices, this group of signals is connected and marked as a cluster. The cluster position is determined using the centre of gravity method with charges as weights.

Afterwards, the clusters situated close to one another are combined into the *local* track fragments separately in each TPC. Due to the magnetic field presence, the tracks in VTPCs are required to be curved, contrary to straight tracks in MTPCs. Once straight tracks in the MTPCs are identified assuming they originate from a fixed main vertex, they are extrapolated backwards to search for corresponding clusters in the VTPCs. If no match is found, the MTPC clusters are released for future use. Subsequently, local tracks in the VTPCs are identified, extrapolated forward, and checked against unassigned MTPC clusters to complete track reconstruction from both the main vertex and other sources. Finally, the local track fragments from different TPCs are merged to form *global* tracks, with the momentum determined from the measured track curvature in the magnetic field.

To obtain x and y components of the interaction vertex (also called *primary vertex*) position, the beam ion trajectory is extrapolated to the target plane. The global tracks are also extrapolated to the target plane to determine the z component of the interaction vertex position. Crucially, the fitting procedure provides a result flag, which indicates the fit quality.

Consequently, the *secondary* vertices are identified. The unstable neutral hadron can-

didates are usually recognized by their distinct V-shaped decay topology. It is characterised by two tracks emerging from a common decay point. Hence, further in the text, these candidates are referred to as V^0 *candidates*. First of all, a dedicated module of reconstruction iterates over all pairs of tracks with opposite charge signs not originating from the primary vertex. It calculates the Distance of Closest Approach (DCA) between the two tracks through a scan, and if the found DCA is small enough (< 1 cm), the pair of the tracks is saved as a V^0 candidate. The threshold is set based on the resolution of the fit of the secondary vertex to ensure reliable reconstruction. The z position of the DCA is weighted as shown in Fig 3.1: the algorithm finds the interval where the DCA was the smallest (d_i at interval z_i), gets DCA values for the next and previous interval (d_{i-1} at interval z_{i-1} and d_{i+1} at interval z_{i+1}, respectively), calculates the weights based on the differences between DCAs in the neighbouring intervals, and the V^0 candidate position is interpolated with usage of weights. The weighted position is then saved as the initial decay vertex position of the V^0 candidate. It is then forwarded as a starting parameter to the subsequent fitting procedure, where the decay vertex position is refitted together with the daughter tracks momenta.

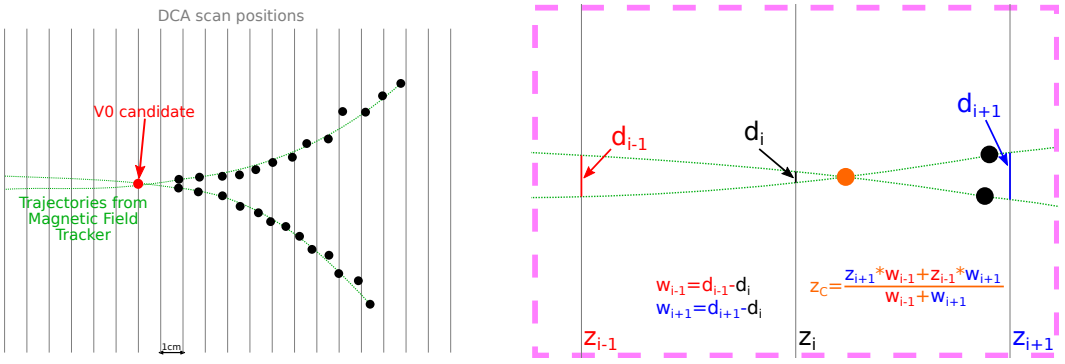

Figure 3.1: *Left*: DCA calculation procedure. The black dots represent TPC clusters, with green lines as reconstructed tracks. *Right*: Estimation of the z component of the decay vertex position of the V^0 candidate. The algorithm finds the interval, where the DCA was the smallest (d_i at interval z_i), gets DCA values for the next and previous interval (d_{i-1} at interval z_{i-1} and d_{i+1} at interval z_{i+1}, respectively), calculates the weights based on the differences between DCAs in the neighbouring intervals, and the V^0 candidate position is interpolated with the usage of weights.

In addition, the global tracks are extrapolated to the TOFs, and the tracks and hits registered by the TOFs are matched to each other. If the matching is successful, the TOF-related information (e.g. time-of-flight, squared mass, charge) is calculated and

added to the track.

Finally, the raw data from the PSD detector is converted into energy deposits using the calibration constants derived from the data on the cosmic rays and hadron beams. This process assigns the measured energy of projectile spectators (in GeV) to each event, which is then used for centrality determination during the analysis.

As a result, after completing the full reconstruction procedure, each event has details on the beam ion trajectory, trigger configuration, list of vertices and tracks and PSD energy deposit. Each track contains information on its momentum, charge sign, number of clusters and specific energy loss. Additionally, the information related to the time-of-flight is available for the tracks reaching the TOF detectors. An example of the reconstructed event from Ar+Sc collision is shown in Fig. 3.2.

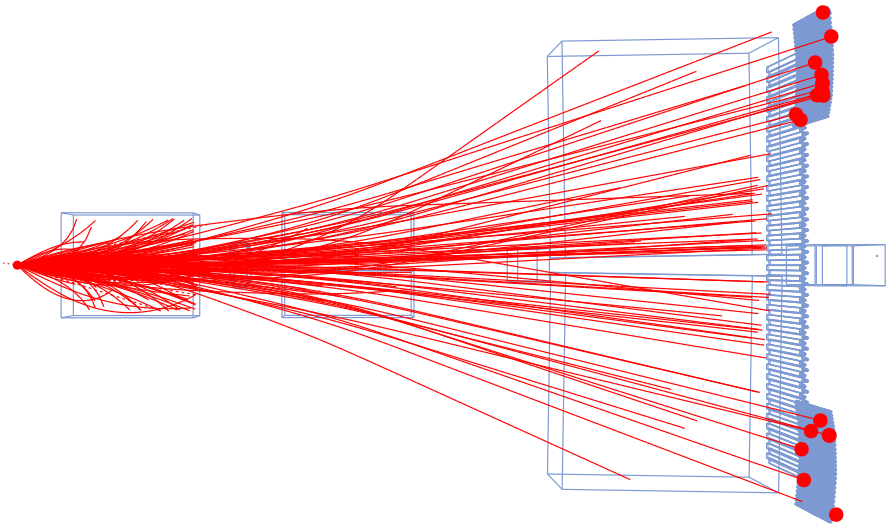

Figure 3.2: Visualization of reconstructed Ar+Sc collision at 75A GeV/c. The red lines depict reconstructed tracks along with red points as hits in TOF.

3.1.2 Monte Carlo simulations

Each of the reconstruction steps described above comes with a certain inefficiency, either due to the limited detection efficiency of each subdetector or limitations of the reconstruction algorithms themselves. A detailed simulation of the detector and its reconstruction is performed with the Monte Carlo method, in order to estimate the reconstruction efficiency for a given physics process and calculate the correction factors that need to be applied to the observables extracted from data. The

EPOS1.99 [65, 66] model is employed to generate the kinematic distributions of simulated events for hadron production in a collision. This choice is related to a good agreement of this model with experimental data, confirmed by a study of Monte Carlo generators for the data analysis in proton-proton collisions [67]. Additionally, the EPOS1.99 model accounts for the fragmentation of the colliding nuclei, which is advantageous for the analysis of the ion collisions.

Afterwards, the interactions of the generated particles with the detector material are simulated using the GEANT4 package [68] with FTFP_BERT physics list [69] and the NA61/SHINE geometry implemented. The simulation output undergoes digitalization dedicated to each subdetector, which is then processed by the same reconstruction chain as that used for the experimental data. It enables a direct comparison between reconstructed experimental and Monte Carlo data.

At the end, the described procedure produces two event types:

- generated MC events (MC_{gen}): a set of the events, which includes information about the simulated particles taken directly from the model (i.e. their true origin, species, momentum etc.),
- reconstructed MC events (MC_{rec}): a set of the events, which mirrors the format used for the reconstructed experimental data.

3.2 Event selection

The series of event selection criteria are employed to assure high data quality and appropriate centrality selection. The analysis is carried out on a subset of events collected using the T2 trigger configuration, i.e. *central interaction* events. The event selection criteria can be grouped into non-biasing and biasing criteria. Non-biasing event selection criteria do not operate on variables, whose values are dependent on the fact of interaction, while biasing criteria do. The first criteria group concern the beam properties, such as beam quality and beam time structure, while the second addresses off-target interactions, reconstruction capabilities, and centrality selection.

3.2.1 Non-biasing event selection criteria

Non-biasing event selection criteria include the following:

(i) beam off-time,

(ii) beam quality.

The criteria are applied consecutively in the listed order to select a single beam ion interaction with the target in the analyzed event and ensure a well-measured beam ion trajectory.

Beam off-time

This criterion eliminates events with an additional beam ion interaction, close in time to the triggering one, thus ensuring no pile-up in the analyzed events. The event is excluded from the analysis if there was an additional beam ion within a $\pm 4\mu$s time window (time required to distinguish between two events in the TPCs) or a minimum bias interaction within a $\pm 25\mu$s time window (maximum hardware time during which the second interaction in the target is eliminated) around the triggering beam ion. The possible contamination of the data sample by unregistered off-time interactions due to a dead time of electronics was estimated to be of the order of 0.01% [64]. Hence, it is omitted during the systematic uncertainty calculation because of its negligible impact compared to other contributions.

Beam quality

This criterion guarantees precise reconstruction of the beam ion trajectory. It requires the presence of a signal from at least two detectors: BPD3 – the closest to the target, and either BPD1 or BPD2. This allows to accurately fit the beam ion trajectory and extrapolate it to the target region. Moreover, it verifies that the beam ion did not undergo interaction upstream of BPD3.

3.2.2 Biasing event selection criteria

Biasing event selection comprises subsequent criteria:

(i) primary vertex properties,

(ii) centrality.

This group of criteria is applied to minimize background from off-target interactions and to select the centrality of analyzed collisions. However, those criteria can potentially introduce biases into the analysis results; therefore, their impact is estimated during the calculation of the systematic uncertainties as described in Sec. 3.7.

Primary vertex properties

The criteria related to the primary vertex properties select the events with a well-reconstructed interaction point in the experimental target. The first criterion is based on the status of the primary vertex reconstruction and requires fit convergence. The x and y components of the primary vertex position are derived from the BPD trajectory fit, while the z component is determined by fitting secondary particle tracks.

The second criterion eliminates most off-target interactions and is applied to the z component of the primary vertex position. Fig. 3.3 shows the distributions of the z component of the primary vertex position for data collected with the target inserted (target IN) and removed (target OUT) with the latter scaled to match the integral for the target IN data in the range of $z < -620$ cm. The observed maxima correspond to different detector elements, with the sharp peak from target interactions appearing only in the target IN data. The detector structures are present in both datasets – V1 and BPD-3 upstream of the target ($z \in [-685; -645]$), and the helium box and front

face of VTPC-1 downstream of the target ($z \in [-560; -505]$). Events with a primary vertex z position within ± 2 cm of the target position are retained for analysis, with the selection values marked by the dashed lines.

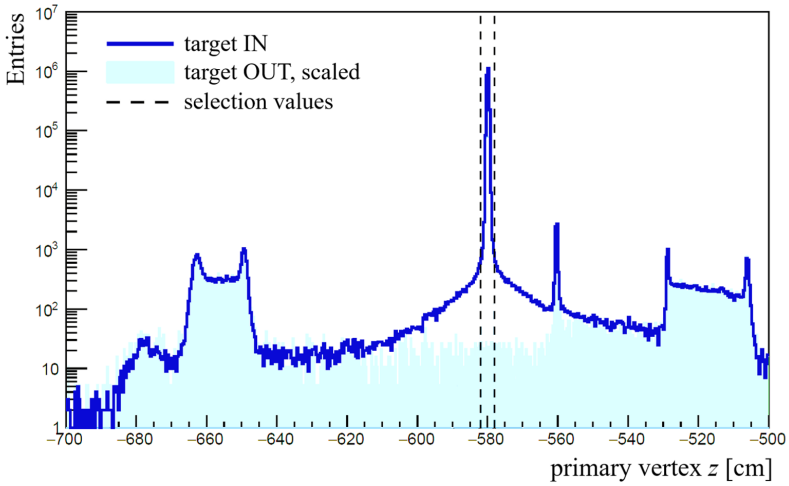

Figure 3.3: The distribution of the z component of the primary vertex position for Ar+Sc collisions at 75A GeV/c. The solid line represents the target IN data, while the cyan histogram indicates the scaled target OUT data. The observed maxima correspond to different detector elements, with the sharp peak from target interactions appearing only in the target IN data. The detector structures are present in both datasets – V1 and BPD-3 upstream of the target ($z \in [-685; -645]$), and the helium box and front face of VTPC-1 downstream of the target ($z \in [-560; -505]$). The dashed lines indicate the accepted range of values for analysis.

Centrality

The results presented in this thesis are obtained for the 10% most central Ar+Sc collisions. As was mentioned earlier, the centrality selection in the experimental data relies on the information from the PSD detector, which provides measurements of the energy of projectile spectators and produced particles inside its geometrical acceptance. This subsection briefly describes the centrality selection procedure, while a detailed description can be found in Refs. [70–72].

During the data taking, the integrated signal from 16 central PSD modules (as shown in the left panel of Fig. 3.4) was utilized in the T2 trigger for online centrality selection. The set threshold was selecting approximately the 30% most central events.

Additionally, an offline procedure was developed for more precise centrality selection using the PSD data.

Firstly, it is necessary to establish the PSD modules which will be used for the event centrality selection at a given beam momentum. Herein, one needs to study the correlation between the energy deposit and the total track multiplicity for each module independently. The positive correlation indicates that most of the deposited energy in the module originates from produced particles, thus, this module should be excluded from consideration. In contrast, the anticipated negative correlation implies that the module mostly measures the energy of spectators. The modules employed for event centrality selection in this analysis are depicted in the middle and right panels of Fig. 3.4.

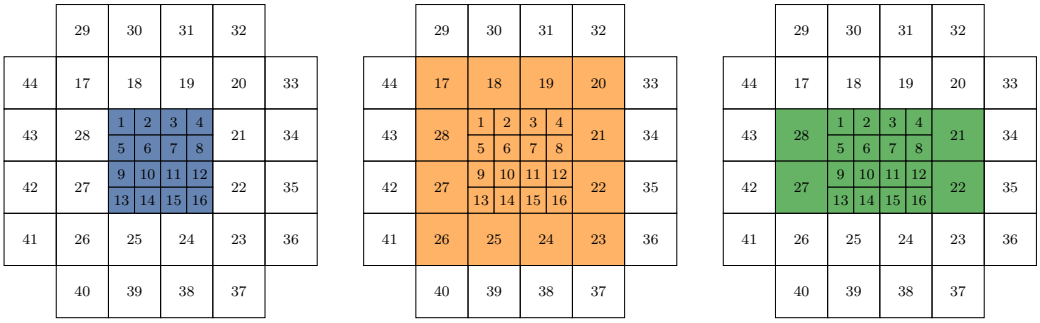

Figure 3.4: PSD modules used in online (*left*) and offline event centrality selection in Ar+Sc collisions at 40*A* and 75*A* GeV/*c* (*middle*), and 150*A* GeV/*c* (*right*).

The total energy E_{PSD} deposited in the selected modules is subsequently calculated. The threshold values, which determine specific centrality classes, are derived from the analysis of the minimum bias data. Fig. 3.5 displays the measured distributions of E_{PSD} for minimum-bias and central trigger-selected events, calculated during the offline analysis, at 150*A* GeV/*c* beam momentum. The shaded region indicates the area corresponding to 10% of the most central collisions. The selection values for 10% most central events for all beam momenta are summarized in Tab. 3.1. To be accepted for the analysis, the event should have the E_{PSD} value lower than the respective threshold for a given beam momentum.

The potential impact of the centrality selection procedure on the results was examined using Monte Carlo data, with a detailed description available at Ref. [64]. Essentially, the maximum bias due to the centrality selection was found to be below 0.5%, which is significantly smaller than other estimated sources of systematic un-

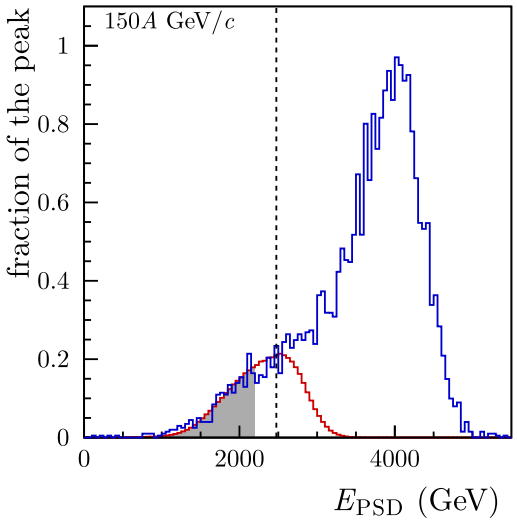

Figure 3.5: Energy E_{PSD} distribution as measured by the PSD calorimeter for 150A GeV/c beam momentum. The blue histogram represents minimum-bias selected events, while the red histogram corresponds to central trigger selected events, with histograms being normalized to align in the overlap region (left of the dotted line). The shaded area indicates the 10% of collisions with the lowest E_{PSD} values [73], which are accepted for the analysis.

Table 3.1: Summary of the centrality selection based on E_{PSD} threshold values used for the analysis of Ar+Sc collisions at different beam momenta.

p_{beam} [GeV/c]	E_{PSD} threshold [GeV]
40A	665.6
75A	1290.6
150A	2276.0

certainty and is thus disregarded in the total systematic uncertainty calculation.

The outlined procedure is utilized for the experimental data, while for the generated and reconstructed Monte Carlo simulated data the centrality selection is based on the number of participants, i.e. interacting nucleons, given by the EPOS1.99 model output. To be consistent with the data, the threshold for the number of participants is set to select the 10% most central Ar+Sc collisions for a given beam momentum.

3.2.3 Event statistics

The event selection criteria outlined in this section are used for experimental data. Besides, the biasing criteria are applied to reconstructed Monte Carlo simulated data, and an appropriate centrality class is chosen for generated Monte Carlo simulated data. Fig. 3.6 illustrates the reduction in the number of events with selection criteria consecutively applied for experimental data and reconstructed Monte Carlo simulated data for all beam momenta. The labels on the x-axes correspond to respective event selection criteria applied in sequence: nEvents is the total number of recorded events, nT2 is the number of events collected with the T2 trigger configuration, nWFA is the number of events after the beam off-time selection, nGoodBPD is the number of events after the beam quality selection, nHasFittedVertex and nZVertex are the number of events after further selections on fit convergence of the primary vertex and its position, respectively, and finally, nCentrality is the number of events available for analysis after the centrality selection.

Table 3.2 summarizes the statistical power of data before and after event selection. Additionally, it was checked that the event selection criteria remove nearly all events in the target OUT dataset [64]. Therefore, any potential contribution from off-target interactions is disregarded in the analysis.

Table 3.2: Summary of the number of events before and after selection in experimental data, generated and reconstructed Monte Carlo data.

p_{beam}	data		generated MC		reconstructed MC	
[GeV/c]	before selection	after selection	before selection	after selection	before selection	after selection
40A	$8.9 \cdot 10^6$	$1.3 \cdot 10^6$	$1.8 \cdot 10^7$	$1.8 \cdot 10^6$	$1.8 \cdot 10^7$	$1.8 \cdot 10^6$
75A	$4.1 \cdot 10^6$	$1.1 \cdot 10^6$	$1.9 \cdot 10^7$	$1.9 \cdot 10^6$	$1.9 \cdot 10^7$	$1.9 \cdot 10^6$
150A	$2.5 \cdot 10^6$	$0.8 \cdot 10^6$	$1.8 \cdot 10^7$	$1.8 \cdot 10^6$	$1.8 \cdot 10^7$	$1.8 \cdot 10^6$

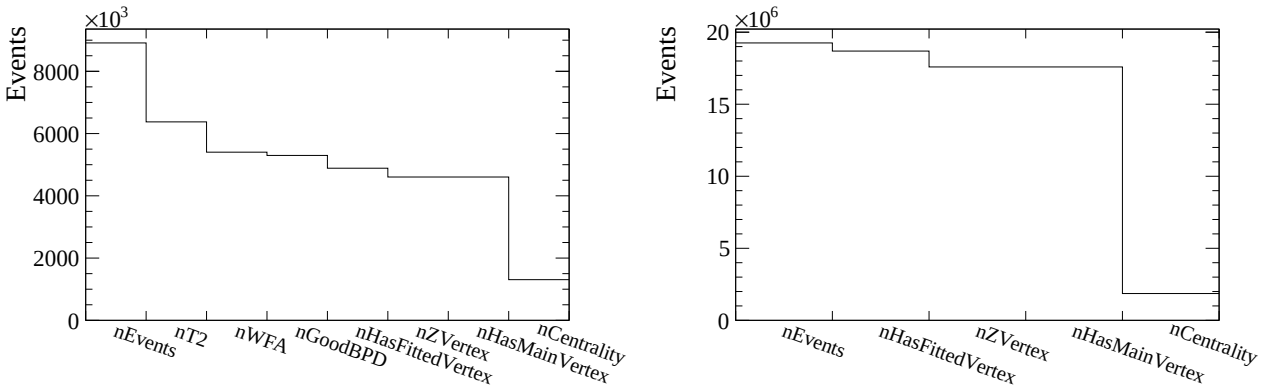

(a) 40A GeV/c

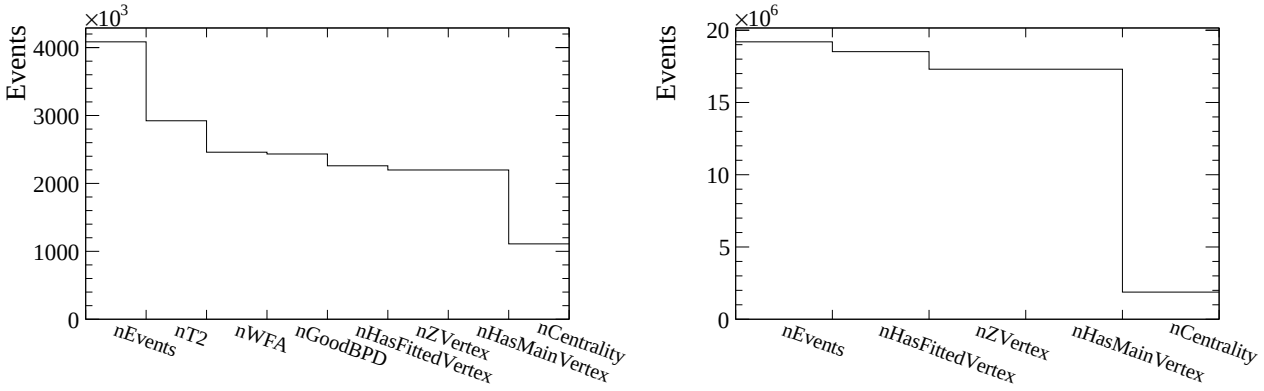

(b) 75A GeV/c

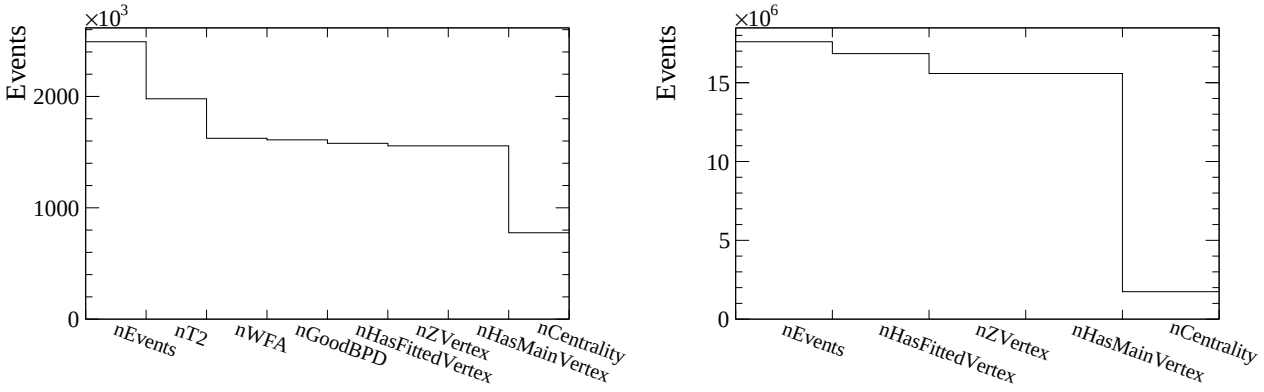

(c) 150A GeV/c

Figure 3.6: Reduction in the number of events with selection criteria consecutively applied (see text for more details) for experimental data (*left*) and reconstructed Monte Carlo simulated data (*right*) in Ar+Sc collisions at (a) 40A, (b) 75A, and (c) 150A GeV/c.

3.3 Track and candidate selection

The V^0 candidates are searched for in all events that pass the event selection criteria. As explained earlier, they are obtained by pairing all positively and negatively charged tracks during the reconstruction. These candidates must meet further track and candidate selection criteria. The track selection criteria relate to the properties of the daughter particles, while the candidate selection criteria concern the properties of the V^0 candidate itself.

In this analysis, Λ baryons are identified by their weak decay channel $\Lambda \longrightarrow p + \pi^-$ with a branching ratio of 63.9%, which is shown in Fig. 3.7.

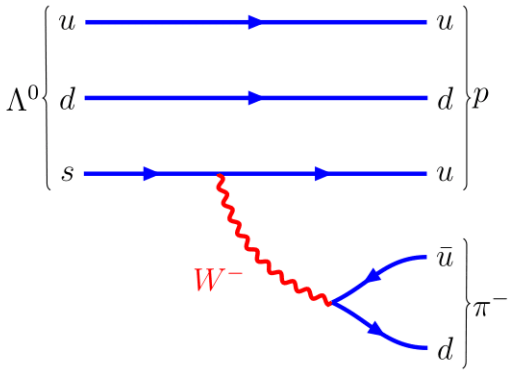

Figure 3.7: A Feynman diagram of the Λ baryon (uds) weak decay to a proton (uud) and negatively charged pion $(\bar{u}d)$.

Charged daughter track selection constitutes the criteria below:

(i) number of reconstructed VTPC clusters,

(ii) minimal momentum,

(iii) specific energy loss (p and π^- pair).

This group of criteria ensures the quality of momentum determination of the daughter tracks and reduces background from low-momentum electrons and V^0 candidates other than Λ baryons.

Number of reconstructed VTPC clusters

This criterion establishes the high-quality reconstruction of particle momenta by requiring an adequate number of clusters reconstructed in both VTPCs. For each track,

the minimal number of clusters is required to be 10.

Minimal momentum

This criterion is implemented to suppress background primarily originating from low-momentum electrons. For each track, the minimal reconstructed momentum is required to be 0.5 GeV/c. The effect can be seen on the Armenteros-Podolanski plots in Fig. 3.23, detailed in Sec. 3.8.

Specific energy loss

The measurements of momentum and energy loss of the particle in active TPC volume allow for its identification using the Bethe-Bloch parametrization. The identification, however, can be obstructed in the low-momentum region due to the overlapping parameterization curves, which correspond to different particle species. In order to suppress background in the Λ mass region, proton and pion candidates are selected by requiring their respective measured energy losses in the TPC volumes to be within $\pm 3\sigma$ around the nominal value around the relevant Bethe-Bloch parameterization curve, as illustrated in Fig. 3.8. This selection is applied only to the experimental data, as there is no simulation of $\mathrm{d}E/\mathrm{d}x$ for the NA61/SHINE setup due to the necessary computing time to obtain full energy loss of the particle in active TPC volume. Instead, an experimentally driven digitizer is used to generate clusters from the simulated points as mentioned in Sec. 3.1. The corresponding correction is discussed further in Sec. 3.6.

The candidate selection criteria contain the following:

(i) directional angle,

(ii) decay length.

These criteria are used to suppress the combinatorial background further. The values for the last two criteria are optimized separately for each rapidity bin using Monte-Carlo simulation according to the procedure explained in Sec.3.5.

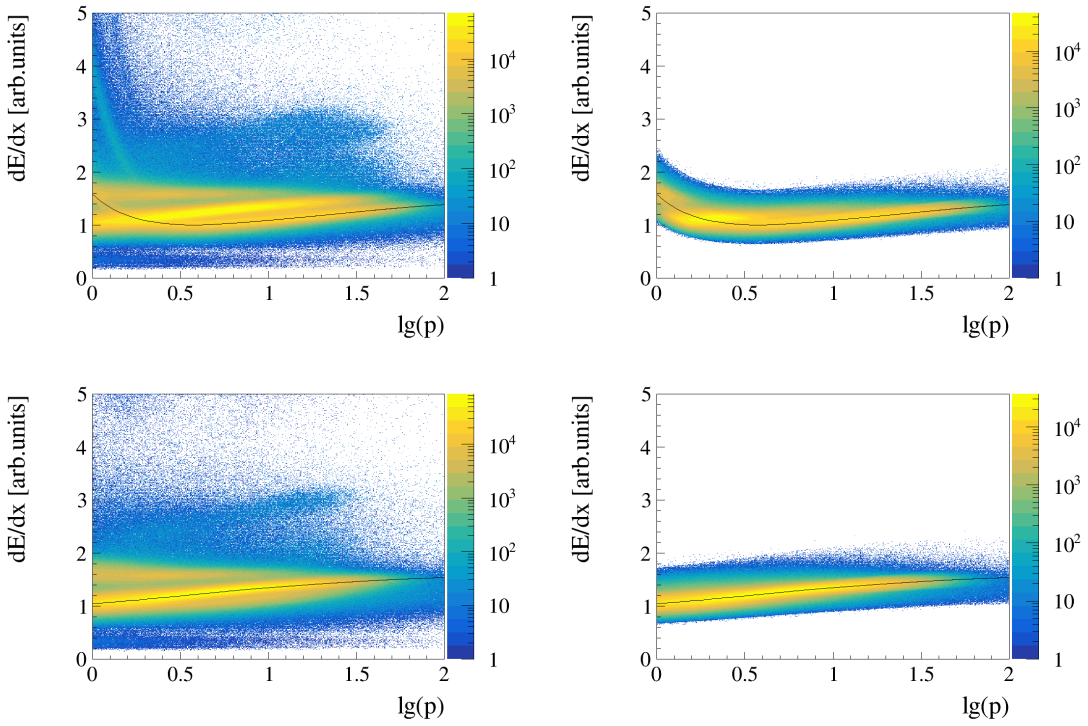

Figure 3.8: Example distributions of $lg(p)$ versus $\mathrm{d}E/\mathrm{d}x$ for positively (*top*) and negatively (*bottom*) charged daughter particles of V^0 candidates reconstructed in Ar+Sc collisions at 75A GeV/c before (*left*) and after (*right*) specific energy loss selection. The black lines show the Bethe-Bloch parametrization of the energy loss for protons (*top*) and pions (*bottom*), respectively.

Directional angle

The directional angle is defined as the angle between the vector sum of the momenta of V^0 candidate decay products, $\overrightarrow{p_\Lambda}$, and a vector connecting the primary production vertex and the V^0 candidate decay vertex, $\overrightarrow{vtx_\Lambda}$, as shown in the left panel of Fig. 3.9.

The selection is imposed on the cosine of the directional angle, which is calculated as

$$\cos\alpha = \frac{\overrightarrow{vtx_\Lambda} \cdot \overrightarrow{p_\Lambda}}{|\overrightarrow{vtx_\Lambda}| \cdot |\overrightarrow{p_\Lambda}|} \,. \tag{3.1}$$

For a two-body decay, it is expected to be equal to 1, however, the detector resolution introduces small deviations from unity. The example distribution of the cosine of the directional angle for V^0 candidates in data is illustrated in the right panel of

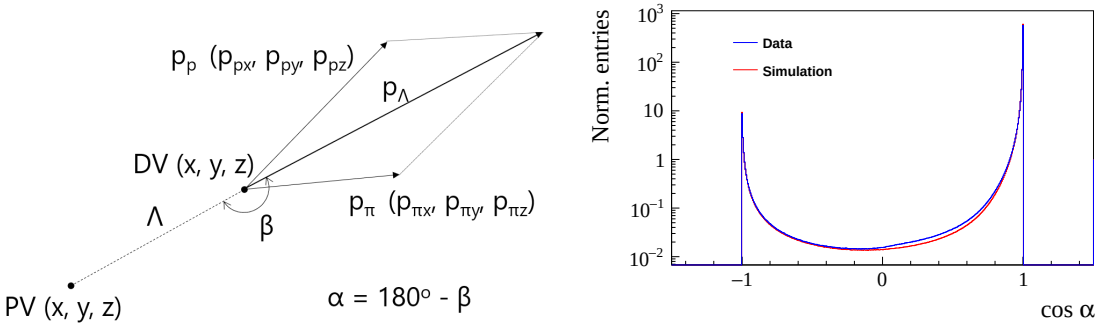

Figure 3.9: *Left*: Example V^0 candidate decay construing the directional angle definition. *Right*: Example distribution of the cosine of the directional angle for V^0 candidates reconstructed in experimental data (*blue*) and Monte-Carlo simulation (*red*) in Ar+Sc collisions at 75*A* GeV/*c* beam momentum.

Fig. 3.9: the presence of background not peaking at unity is evident. To reduce this background, a selection requirement is applied to this variable. As was mentioned before, the values of this selection criterion are optimized as explained in Sec. 3.5. Table 3.3 summarizes the values of selection criterion used in the analysis.

Table 3.3: Summary of the selection requirements on the cosine of the directional angle used for the analysis of Ar+Sc collisions at different beam momenta.

p_{beam} [GeV/c]	rapidity range	value
40*A*	$y \in (-1.5; 0.0]$	> 0.9995
	$y \in (0.0; 2.0]$	> 0.9999
75*A*	$y \in (-1.5; 0.0]$	> 0.9995
	$y \in (0.0; 1.5]$	> 0.9999
150*A*	$y \in (-2.0; -0.5]$	> 0.9995
	$y \in (-0.5; 1.5]$	> 0.9999

Decay length

The V^0 candidate decay length is defined as the distance between the primary vertex (PV) and V^0 candidate decay vertex (DV) as shown in the left panel of Fig. 3.10.

It is calculated as

$$\Delta L = \sqrt{\sum_{i=x,y,z} (DV_i - PV_i)^2} \tag{3.2}$$

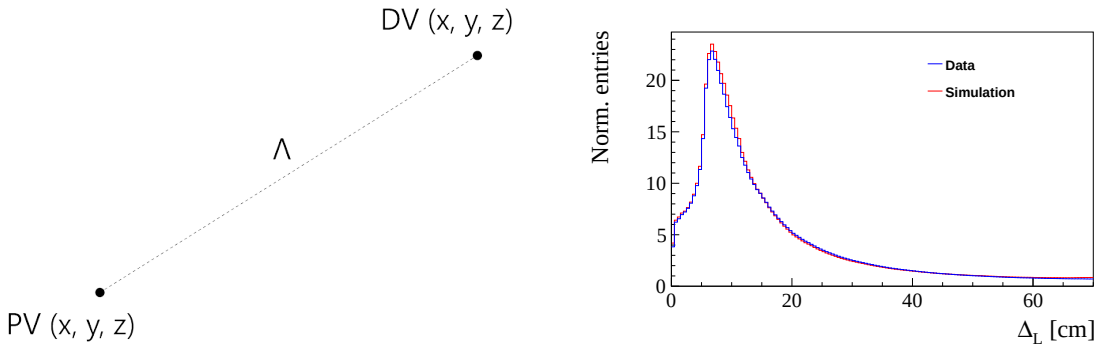

Figure 3.10: *Left*: Example V^0 candidate decay construing the decay length definition. *Right*: Example distribution of the decay length for V^0 candidates reconstructed in experimental data (*blue*) and Monte-Carlo simulation (*red*) in Ar+Sc collisions at 75A GeV/c beam momentum.

This selection sets a threshold on the minimum V^0 candidate decay length; thus, the contribution of primary tracks mistakenly identified as V^0 candidates is minimized. The example distribution of the decay length for V^0 candidates is illustrated in the right panel of Fig 3.10. As previously noted, the selection values are optimized, and it was found that the decay length should be greater than 10 cm for all analysed beam momenta. Additionally, a z component of V^0 candidate decay vertex position is required to be greater than a z component of the primary vertex position.

3.4 Signal extraction

3.4.1 Binning

The analysis focuses on extracting the uncorrected (raw) signal yields of Λ baryons from the invariant mass distribution. At this point, the dataset comprises all V^0 candidates that meet all selection criteria. The invariant mass of each V^0 candidate is computed using the formula:

$$m(p\pi^-) = \sqrt{(E_p + E_{\pi^-})^2 - (\vec{p}_p + \vec{p}_{\pi^-})^2}\,, \tag{3.3}$$

where E_p and E_{π^-} represent the energies of V^0 candidate decay products under the assumption of proton and pion masses, respectively, and $\vec{p}_p$ and $\vec{p}_{\pi^-}$ denote their three-momenta. V^0 candidates associated with true Λ decays contribute to the peak

near the Λ baryon mass, while V^0 candidates built of two unrelated tracks contribute to the *combinatorial* background that has a smooth distribution across the considered invariant-mass range.

The data is binned based on rapidity (y) and transverse momentum (p_T) phase space. Rapidity is calculated as follows:

$$y = \frac{1}{2} \ln \frac{E + p_z}{E - p_z} , \tag{3.4}$$

where E and p_z represent the total energy and longitudinal momentum (momentum along the beam axis) of the V^0 candidate, assuming $c \equiv 1$. In the context of the collision centre-of-mass frame (CMS), the phase space near $y = 0$ is called *mid-rapidity*. Regions with positive $(y > 0)$ and negative $(y < 0)$ rapidity are referred to as *forward* and *backward* rapidity regions, respectively. Rapidity values utilized in this analysis are computed within the collision CMS.

Table 3.4 summarizes the ranges and number of bins of equal width ($\Delta y = 0.5$ and $\Delta p_T = 0.3$) in which analysis is performed for each beam momentum. The accepted bins for the analyses are depicted in Figs. 4.1, 4.2, and 4.3 in Chapter 4, which show the corrected $d^2n/dydp_T$ spectra for different beam momenta values.

Table 3.4: Summary of binning used for the analysis of Ar+Sc collisions at different beam momenta.

p_{beam}	rapidity		transverse momentum	
[GeV/c]	range	number of bins	range	number of bins
40A	$y \in (-1.5; 2.0)$	7	$p_T \in (0.0; 3.0)$	10
75A	$y \in (-1.5; 1.5]$	6	$p_T \in (0.0; 3.0)$	10
150A	$y \in (-2.0; 1.5]$	7	$p_T \in (0.0; 3.0)$	10

3.4.2 Fit procedure

The number of selected signal V^0 candidates is estimated by fitting to the invariant mass distribution in each (y, p_T) bin separately. The fitting is conducted using the unbinned extended maximum likelihood method within the RooFit framework [74]. In an extended fit, the likelihood includes terms proportional to the observed signal and background yields, along with their uncertainties.

The fit distribution is parametrized with a Breit-Wigner signal peak over a Chebychev

polynomial background. The Breit-Wigner distribution is described as:

$$B(x; m, \sigma) = A_B \cdot \frac{1}{(x-m)^2 + \left(\frac{\sigma}{2}\right)^2} \,, \tag{3.5}$$

where A_B serves as a normalization factor, and m and σ denote the mean and half-width at half-maximum, respectively. In turn, the Chebyshev polynomial distribution $T(x; c_0, ..., c_n)$ is expressed as:

$$T(x; c_0, ..., c_n) = A_T \cdot \left(T_0(x) + \sum_{k=1}^{n} p_k T_k(x) \right) \,, \tag{3.6}$$

where A_T is a normalization factor, p_k are the polynomial coefficients, and $T_k(x)$ represent a k^{th} order Chebyshev polynomials of the first kind.

For analysis of Ar+Sc collisions at 40*A* and 75*A* GeV/*c*, the fitting range is constrained as $1.095 < m(p\pi^-) < 1.17$ GeV/c^2 to improve the description of the background. Typically, the 4^{th} order Chebyshev polynomial is used to describe the background. If the number of candidates in a given bin is lower than 10^4, then the 3^{rd} order polynomial is utilized in order to enhance the fit stability. Yet, at 150*A* GeV/*c*, the fitting range is narrower: $1.095 < m(p\pi^-) < 1.14$ GeV/c^2 to increase signal-to-background ratio, and, consequently, the background is represented by the 2^{nd} order polynomial. Example fitted invariant mass distributions of V^0 candidates are depicted in Fig. 3.11. Further, the uncorrected (raw) signal yields of Λ baryons in Ar+Sc collisions at 40*A*, 75*A*, and 150*A* GeV/*c* together with their uncertainties, as returned by the fit, are illustrated in Fig. 3.12.

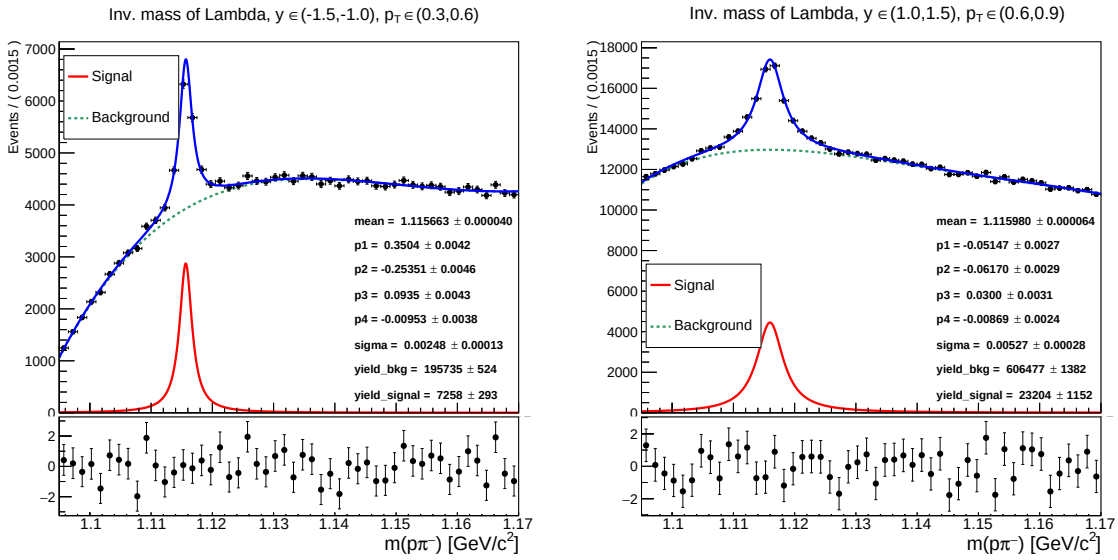

Figure 3.11: Example $p\pi^-$ invariant mass distributions in Ar+Sc collisions at 75A GeV/c for $y \in (-1.5; -1.0], p_T \in (0.3; 0.6]$ (*left*) and $y \in (1.0; 1.5], p_T \in (0.6; 0.9]$ (*right*). The data points are shown in black. The total fit result is shown in blue with the Λ signal component represented in red. The fit parameters displayed on the right include the mean and width (sigma) of the Breit-Wigner signal peak, Chebyshev polynomial coefficients (p_1 to p_4), and signal and background yields. The pull plot at the bottom shows the normalized residuals and indicates a good agreement between the fit model and the data.

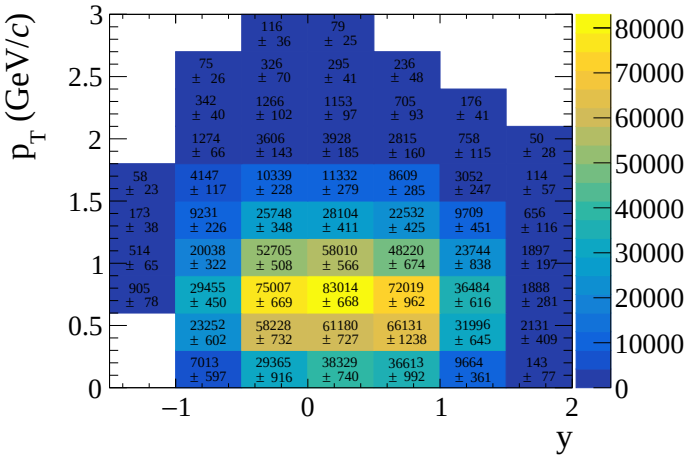

(a) 40*A* GeV/*c*

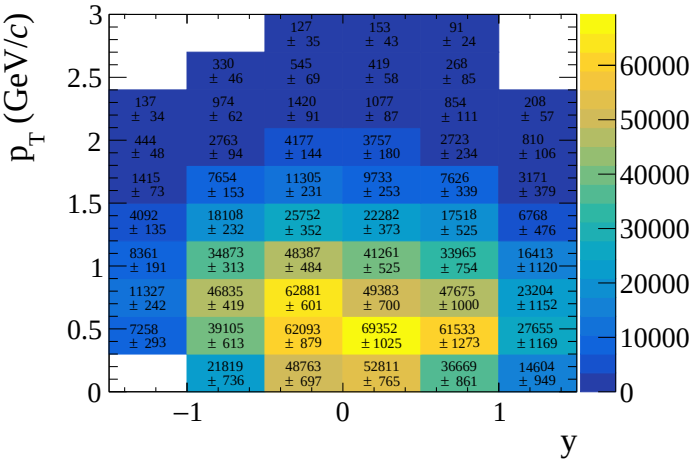

(b) 75*A* GeV/*c*

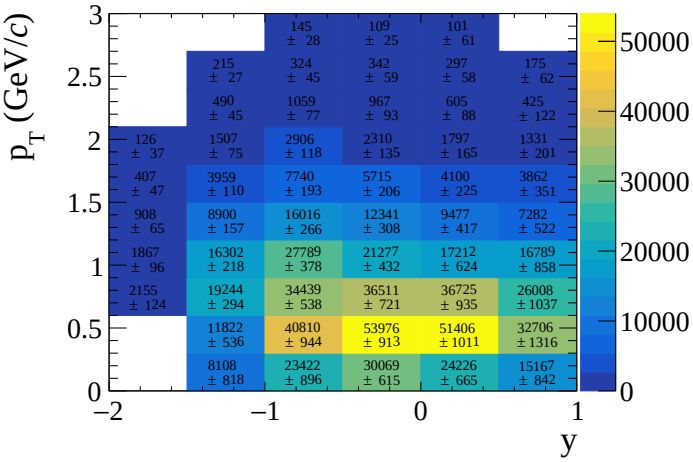

(c) 150*A* GeV/*c*

Figure 3.12: Distributions of uncorrected (raw) signal yields of Λ baryons in $y - p_T$ phase space produced in central Ar+Sc collisions at (a) 40*A*, (b) 75*A*, and (c) 150*A* GeV/*c* with statistical uncertainties.

3.5 Selection optimisation

The optimization of the candidate selection is performed using reconstructed Monte Carlo simulated data, with each rapidity bin treated independently. Different selection requirements are assessed within each bin to determine the optimal value. The invariant mass spectra are obtained for the V^0 candidates, which passed event and track selection, in addition to a given selection value being tested. The spectra are then fitted with the previously described procedure, and the signal significance is computed as $\frac{S}{\sqrt{S+B}}$, where S and B represent the signal and background yields, respectively. The signal significance and yield distributions are plotted as a function of the selection values, and the signal yield distribution is scaled to match the integral of the signal significance distribution. The value lying in the intersection of two distributions is selected for further analysis.

As mentioned earlier, two candidate selection criteria are optimized: the cosine of the directional angle and the decay length. The tested values for each criterion during the selection optimization are provided in Table 3.5 with the example distributions for the directional angle selection shown in Fig. 3.13. The selection values used in the analysis are summarized in Sec. 3.3.

Table 3.5: Summary of the selection values on the cosine of the directional angle and decay length tested during the selection optimization.

Cut number	$\cos\alpha$ value	Δ_L value
1	0.99	2.5
2	0.995	5.0
3	0.999	7.5
4	0.9995	10.0
5	0.9999	12.5
6	0.99995	15.0
7	0.99999	17.5
8	0.999995	20.0

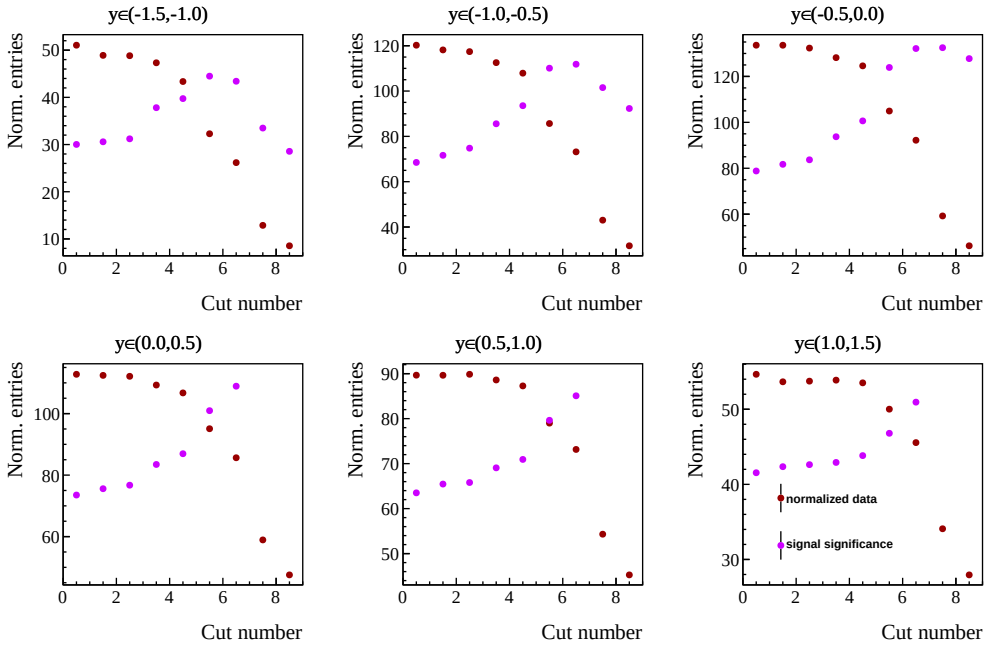

Figure 3.13: Example distributions of signal significance (magenta points) and signal yield (brown points) as a function of directional angle selection values in Ar+Sc collisions at 75A GeV/c after event and track selection. The signal yield distribution is scaled to match the integral of the signal significance distribution. The tested values for the criterion during the selection optimization are provided in Table 3.5.

3.6 Corrected yields and statistical uncertainties

A detailed Monte Carlo simulation was performed to compute the correction for losses due to the geometrical acceptance and reconstruction inefficiency, selections applied in the analysis, branching ratio and feed-down from the decays of heavier hyperons. The simulation procedure was already described in Sec. 3.1. The simulated events were reconstructed with the same software used for real collision events, and the same selections were applied (with the exception of specific energy loss). The branching ratio of Λ baryon decays to $p\pi^-$ is taken into account in the GEANT4 software package. For each y and p_T bin, the correction factor $c_{MC}(y, p_T)$ is calculated as:

$$c_{MC}(y, p_T) = \frac{n^{gen}_{MC}(y, p_T)}{N^{gen}_{MC}} \Big/ \frac{n^{acc}_{MC}(y, p_T)}{N^{acc}_{MC}} , \tag{3.7}$$

where:

- $n_{MC}^{gen}(y, p_T)$ is the number of Λ generated in a given (y, p_T) bin,

- $n_{MC}^{acc}(y, p_T)$ is the number of reconstructed Λ in a given (y, p_T) bin, which is obtained by following the same extraction procedure as for experimental data,

- N_{MC}^{gen} is the number of 10% most central generated events,

- N_{MC}^{acc} is the number of accepted events (after event selection).

The statistical uncertainty of the correction factor $c_{MC}(y, p_T)$ has two contributions, the first, α, related to the event selection and the second, β, connected with the track and candidate selection:

$$c_{MC}(y, p_T) = \frac{n_{MC}^{gen}(y, p_T)}{N_{MC}^{gen}} \Big/ \frac{n_{MC}^{acc}(y, p_T)}{N_{MC}^{acc}} = \frac{N_{MC}^{acc}}{N_{MC}^{gen}} \Big/ \frac{n_{MC}^{acc}(y, p_T)}{n_{MC}^{gen}(y, p_T)} = \frac{\alpha}{\beta(y, p_T)} \,. \quad (3.8)$$

The error of α is calculated assuming a binomial distribution:

$$\Delta\alpha = \sqrt{\frac{\alpha(1-\alpha)}{N_{MC}^{gen}}} \,. \quad (3.9)$$

The error of β is calculated according to the formula:

$$\Delta\beta(y, p_T) = \sqrt{\left(\frac{\Delta n_{MC}^{acc}(y, p_T)}{n_{MC}^{gen}(y, p_T)}\right)^2 + \left(\frac{n_{MC}^{acc}(y, p_T) \cdot \Delta n_{MC}^{gen}(y, p_T)}{(n_{MC}^{gen}(y, p_T))^2}\right)^2} \,, \quad (3.10)$$

where $\Delta n_{MC}^{acc}(y, p_T)$ is the uncertainty from the fit, and $\Delta n_{MC}^{gen}(y, p_T) = \sqrt{n_{MC}^{gen}(y, p_T)}$. The equation for $\Delta c_{MC}(y, p_T)$ can then be written as:

$$\Delta c_{MC}(y, p_T) = \sqrt{\left(\frac{\Delta\alpha}{\beta}\right)^2 + \left(-\frac{\alpha \cdot \Delta\beta}{\beta^2}\right)^2} \,. \quad (3.11)$$

The distributions of correction factors $c_{MC}(y, p_T)$ with statistical uncertainties for Ar+Sc collisions at 40A, 75A, and 150A GeV/c are shown in Fig. 3.14.

The loss of the Λ baryons due to the specific energy loss selection is corrected with an additional factor:

$$c_{dE/dx} = \frac{1}{\epsilon^2} = 1.005 \,, \quad (3.12)$$

where $\epsilon = 0.9973$ is the probability for protons or pions to be detected within $\pm 3\sigma$ around the nominal Bethe-Bloch value.

Finally, the double-differential yield of Λ baryons per inelastic event in bins of (y, p_T) is calculated as follows:

$$\frac{d^2n}{dy\,dp_T}(y, p_T) = \frac{c_{dE/dx} \cdot c_{MC}(y, p_T)}{\Delta y\,\Delta p_T} \cdot \frac{n_\Lambda(y, p_T)}{N_{events}}\,, \tag{3.13}$$

where:

- $c_{dE/dx}$, $c_{MC}(y, p_T)$ are the correction factors described above,
- Δy and Δp_T are the bin widths,
- $n_\Lambda(y, p_T)$ is the uncorrected number of Λ baryons, obtained by the signal extraction procedure,
- N_{events} is the number of events after event selection.

The statistical uncertainties $\Delta n_\Lambda(y, p_T)$ of the corrected double-differential yields receive contributions from the statistical uncertainty of the correction factor $c_{MC}(y, p_T)$ and the statistical uncertainty of the uncorrected number of Λ baryons taken from the fit, and are obtained as:

$$\Delta\frac{d^2n}{dydp_T}(y, p_T) = \sqrt{\left(\frac{c_{dE/dx} \cdot c_{MC}(y, p_T)}{N_{events}\,\Delta y\,\Delta p_T}\right)^2 \Delta n_\Lambda^2(y, p_T) + \left(\frac{c_{dE/dx} \cdot n_\Lambda(y, p_T)}{N_{events}\,\Delta y\,\Delta p_T}\right)^2 \Delta c_{MC}^2(y, p_T)}\,. \tag{3.14}$$

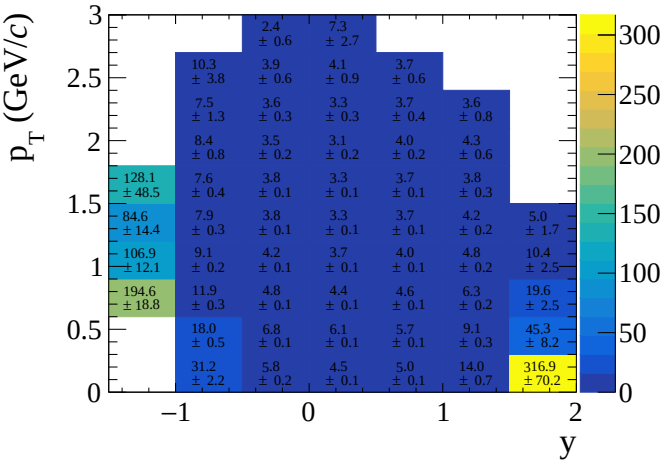

(a) 40A GeV/c

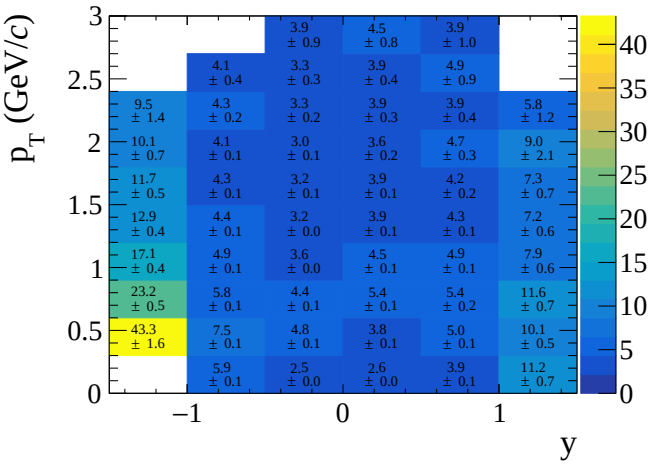

(b) 75A GeV/c

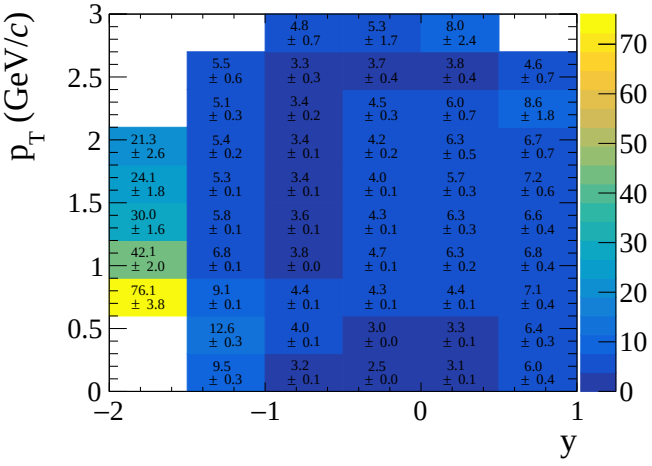

(c) 150A GeV/c

Figure 3.14: Distributions of correction factors for Ar+Sc collisions at (a) 40A, (b) 75A, and (c) 150A GeV/c with statistical uncertainties.

3.7 Systematic uncertainties

The systematic uncertainties of the results are assessed by independently altering each biasing selection criterion. The entire analysis is performed with the given alteration, and then the results are compared to those obtained with nominal selection values. Typically, two modifications for each selection criterion are defined: *tight* (more constraining than nominal) and *loose* (less constraining than nominal). The maximum deviations are determined for every criterion contributing to total systematic uncertainty. The total systematic uncertainty is calculated as the sum in quadrature of the contributions of possible biases, assuming they are uncorrelated. This procedure is used to estimate systematic uncertainties of all final quantities presented in this thesis.

The following selection criteria are considered as biasing for the calculation of the systematic uncertainties:

(i) event selection:

- primary vertex z position,

(ii) charged daughter track selection:

- number of reconstructed VTPC clusters,
- minimal momentum,
- specific energy loss,

(iii) candidate selection:

- directional angle,
- decay length,

(iv) signal extraction:

- fit range.

The tight and loose values along the nominal values for each selection criterion are summarized in Table 3.6. The first part of the table indicates the values of selection criteria which are common for all analyzed beam momenta. The subsequent parts

of the table focus each on a given beam momentum value. Moreover, the directional angle selection values are shown for separate rapidity ranges.

As noted before, the fit range is assumed to be biasing in the signal extraction procedure. The fitting range options are outlined in Table 3.6 for each beam momentum value individually. Additionally, all starting fit parameters are modified to test the stability of the fitting model, and the contribution to the systematic uncertainty is found to be negligent.

The contributions of the different biases to the total systematic uncertainty, expressed as the percentages of the nominal yield, are shown in Figs. 3.15, 3.16, and 3.18 for double-differential $y - p_T$ spectra of Λ baryons for Ar+Sc collisions at 40A, 75A, and 150A GeV/c, respectively. Additionally, Figs. 3.19, 3.20, and 3.21 illustrate the contributions for one-dimensional transverse momentum spectra of Λ in rapidity slices for each beam momentum value. To enhance readability in this case, the contributions are grouped by the source of bias, as described before (event selection, track selection, candidate selection, and signal extraction). In most bins, the partial contributions are below 10%, with increases at the edges of the acceptance.

Table 3.6: Summary of the values of selection criteria used for systematic uncertainty calculation in the analysis of Ar+Sc collisions at different beam momenta.

p_{beam} [GeV/c]	selection criterion	value		
		nominal	tight	loose
40A, 75A, 150A	primary vertex z [cm]	(-580 ± 2)	(-580 ± 1.5)	(-580 ± 5)
	num. of VTPC clusters	> 10	> 5	> 15
	minimal momentum [GeV/c]	> 0.5	> 0.6	> 0.4
	specific energy loss	$\pm 3\sigma$	$\pm 2.5\sigma$	$\pm 3.5\sigma$
	decay length [cm]	> 10	> 12.5	7.5
40A	cosine of the directional angle	$y \in (-1.5; 0.0]$		
		> 0.9995	> 0.9999	> 0.999
		$y \in (0.0; 2.0]$		
		> 0.9999	0.99995	0.9995
	fitting range [GeV/c^2]	$1.095 - 1.17$	$1.105 - 1.16$	$1.09 - 1.175$
75A	cosine of the directional angle	$y \in (-1.5; 0.0]$		
		> 0.9995	> 0.9999	> 0.999
		$y \in (0.0; 1.5]$		
		> 0.9999	0.99995	0.9995
	fitting range [GeV/c^2]	$1.095 - 1.17$	$1.105 - 1.16$	$1.09 - 1.175$
150A	cosine of the directional angle	$y \in (-2.0; -0.5]$		
		> 0.9995	> 0.9999	> 0.999
		$y \in (-0.5; 1.5]$		
		> 0.9999	0.99995	0.9995
	fitting range [GeV/c^2]	$1.095 - 1.14$	$1.105 - 1.135$	$1.09 - 1.145$

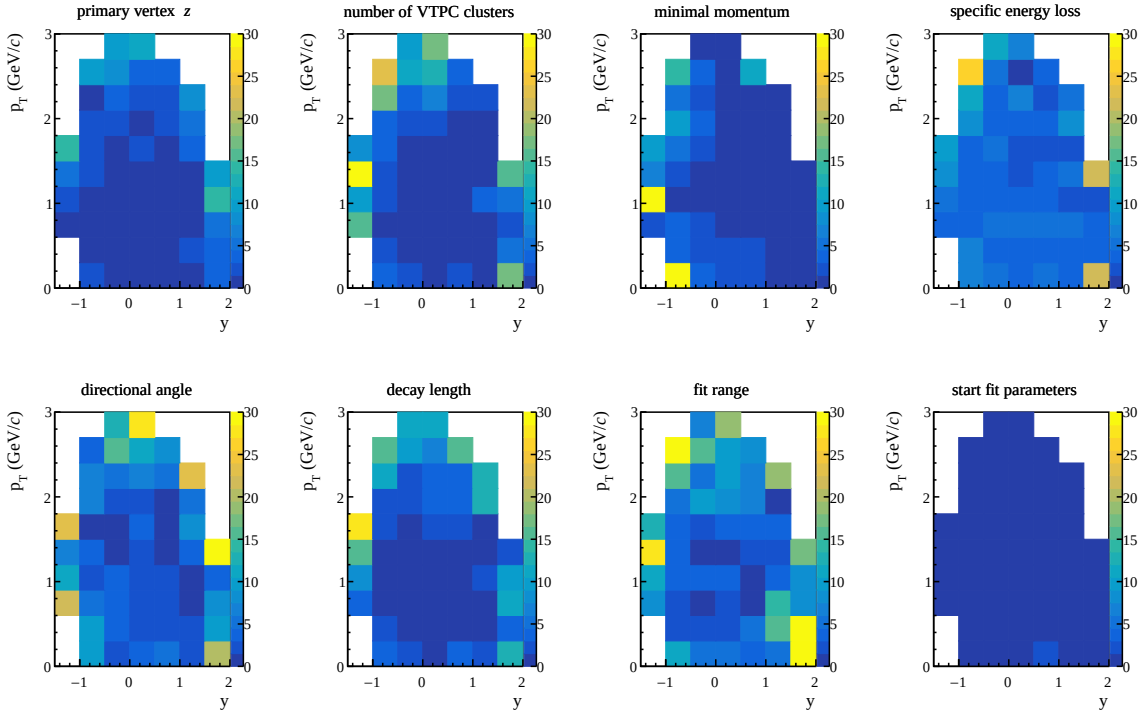

Figure 3.15: Contributions of selection criteria to the final systematic uncertainty of double-differential $y - p_T$ spectra of Λ baryons produced in central Ar+Sc collisions at 40A GeV/c beam momentum.

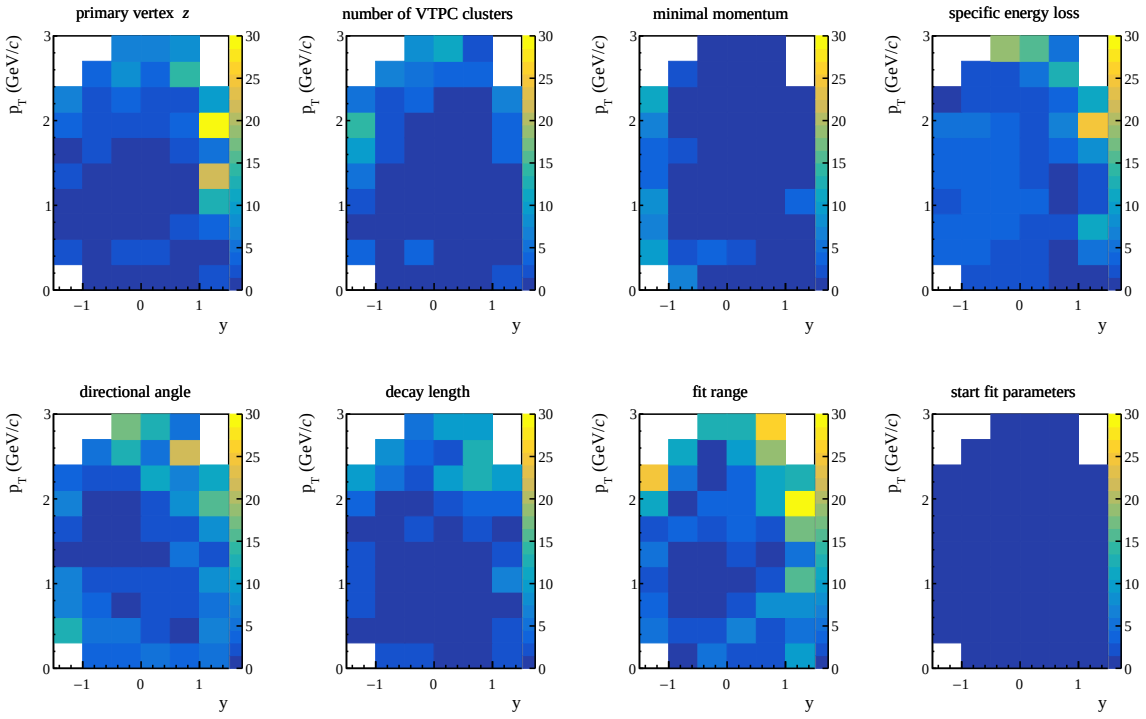

Figure 3.16: Contributions of selection criteria to the final systematic uncertainty of double-differential $y - p_T$ spectra of Λ baryons produced in central Ar+Sc collisions at 75A GeV/c beam momentum.

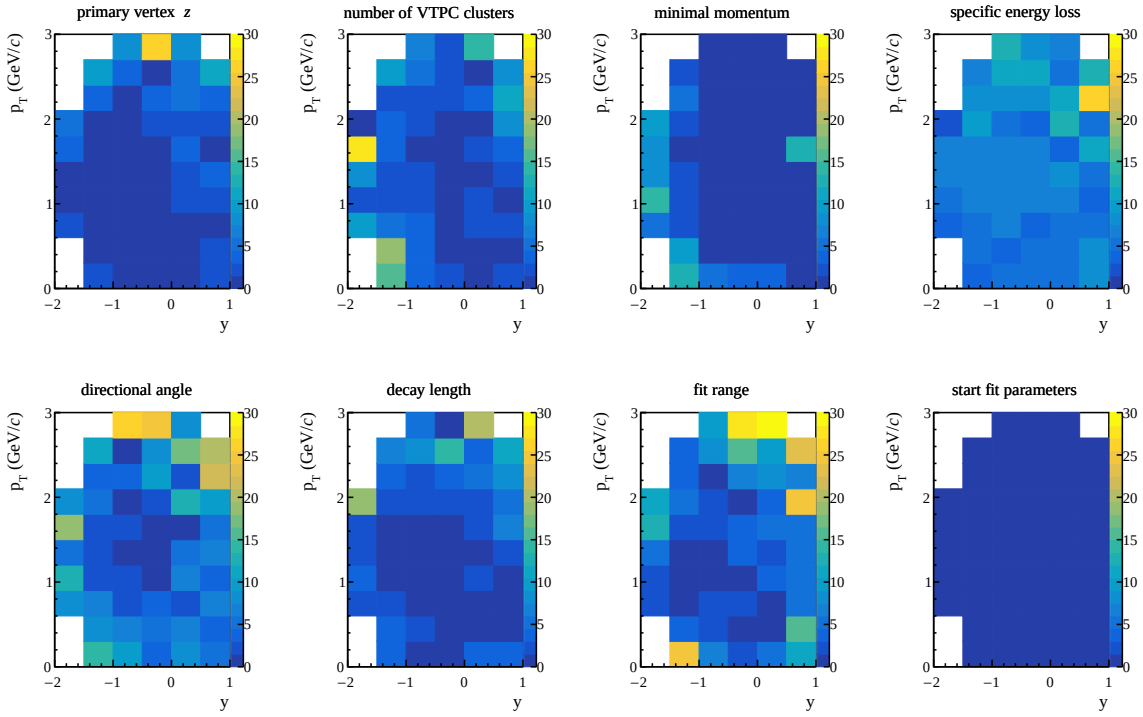

Figure 3.17: 150A GeV/c

Figure 3.18: Contributions of selection criteria to the final systematic uncertainty of double-differential $y - p_T$ spectra of Λ baryons produced in central Ar+Sc collisions at 150A GeV/c beam momentum.

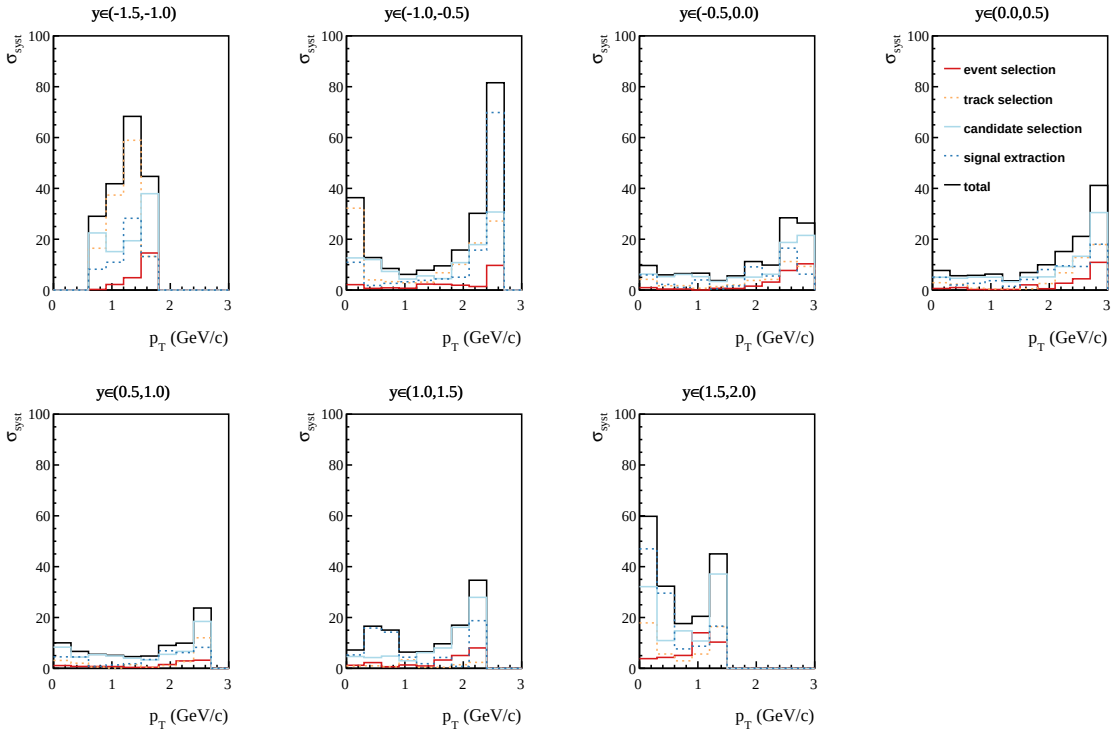

Figure 3.19: Contributions of selection criteria groups to the final systematic uncertainty of transverse momentum spectra in rapidity slices of Λ baryons produced in central Ar+Sc collisions at 40A GeV/c beam momentum.

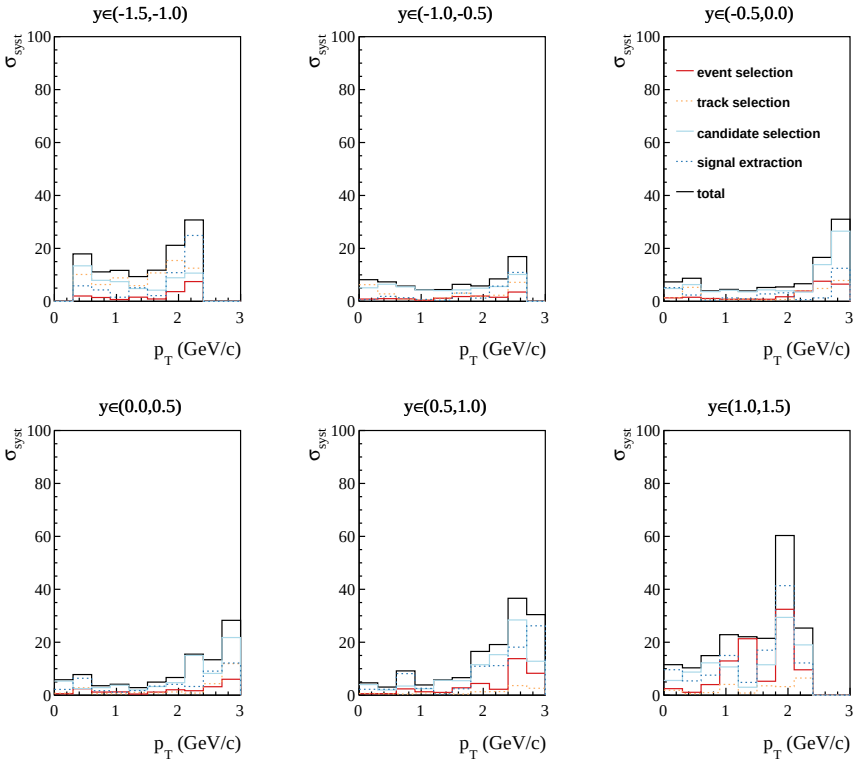

Figure 3.20: Contributions of selection criteria groups to the final systematic uncertainty of transverse momentum spectra in rapidity slices of Λ baryons produced in central Ar+Sc collisions at 75A GeV/c beam momentum.

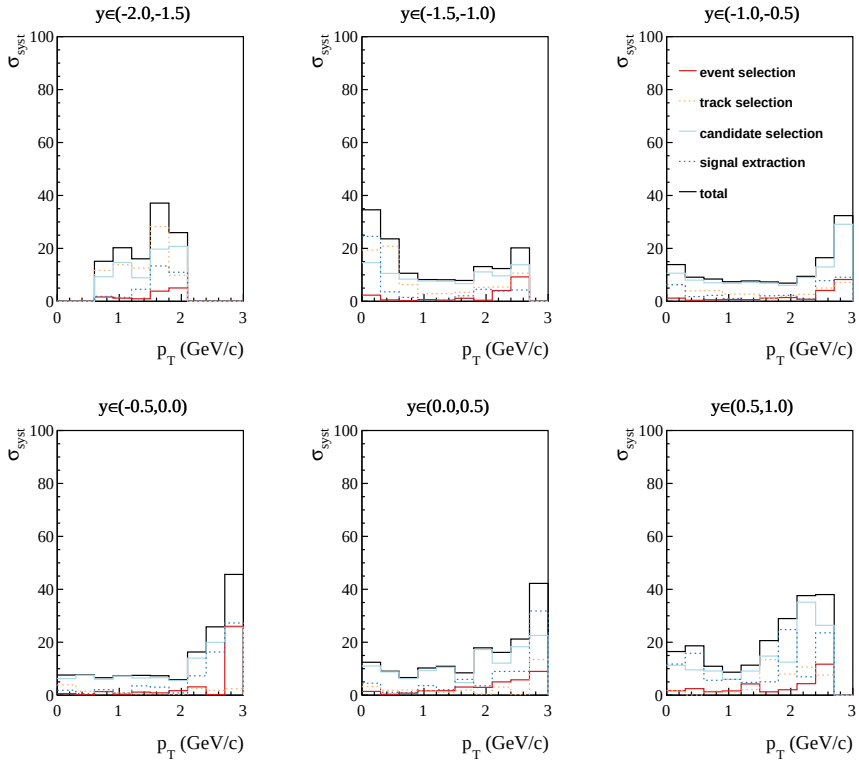

Figure 3.21: Contributions of selection criteria groups to the final systematic uncertainty of transverse momentum spectra in rapidity slices of Λ baryons produced in central Ar+Sc collisions at 150A GeV/c beam momentum.

3.8 Quality checks

3.8.1 Armenteros-Podolanski plot

A commonly used technique to distinguish between the types of reconstructed V^0 candidates is through the Armenteros-Podolanski plot [75]. It is a two-dimensional plot, which shows the longitudinal momentum asymmetry α_{Arm} versus transverse momentum p_{TArm} of the V^0 candidate decay products. The quantity α_{Arm} is calculated as follows:

$$\alpha_{Arm} = \frac{p_L^+ - p_L^-}{p_L^+ + p_L^-} , \tag{3.15}$$

where p_L^+ and p_L^- are longitudinal momenta of the V^0 candidate decay products relative to the V^0 candidate momentum, as shown in Fig. 3.22. Similarly, the transverse momentum p_{TArm} is defined with respect to the V^0 candidate momentum and illustrated in the same figure.

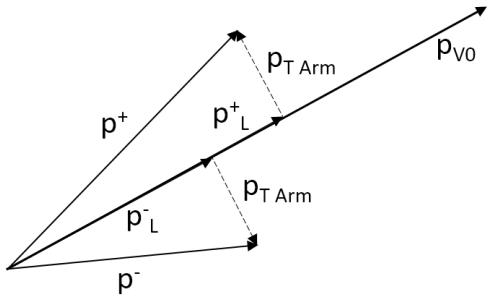

Figure 3.22: Example V^0 candidate decay construing the variable definitions for α_{Arm} and p_{TArm} calculation.

Theoretically allowed values of α_{Arm} and p_{TArm} form half-ellipses with the centre determined by the mass difference between the V^0 candidate decay products. In the case of K_S^0 meson decay to $\pi^+\pi^-$, the decay products have the same mass, thus, the ellipse centre is found at 0. For Λ ($\overline{\Lambda}$) baryon decays to $p\pi^-$ ($\overline{p}\pi^+$), the substantial mass difference between the decay products results in ellipses centred at ± 0.8.

Additionally, the Armenteros-Podolanski plot can be used to verify the efficiency of the proposed selection, as the half-ellipse originating from the given type of V^0 candidates becomes more prominent. As illustrated in Fig. 3.23, the minimum mo-

mentum selection (discussed in Sec. 3.3) significantly reduces the background in the Λ baryon mass region. The final Armenteros-Podolanski plots for Ar+Sc collisions at 40A, 75A, and 150A GeV/c after applying all selection criteria are shown in Fig. 3.24.

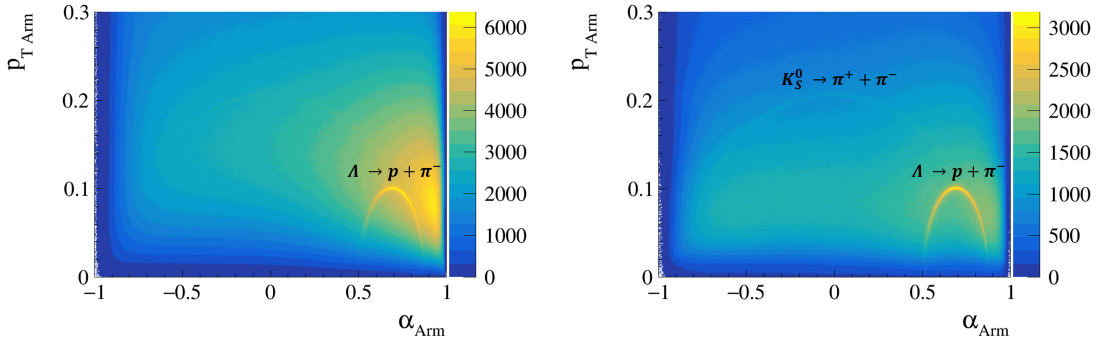

Figure 3.23: Armenteros-Podolanski plots for accepted V^0 candidates in central Ar+Sc collisions at 75A GeV/c after event and track selection, and specific energy loss selection without (*left*) and with (*right*) minimum momentum selection. The half-ellipse seen in the bottom right originates from the $\Lambda \to p\pi^-$ decays, while the larger half-ellipse seen in the centre comes from $K^0_S \to \pi^+\pi^-$ decays.

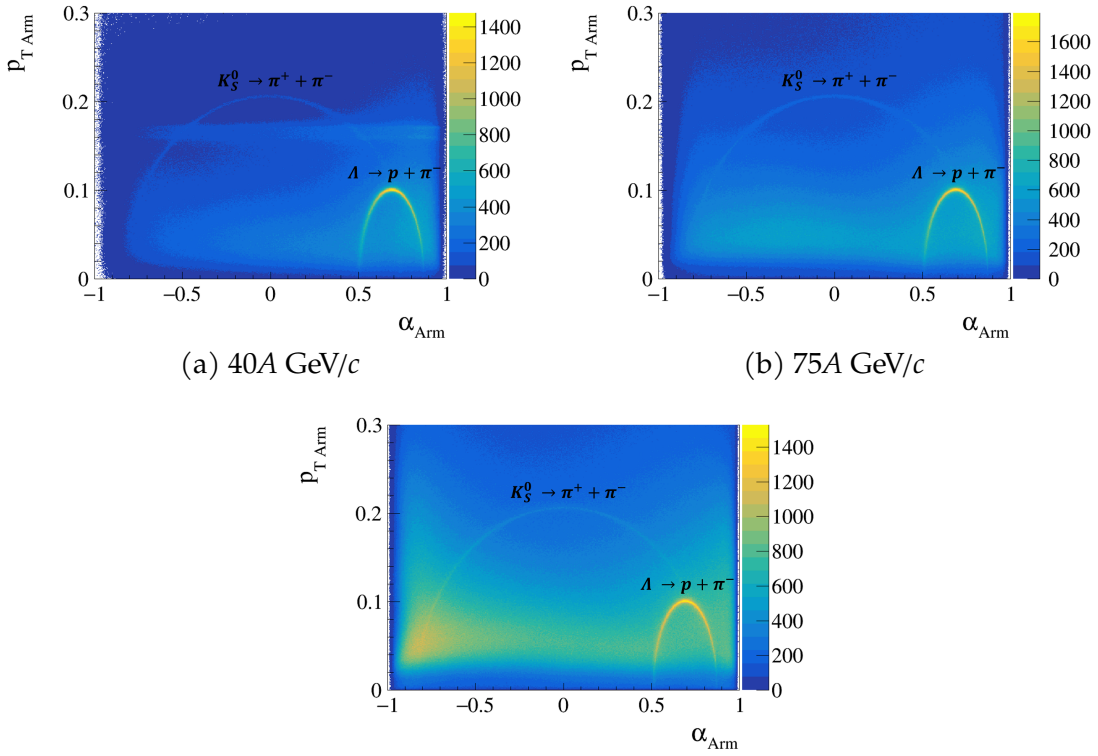

(a) 40A GeV/c (b) 75A GeV/c

(c) 150A GeV/c

Figure 3.24: Armenteros-Podolanski plots for accepted V^0 candidates in central Ar+Sc collisions at (a) 40A, (b) 75A, and (c) 150A GeV/c after event, track and candidate selection (including rapidity dependent selections). The half-ellipse seen in the bottom right originates from the $\Lambda \to p\pi^-$ decays, while the larger half-ellipse seen in the centre comes from $K^0_S \to \pi^+\pi^-$ decays.

3.8.2 Mean lifetime measurement

The reliability of the V^0 candidate reconstruction and the selection and correction procedures can be further validated by studying the decay time distribution of the accepted candidates. The analysis procedure is similar to the analysis conducted in the $y - p_T$ phase space described throughout this chapter. However, in this case, the phase space is divided into bins based on rapidity and lifetime. The decay time of each Λ candidate is calculated as:

$$c\tau = \frac{\Delta L}{\beta\gamma} \,, \tag{3.16}$$

where ΔL is the decay length as defined in Sec. 3.3, $\beta = v/c$ is the velocity expressed relatively to the speed of light in vacuum, and γ is the Lorentz factor. Afterwards, the obtained value is normalized to the world-average mean lifetime value $c\tau_\Lambda = 7.89\,cm$ taken from the PDG [6].

The rapidity binning follows the same approach as described in Sec. 3.4, while there are 8 bins within the range $c\tau/c\tau_\Lambda \in [1.0; 8.0]$ for the decay time. The signal yield is extracted from the invariant mass distribution fit for each $y - c\tau/c\tau_\Lambda$ bin individually. The bin is accepted for analysis if there is a sufficiently large sample of Λ candidates to perform a meaningful fit. The corrected decay time distributions are fitted by an exponential distribution, and the obtained mean lifetime ratios are checked (should be at unity by definition).

The corrected decay time distributions for Ar+Sc collisions at 40A, 75A, and 150A GeV/c are shown in Figs. 3.25, 3.26, and 3.27, respectively. Exponential functions are fitted to the distributions to determine the mean lifetime within each rapidity bin. The obtained values as a function of rapidity are illustrated in Fig. 3.28 and show a good agreement with unity within the uncertainties.

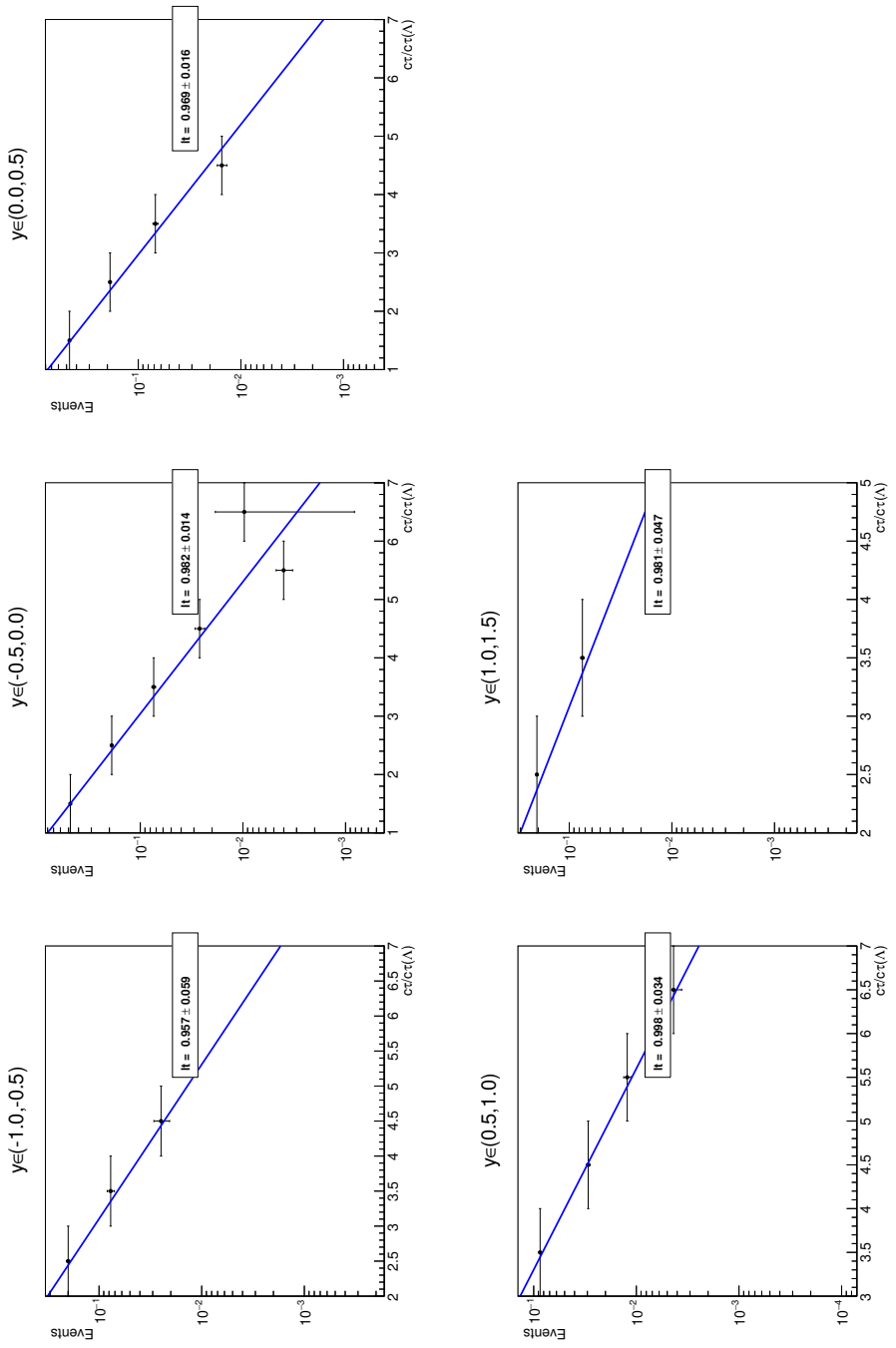

Figure 3.25: Corrected decay time distributions of Λ baryons produced in central Ar+Sc collisions at 40A GeV/c with statistical uncertainties. The blue lines represent the exponential fits performed to determine the mean lifetimes denoted in the fit parameter box as lt.

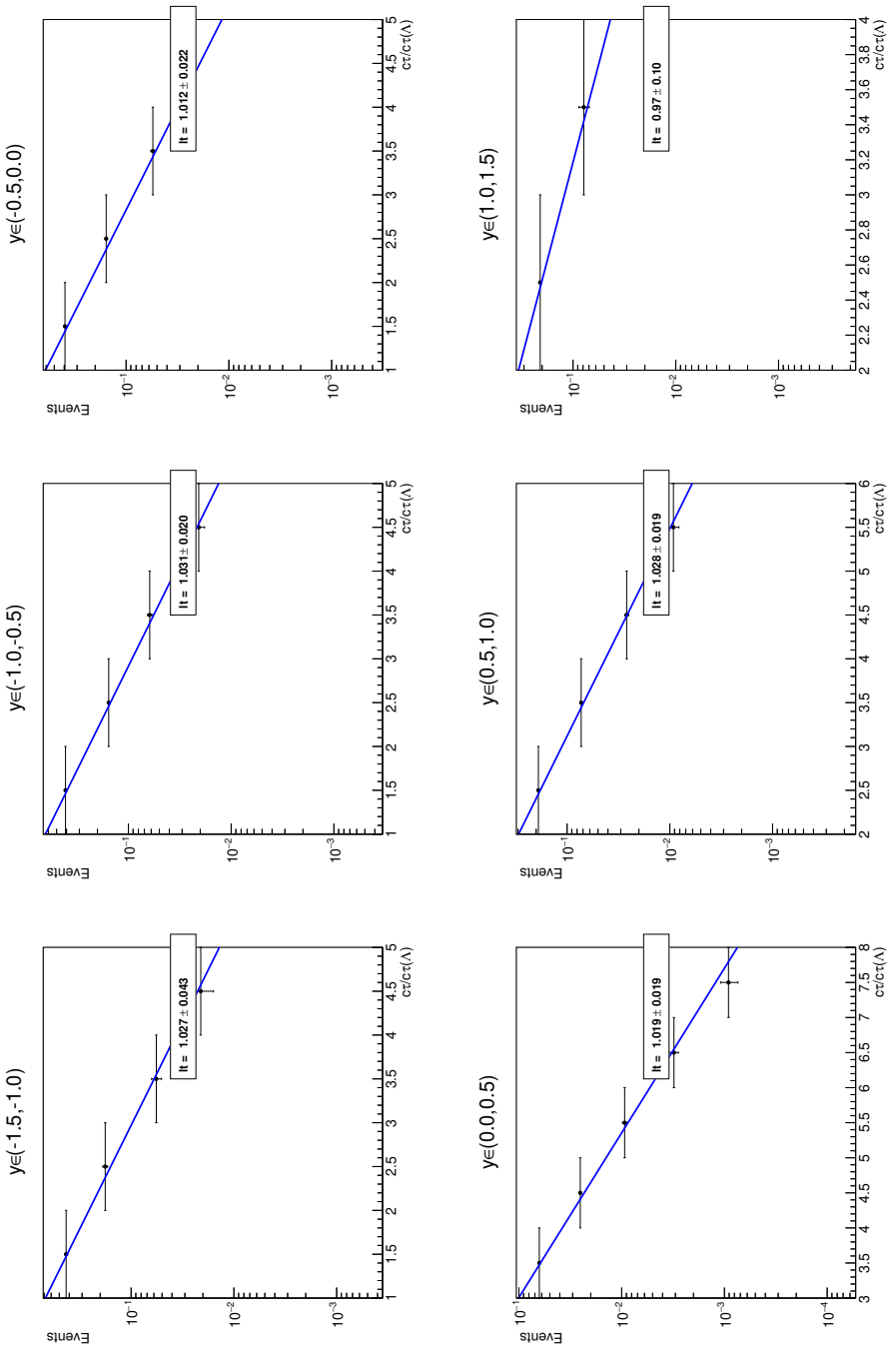

Figure 3.26: Corrected decay time distributions of Λ baryons produced in central Ar+Sc collisions at 75A GeV/c with statistical uncertainties. The blue lines represent the exponential fits performed to determine the mean lifetimes denoted in the fit parameter box as lt.

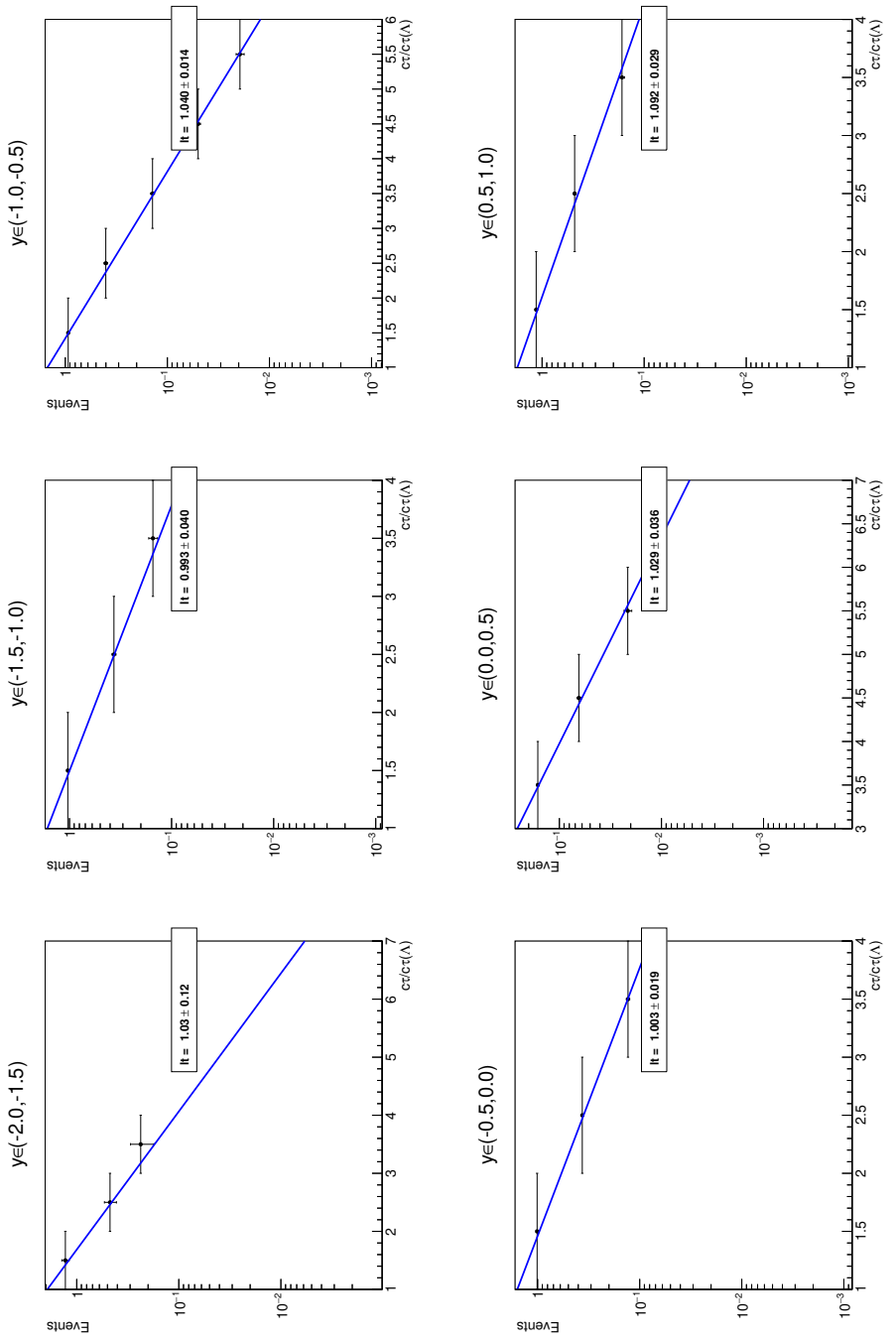

Figure 3.27: Corrected decay time distributions of Λ baryons produced in central Ar+Sc collisions at 150A GeV/c with statistical uncertainties. The blue lines represent the exponential fits performed to determine the mean lifetimes denoted in the fit parameter box as lt.

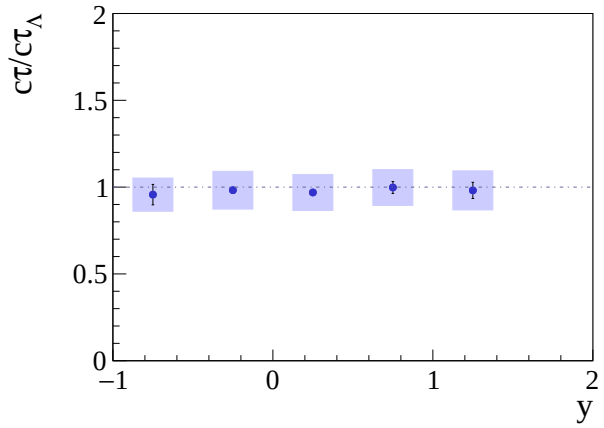

(a) 40*A* GeV/*c*

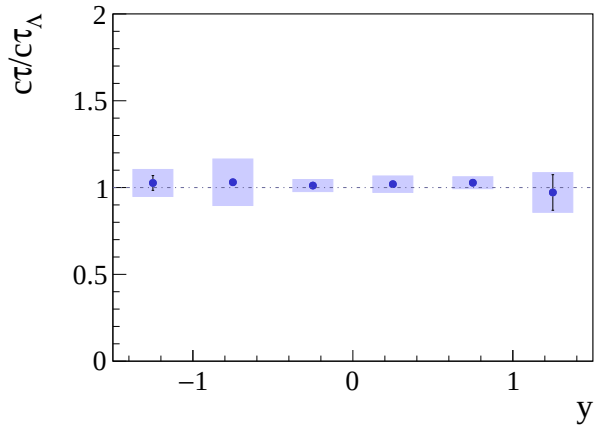

(b) 75*A* GeV/*c*

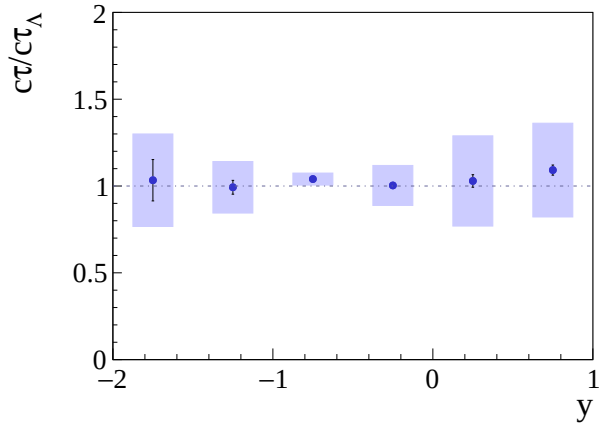

(c) 150*A* GeV/*c*

Figure 3.28: Mean lifetime normalized to the PDG value [6] of Λ baryons produced in central Ar+Sc collisions at (a) 40*A*, (b) 75*A*, and (c) 150*A* GeV/*c*. The statistical uncertainties are depicted as vertical bars, while the systematic uncertainties are presented as shaded boxes.

Chapter 4

Results

This chapter presents experimental results on Λ baryon production in 0-10% most central Ar+Sc collisions at 40A, 75A, and 150A GeV/c ($\sqrt{s_{NN}}$ = 8.77, 11.94, and 17.3 GeV, respectively). Firstly, the double-differential spectra in $y - p_T$ bins are shown in Sec. 4.1, followed by the one-dimensional transverse momentum and rapidity spectra in Sec. 4.2 and 4.3, respectively. The latter section also includes the results on the mean multiplicity of Λ baryons. The obtained results are then compared to selected model predictions in Sec. 4.4 and available world data in Sec. 4.5.

4.1 Double-differential spectra

The double-differential spectra of Λ baryons produced in central Ar+Sc collisions in $y - p_T$ phase space are obtained following the methodology outlined in Sec. 3.4 and subsequently corrected for losses due to the geometrical acceptance of the detector, reconstruction inefficiency, selections applied in the analysis, branching ratio, and feed-down from the decays of heavier hyperons as explained in Sec. 3.6. The resulting corrected spectra of Λ baryons produced in central Ar+Sc collisions at 40A, 75A, and 150A GeV/c are shown along with their statistical and systematic uncertainties in Figs. 4.1, 4.2, and 4.3, respectively.

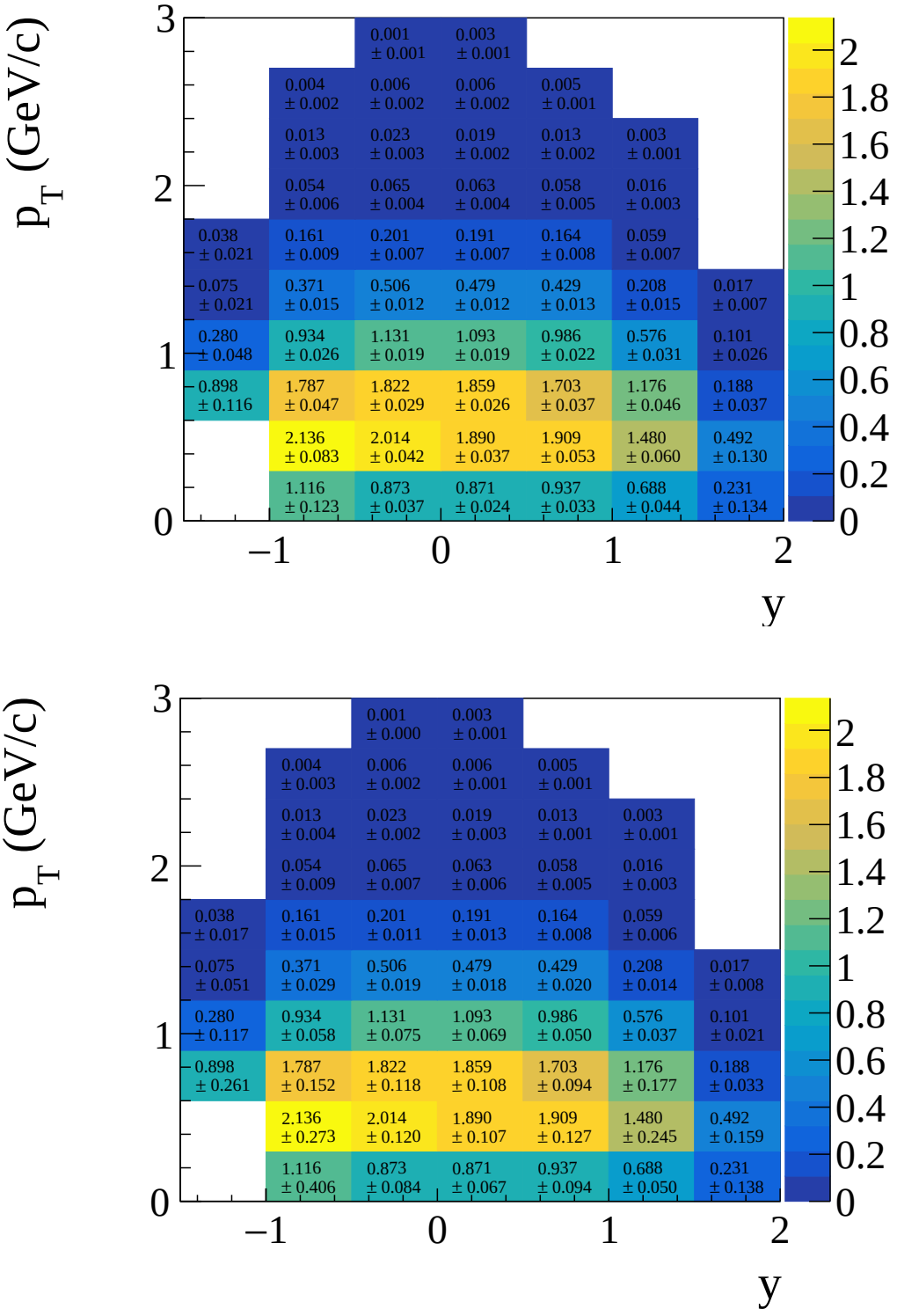

Figure 4.1: Double-differential $y - p_T$ spectra of Λ baryons produced in central Ar+Sc collisions at 40A GeV/c beam momentum with statistical (*top*) and systematic (*bottom*) uncertainties provided in the form: $(d^2n/dydp_T \pm \sigma_{stat})$ or $(d^2n/dydp_T \pm \sigma_{syst})$, respectively.

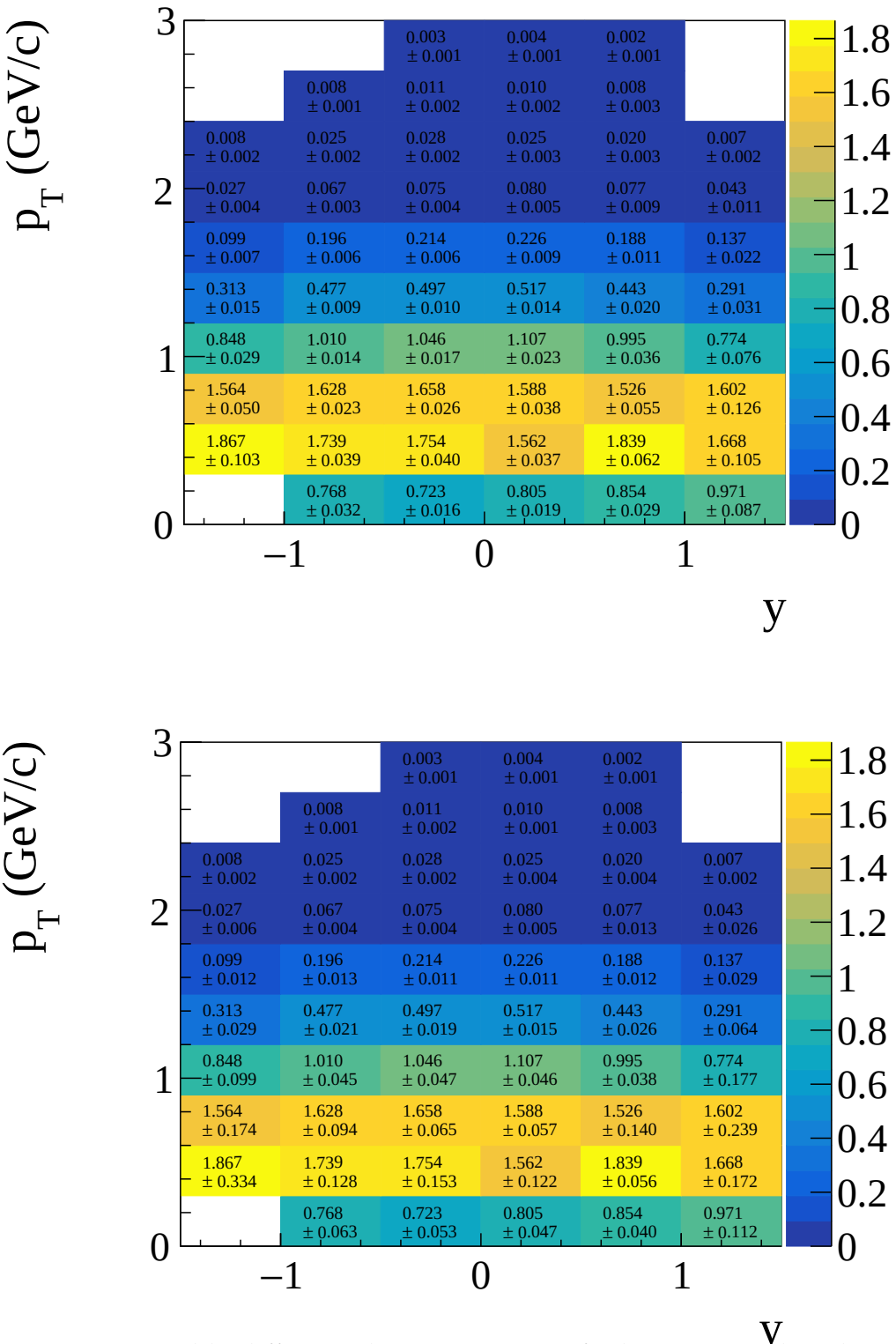

Figure 4.2: Double-differential $y - p_T$ spectra of Λ baryons produced in central Ar+Sc collisions at 75A GeV/c beam momentum with statistical (*top*) and systematic (*bottom*) uncertainties provided in the form: $(d^2n/dydp_T \pm \sigma_{stat})$ or $(d^2n/dydp_T \pm \sigma_{syst})$, respectively.

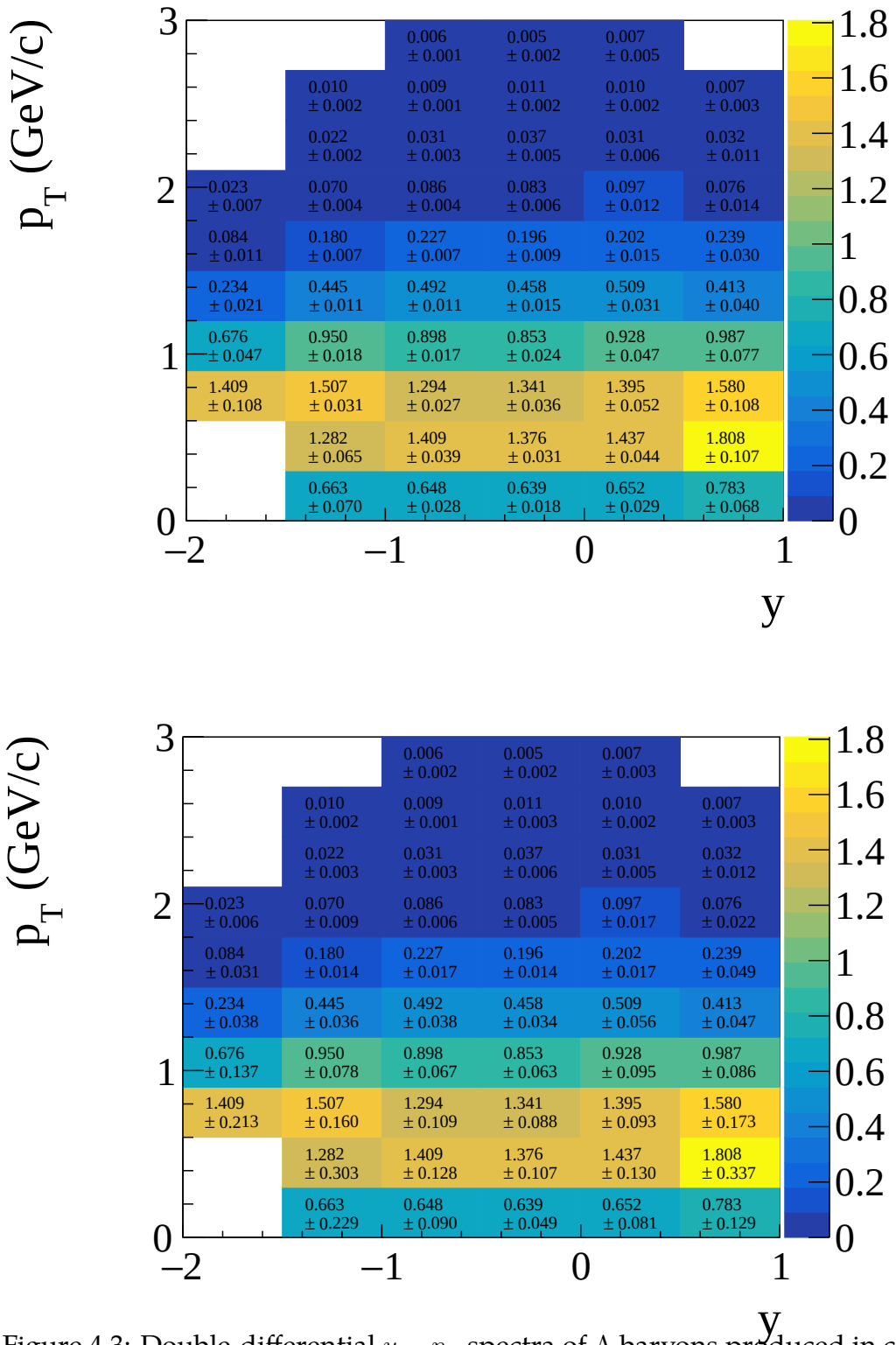

Figure 4.3: Double-differential $y - p_T$ spectra of Λ baryons produced in central Ar+Sc collisions at 150A GeV/c beam momentum with statistical (*top*) and systematic (*bottom*) uncertainties provided in the form: $(d^2n/dydp_T \pm \sigma_{stat})$ or $(d^2n/dydp_T \pm \sigma_{syst})$, respectively.

4.2 Transverse momentum distributions

The one-dimensional transverse momentum spectra of Λ baryons produced in central Ar+Sc collisions in rapidity slices are shown in Figs. 4.4, 4.5, and 4.6 for 40A, 75A, and 150A GeV/c, respectively. To estimate the yield in the unmeasured high p_T range, the function defined by the following equation is fitted to the spectra using the χ^2 method:

$$f(p_T) = S \cdot p_T \cdot \exp\left(-\frac{p_T^2 + m_0^2}{T}\right) , \tag{4.1}$$

where S represents the normalization factor, T denotes the inverse slope parameter, and m_0 is the known Λ baryon mass as per Ref. [6]. Particularly, this parametrization provides the values of the inverse slope parameter T, which in hydrodynamical models is proportional to the kinetic freeze-out temperature, modified due to the transverse flow [76].

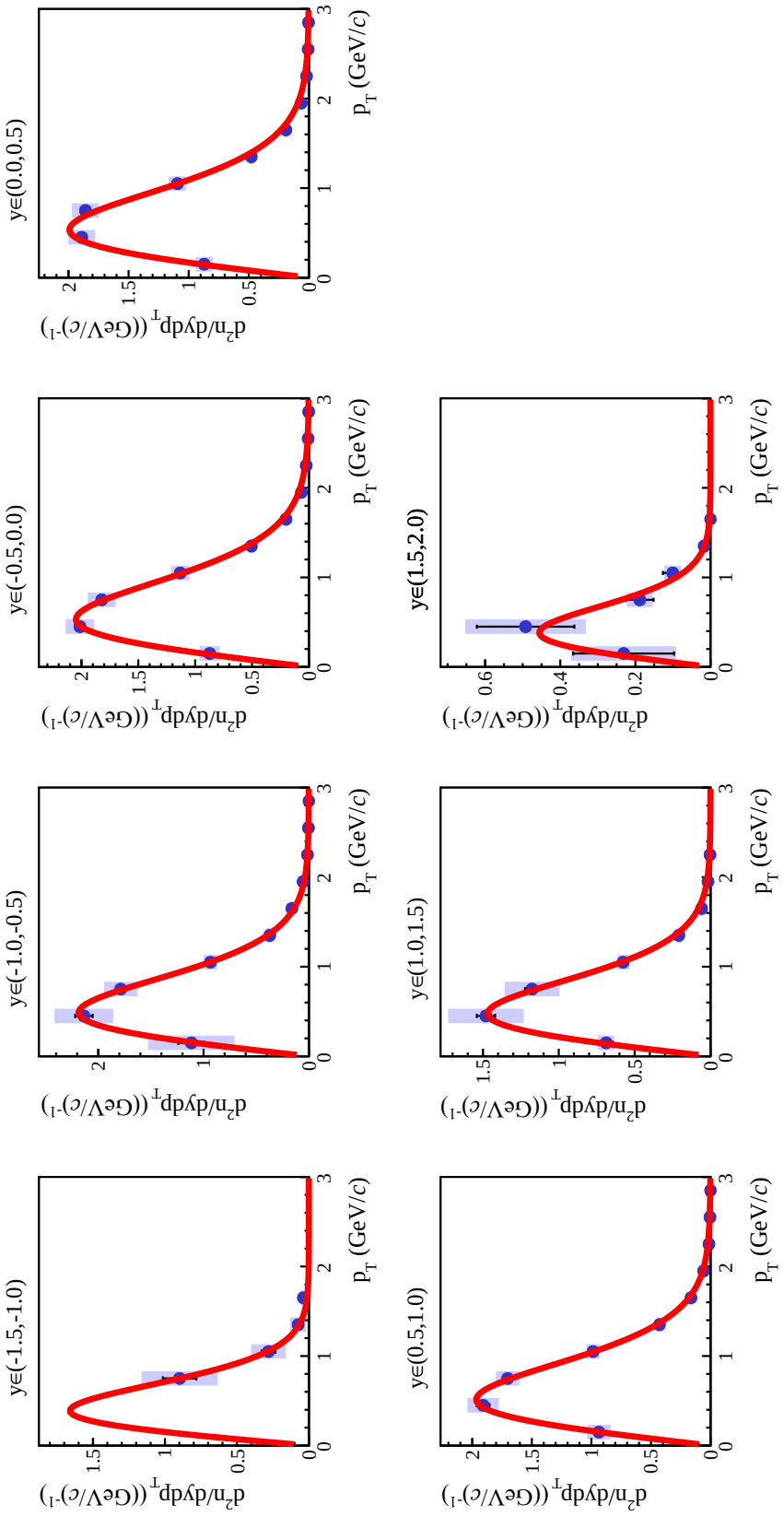

Figure 4.4: Transverse momentum spectra in rapidity slices of Λ baryons produced in central Ar+Sc collisions at 40A GeV/c beam momentum. The statistical uncertainties are depicted as vertical bars, while the systematic uncertainties are presented as shaded boxes. The red lines represent the fits as given by Eq. 4.1.

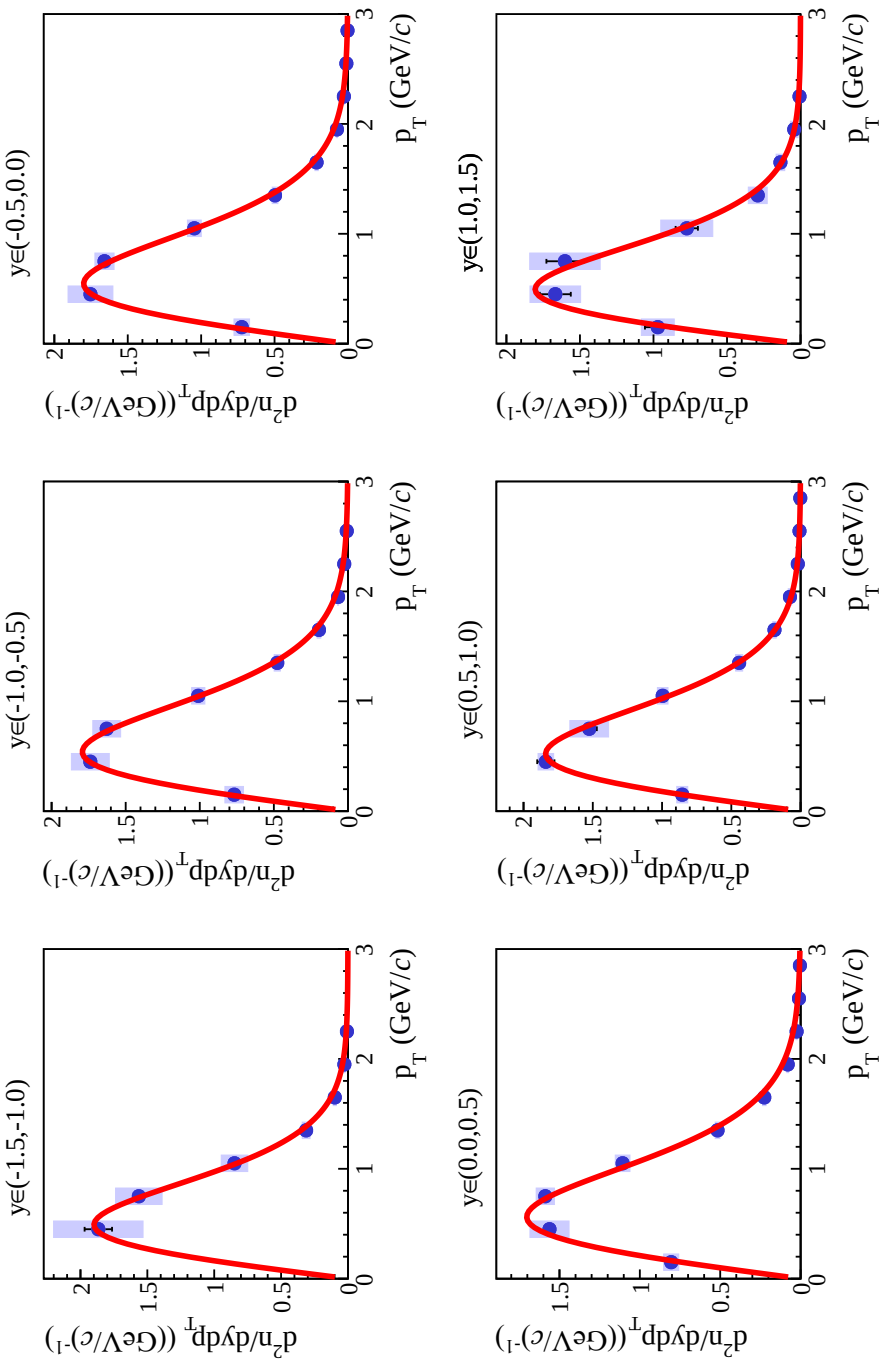

Figure 4.5: Transverse momentum spectra in rapidity slices of Λ baryons produced in central Ar+Sc collisions at 75A GeV/c beam momentum. The statistical uncertainties are depicted as vertical bars, while the systematic uncertainties are presented as shaded boxes. The red lines represent the fits as given by Eq. 4.1.

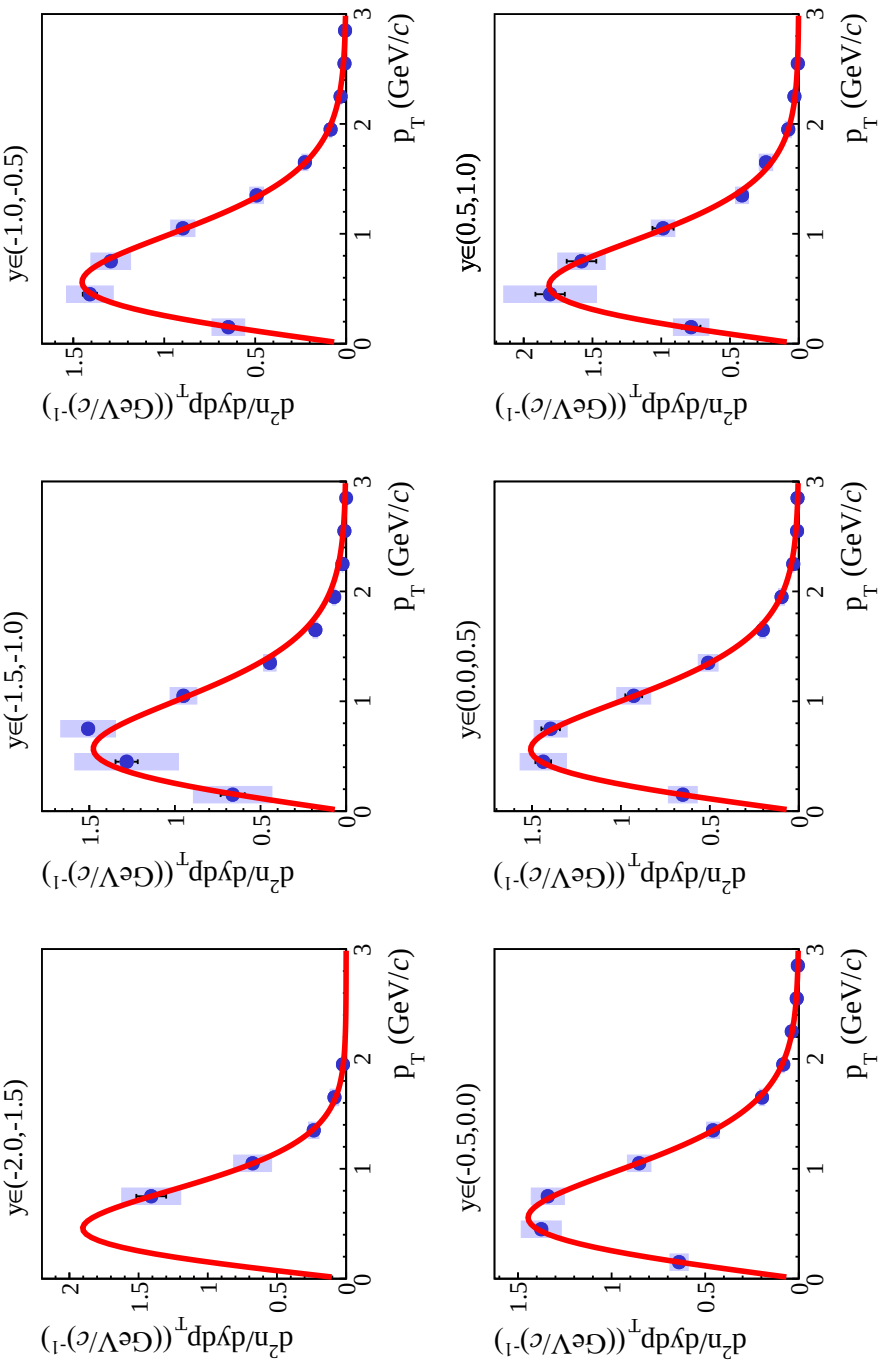

Figure 4.6: Transverse momentum spectra in rapidity slices of Λ baryons produced in central Ar+Sc collisions at 150A GeV/c beam momentum. The statistical uncertainties are depicted as vertical bars, while the systematic uncertainties are presented as shaded boxes. The red lines represent the fits as given by Eq. 4.1.

4.3 Rapidity distributions and mean multiplicities

The one-dimensional rapidity spectra of Λ baryons produced in central Ar+Sc collisions at 40A, 75A, and 150A GeV/c are depicted in Fig. 4.7. The distributions are derived from the transverse momentum spectra as the sum of the values in the measured region and the integral of the function 4.1 in the unmeasured region for each rapidity bin separately. The statistical uncertainty in a given rapidity bin is determined as the sum in quadrature of statistical uncertainties of the measured points and the uncertainty of the fitted function integral in the unmeasured region as provided by the Root framework [77]. The systematic uncertainty is calculated as explained in Sec. 3.7, and, additionally, half of the total contribution to the yield originating from the extrapolation is added in quadrature to address any potential bias coming from the selection of function 4.1.

The mean multiplicity is computed as the sum of the measured values scaled, assuming that the yield ratio between measured and unmeasured regions is consistent between the experimental data and Monte Carlo (Epos1.99) simulated data. The statistical uncertainty is then calculated as the sum in quadrature of the statistical uncertainties of the measured points, scaled under the same assumption. The systematic uncertainty is estimated as explained in Sec. 3.7, and, additionally, half of the extrapolated integral is added in quadrature to address the potential bias from the distribution shape in the Epos1.99 model. Table 4.1 summarizes the obtained numerical values of the mid-rapidity yield ($|y| < 0.5$) along with the mean multiplicities for each beam momentum value.

Table 4.1: Numerical values of the mid-rapidity yields ($|y| < 0.5$) and mean multiplicities of Λ baryons produced in central Ar+Sc collisions with statistical and systematic uncertainties provided in the form: $\Lambda \pm \sigma_{stat} \pm \sigma_{syst}$.

p_{beam} (GeV/c)	$dN(\Lambda)/dy\|_{y=0}$	$\langle\Lambda\rangle$
40A	$1.97 \pm 0.02 \pm 0.10$	$5.49 \pm 0.06 \pm 0.24$
75A	$1.79 \pm 0.02 \pm 0.07$	$6.44 \pm 0.05 \pm 0.62$
150A	$1.54 \pm 0.02 \pm 0.10$	$6.43 \pm 0.06 \pm 0.88$

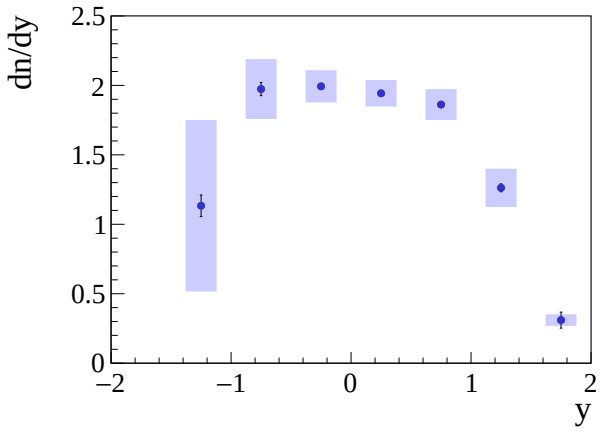

(a) 40A GeV/c

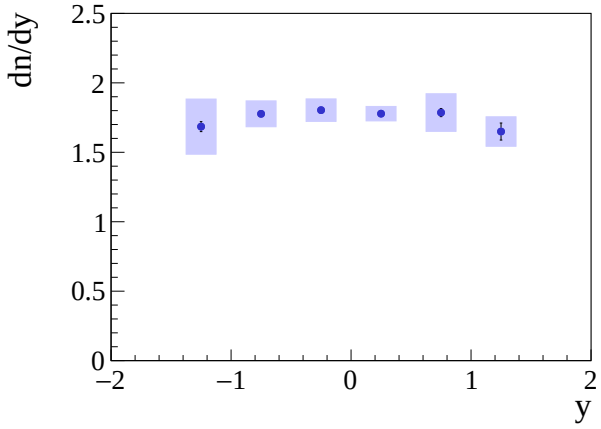

(b) 75A GeV/c

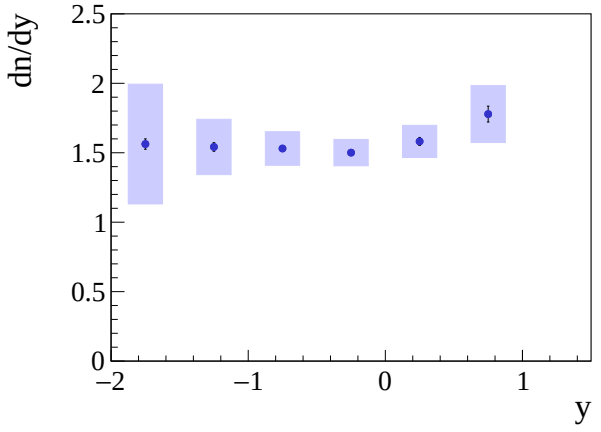

(c) 150A GeV/c

Figure 4.7: Rapidity spectra of Λ baryons produced in central Ar+Sc collisions at (a) 40A, (b) 75A, and (c) 150A GeV/c. The statistical uncertainties are depicted as vertical bars, while the systematic uncertainties are presented as shaded boxes.

4.4 Comparison to particle production models

This section presents a comparison of the obtained experimental results with selected particle production models: EPOS1.99 [65, 66] and SMASH 2.0 [78, 79]. The models differ in the physics mechanism employed to describe the heavy-ion interactions. Particularly, in EPOS1.99, the reaction proceeds from the excitation of strings according to Gribov-Regge theory to string fragmentation into hadrons. On the other hand, SMASH uses a hadronic transport approach, where the free parameters of the string excitation and decay are tuned to match the experimental measurements in proton-proton collisions.

First of all, the comparison of the inverse slope parameter values with model predictions as a function of rapidity is shown in Fig. 4.8. The inverse slope parameter values are obtained from fits to the transverse momentum spectra as defined by Eq. 4.1. One can see that both models underestimate the inverse slope parameter in the full rapidity range, although the shape of the distribution provided by the SMASH is visibly close to the experimental results.

Following this, the comparison of the rapidity spectra of Λ baryons produced in central Ar+Sc collisions with model predictions is illustrated in Fig. 4.9. In the case of 40A GeV/c, the EPOS1.99 underestimates the Λ baryon production in the mid-rapidity region, although it shows a good agreement in the tails of the rapidity distribution. Similarly, at 75A and 150A GeV/c, the available experimental results are underestimated by EPOS1.99. However, no direct comparison is possible in the outermost rapidity regions. The SMASH tends to significantly underestimate the Λ baryon production for all analyzed beam momenta values, which is also the case for the production of charged ($\pi^{\pm}, K^{\pm}, p$ and $\overline{p}$ [73]) and neutral (K^0_S [80]) particles in Ar+Sc collisions.

Furthermore, the mid-rapidity yields and the mean multiplicities are compared with the model predictions in Fig. 4.10. The EPOS1.99 underestimates either the mid-rapidity yields or mean multiplicities, though the model predictions almost match with experimental results towards the highest energy. However, same as for the rapidity spectra, the SMASH predicts significantly lower values for both quantities in the full energy range.

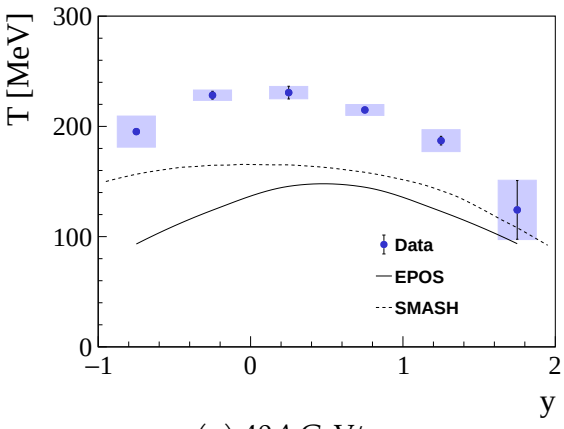

(a) 40A GeV/c

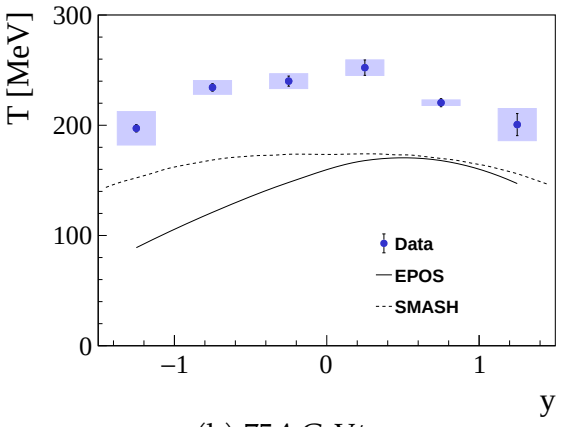

(b) 75A GeV/c

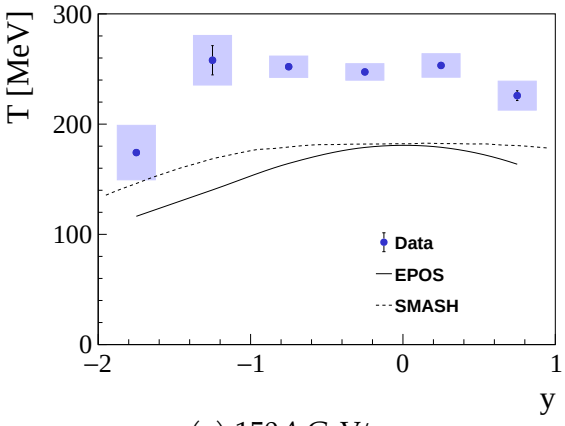

(c) 150A GeV/c

Figure 4.8: Comparison of the inverse slope parameter T of transverse momentum spectra of Λ baryons produced in central Ar+Sc collisions at (a) 40A, (b) 75A, and (c) 150A GeV/c with predictions of Epos1.99 [65, 66] and Smash [78, 79] models. For the data, the statistical uncertainties are depicted as vertical bars, while the systematic uncertainties are presented as shaded boxes. Model uncertainties are neglected.

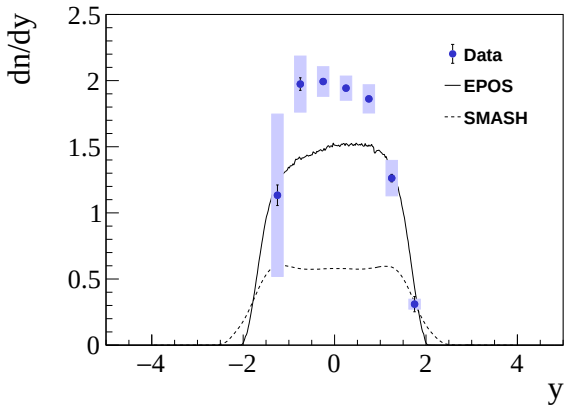

(a) 40*A* GeV/*c*

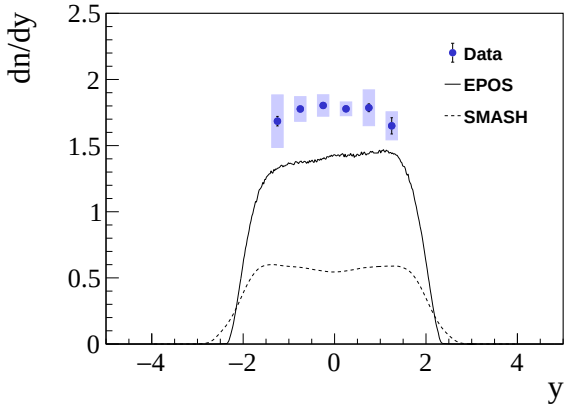

(b) 75*A* GeV/*c*

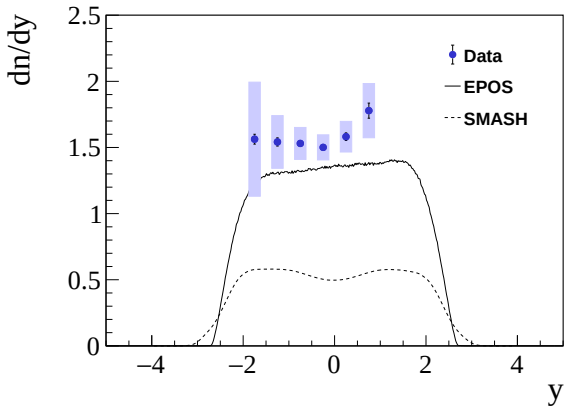

(c) 150*A* GeV/*c*

Figure 4.9: Comparison of rapidity spectra of Λ baryons produced in central Ar+Sc collisions at (a) 40*A*, (b) 75*A*, and (c) 150*A* GeV/*c* with predictions of Epos1.99 [65, 66] and Smash [78, 79] models. For the data, the statistical uncertainties are depicted as vertical bars, while the systematic uncertainties are presented as shaded boxes. Model uncertainties are neglected.

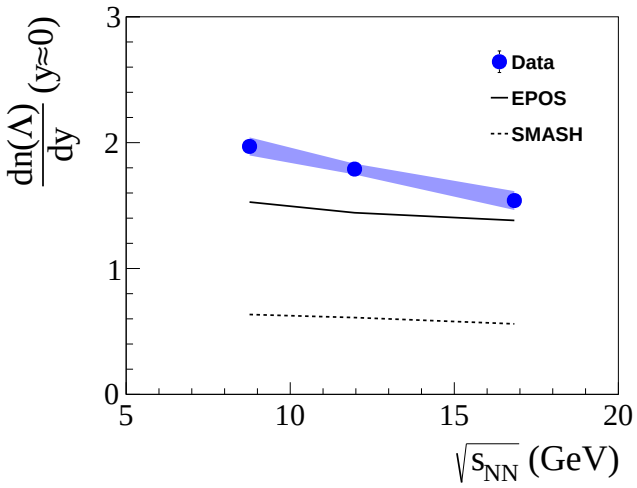

(a)

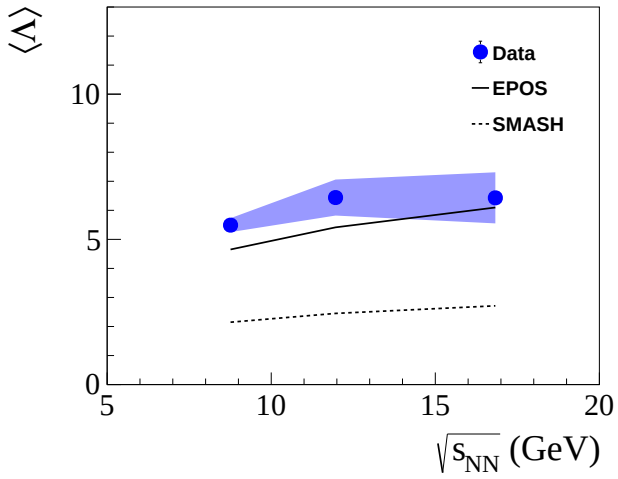

(b)

Figure 4.10: Comparison of the energy dependence of (a) mid-rapidity yields, and (b) mean multiplicities of Λ baryons produced in central Ar+Sc collisions at 40A, 75A, and 150A GeV/c with predictions of Epos1.99 [65, 66] and Smash [78, 79] models. For the data, the systematic uncertainties are presented as a shaded band. Model uncertainties are neglected.

4.5 Comparison to world data

This section provides a comparison of the obtained experimental results to available world data. The energy dependence of various properties of strangeness production in Ar+Sc collisions is compared with the available data for p+p ([81–114]), Ar+Sc ([73]), C+C ([115, 116]), Si+Si ([115, 116]), Ar+KCl ([117–119]), Au+Au ([120–139]), and Pb+Pb ([42, 43, 140–142]) collisions. The data originate from experiments conducted at the AGS, SPS, and RHIC accelerators. Additionally, the system size dependence is explored where possible, comparing results across different collision systems at the same or close momenta.

The corresponding comparison of the inverse slope parameter T of Λ baryon transverse momentum spectra (as defined in Eq. 4.1) at mid-rapidity is presented in Fig. 4.11 as a function of the collision energy. The energy dependence of the inverse slope parameter in Ar+Sc and Ar+KCl collisions, systems of comparable size, shows a rise followed by a plateau towards the highest SPS energy, similarly to the trend in Pb+Pb data. The values mentioned above are slightly lower than those in Pb+Pb collisions but significantly higher than in p+p. This suggests that the kinetic freeze-out temperature in Ar+Sc collisions is closer to that in Pb+Pb (a large collision system) than in p+p (a small collision system).

In turn, Fig. 4.12 shows the system size dependence of the inverse slope parameter of Λ baryons at a beam momentum of 150A GeV/c, where the most extensive world data is available. The mean number of wounded nucleons $\langle W \rangle$ is selected as the measure of the system size. One can see that the inverse slope parameter depends approximately linearly on the size of the collision system.

The rapidity spectra of Λ baryons produced in different collision systems are compared in Fig. 4.13 across all analyzed beam momenta. In cases where data for the exact beam momentum was unavailable, the data from the closest available beam momentum is used. Thus, the results from Ar+Sc collisions at 75A GeV/c are compared to the results from p+p collisions at 69A GeV/c [89], and the results from Pb+Pb collisions at 80A GeV [140]. Similarly, the results from Ar+Sc collisions at 150A GeV/c are compared to the results from other collision systems at 158A GeV/c [100, 115, 140]. The spectra are normalized by the mean number of wounded nucleons in the given collision system. The corresponding spectra for Ar+Sc and Pb+Pb collisions come closer with increasing beam momentum, with prominent similarities at 150A GeV/c,

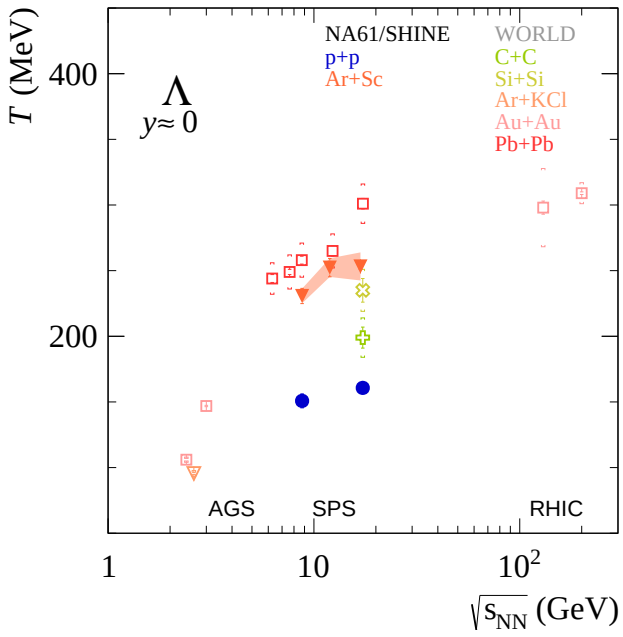

Figure 4.11: Energy dependence of inverse slope parameter T of Λ baryon transverse momentum spectra at mid-rapidity. Results for p+p ([100, 101]), Ar+Sc (this thesis), C+C ([116]), Si+Si ([116]), Ar+KCl ([117]), Au+Au ([121, 127, 129]), and Pb+Pb ([140]) are shown.

which points to a similar transition from baryon stopping to baryon transparency [143, 144] for these collision systems. In addition, at the highest beam momentum, the said rapidity spectra closely resemble the distribution for Si+Si collisions. At the same time, spectra for lighter systems, such as p+p and C+C, exhibit distinctly lower values.

The energy dependencies of the mid-rapidity yield and mean multiplicity of Λ baryons, along with available world data, are presented in Figs. 4.14 and 4.15, respectively. Both quantities reach a plateau within the SPS energy range regardless of the collision system size. The values for Ar+Sc and Si+Si collisions are much closer to those observed in Au+Au and Pb+Pb collisions than in p+p and C+C collisions. This, together with previous observations, may suggest that the particle production mechanisms in these systems are comparable, whereas smaller systems, such as p+p and C+C, show different interaction dynamics.

Consequently, the system size dependence of mean multiplicity of Λ baryons is shown in Fig. 4.16 for all analyzed beam momenta. As previously mentioned, the mean number of wounded nucleons $\langle W \rangle$ serves as the measure of the system size. The WNM [33] prediction is also included to illustrate the expected linear scaling with

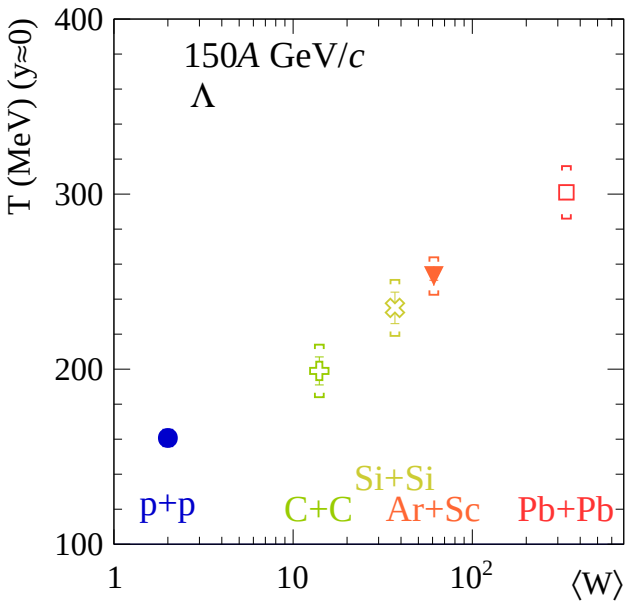

Figure 4.12: System size dependence of inverse slope parameter T of transverse momentum spectra at mid-rapidity of Λ baryons produced at 150A GeV/c. The mean number of wounded nucleons $\langle W \rangle$ is utilized as a system size measure. Results for p+p ([100, 101]), Ar+Sc (this thesis), C+C ([116]), Si+Si ([116]), and Pb+Pb ([140]) are shown.

respect to corresponding results for p+p collisions. For all beam momenta, the values for heavier systems, such as Si+Si, Ar+Sc and Pb+Pb, show a linear trend but are slightly above the WNM prediction.

Fig. 4.17 illustrates the energy dependence of the $\langle\Lambda\rangle/\langle\pi\rangle$ ratio, with $\langle\pi\rangle = 1.5 \cdot (\langle\pi^+\rangle + \langle\pi^-\rangle)$, where $\langle\pi^+\rangle$ and $\langle\pi^-\rangle$ are mean multiplicities of positively and negatively charged pions, respectively. The results for Pb+Pb collisions show a notable peak in the $\langle\Lambda\rangle/\langle\pi\rangle$ ratio at lower SPS energies, followed by a sharp value decline as the energy increases. It was reported that the peak is located in the same energy region as for the $\langle K^+\rangle/\langle\pi^+\rangle$ ratio, though it was arguable whether it can be attributed to the same effect [43, 140]. In contrast, for the p+p collisions, the $\langle\Lambda\rangle/\langle\pi\rangle$ ratio shows a modest rise, followed by a much more gradual decrease. To conclusively determine the existence of a maximum in results for $\langle\Lambda\rangle/\langle\pi\rangle$ ratio in Ar+Sc collisions, the measurement of Λ baryon production at lower beam momenta is necessary. Interestingly, no peak is observed in the $\langle K^+\rangle/\langle\pi^+\rangle$ ratio [73]. Overall, the observed decrease in measured values for Ar+Sc collisions lies between the trends seen in Pb+Pb and p+p collisions, with the degree of decrease being closer to that

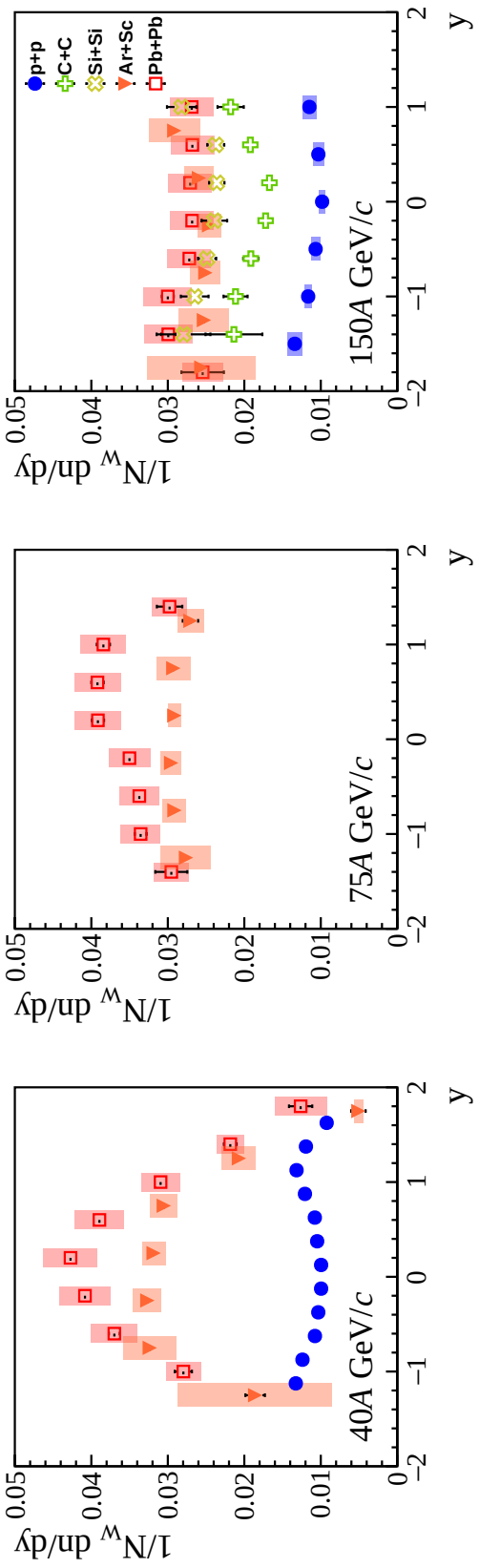

Figure 4.13: Comparison of rapidity spectra of Λ baryons produced in central Ar+Sc collisions at 40A (*left*), 75A (*middle*), and 150A GeV/c (*right*) with corresponding rapidity spectra in p+p ([100, 101]), C+C ([115]), Si+Si ([115]) and Pb+Pb ([140]) collisions. The spectra are scaled by the mean number of wounded nucleons N_W for a given collision system. The statistical uncertainties are depicted as vertical bars, while the systematic uncertainties are presented as shaded boxes.

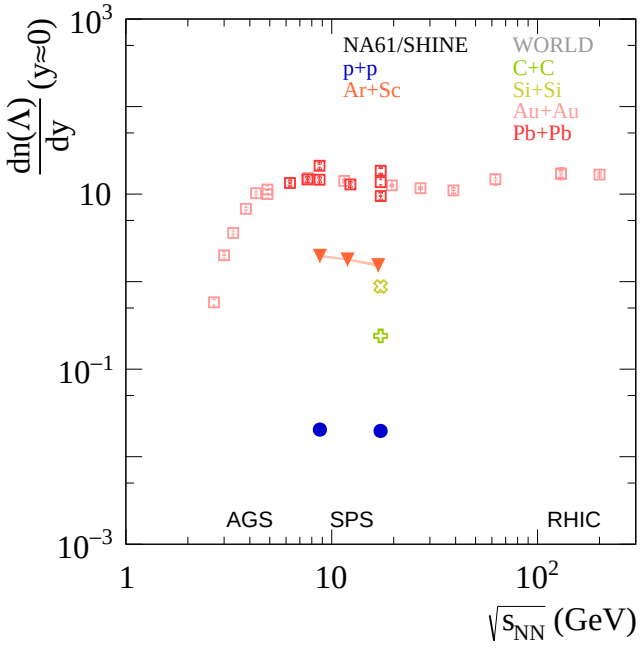

Figure 4.14: Energy dependence of mid-rapidity yield of Λ baryons. The systematic uncertainties of the Ar+Sc result are presented as a shaded band. Results for p+p ([100, 101]), Ar+Sc (this thesis), C+C ([116]), Si+Si ([116]), Au+Au ([120, 121, 123–129, 139]), and Pb+Pb ([42, 139–141]) are shown.

in Pb+Pb than in p+p collisions.

Additionally, the system size dependence of the $\langle\Lambda\rangle/\langle\pi\rangle$ ratio is presented in Fig. 4.18 for all analyzed beam momenta. The mean number of wounded nucleons $\langle W\rangle$ is used as the characteristic of system size. The prediction of the WNM [33] is added for reference to illustrate the expected constant behaviour relative to results for p+p collisions. Greater deviations from the WNM prediction are observed at lower beam momenta for heavier systems.

Fig. 4.19 shows the energy dependence of total strangeness-to-entropy ratio E_S, which is represented following the description in [40] as

$$E_S = \frac{\langle\Lambda\rangle + \langle K + \overline{K}\rangle}{\langle\pi\rangle} \,,$$

where $\langle\pi\rangle = 1.5 \cdot (\langle\pi^+\rangle + \langle\pi^-\rangle)$ as defined previously. Because the $\overline{\Lambda}/\Lambda$ ratio is typically less than 0.15 [140], the $\overline{\Lambda}$ contribution to E_S is small and therefore neglected. To include as much data as possible, $\langle K + \overline{K}\rangle$ is expressed as $4 \cdot \langle K^0_S\rangle$ for p+p data

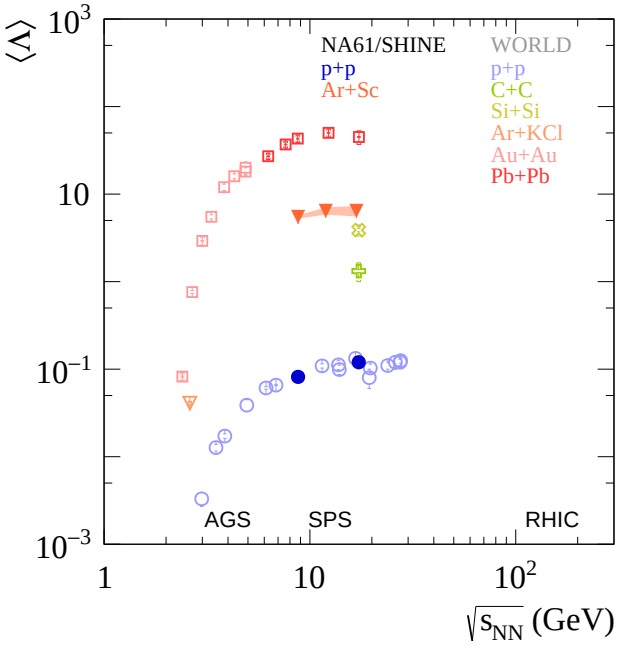

Figure 4.15: Energy dependence of the mean multiplicity of Λ baryons. The systematic uncertainties of the Ar+Sc result are presented as a shaded band. Results for p+p ([81–102]), Ar+Sc (this thesis), C+C ([116]), Si+Si ([116]), Ar+KCl ([117]), Au+Au ([120–124, 139]), and Pb+Pb ([140]) are shown.

(as K^0_S mesons were typically measured alongside Λ baryons in bubble chamber experiments), and as $2\cdot(\langle K^+\rangle+\langle K^-\rangle)$ for A+A data. For Pb+Pb collisions, E_S shows a distinct maximum at lower SPS energies, followed by a plateau. On the contrary, the results for p+p collisions exhibit no maximum, with E_S showing a rise followed by a plateau. The results for Ar+Sc collisions follow the trend observed in p+p collisions; however, the E_S values are much closer to those for Pb+Pb collisions.

Finally, the system size dependence of total strangeness-to-entropy ratio E_S is displayed in Fig. 4.20, employing the mean number of wounded nucleons $\langle W\rangle$ as the measure of system size. The Wounded Nucleon Model (WNM) [33] prediction is plotted to show the expected constant behaviour with respect to results for p+p collision. Similarly to the $\langle\Lambda\rangle/\langle\pi\rangle$ ratio, there are more significant deviations at lower beam momenta for heavier systems, but E_S values hint at a nearly linear dependence on the system size.

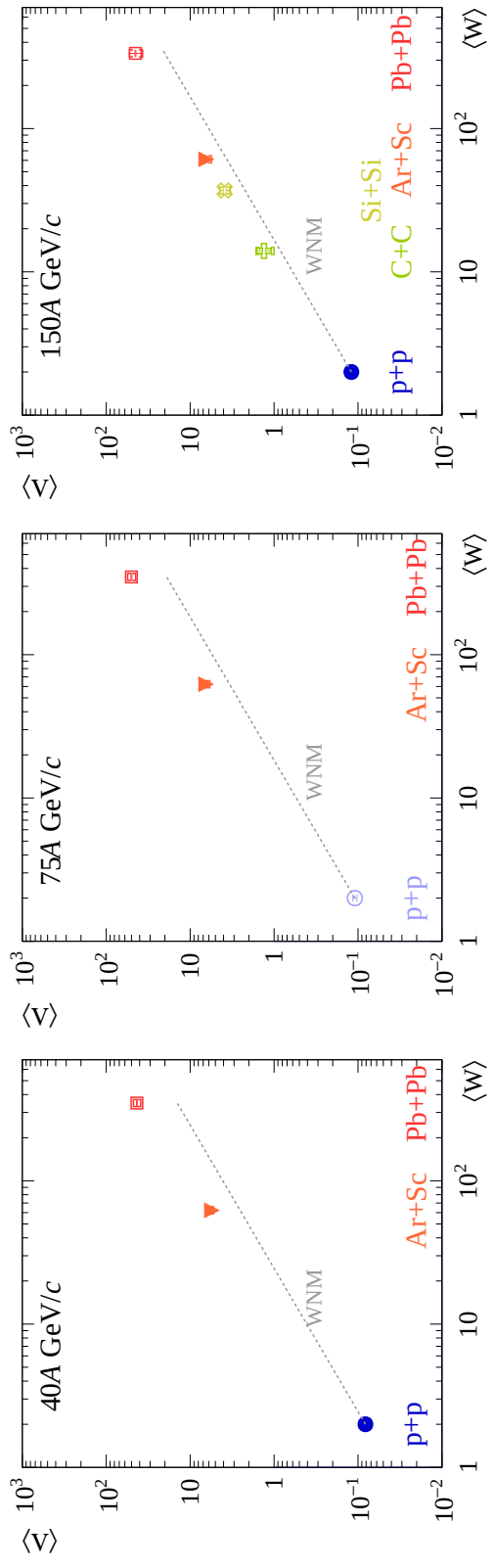

Figure 4.16: System size dependence of the mean multiplicity of Λ baryons produced at 40A (*left*), 75A (*middle*), and 150A GeV/c (*right*). The mean number of wounded nucleons $\langle W \rangle$ is utilized as a system size measure. The dotted line shows the Wounded Nucleon Model (WNM) [33] prediction for reference. Results for p+p ([89, 100, 101]), Ar+Sc (this thesis), C+C ([116]), Si+Si ([116]), and Pb+Pb ([140]) are shown.

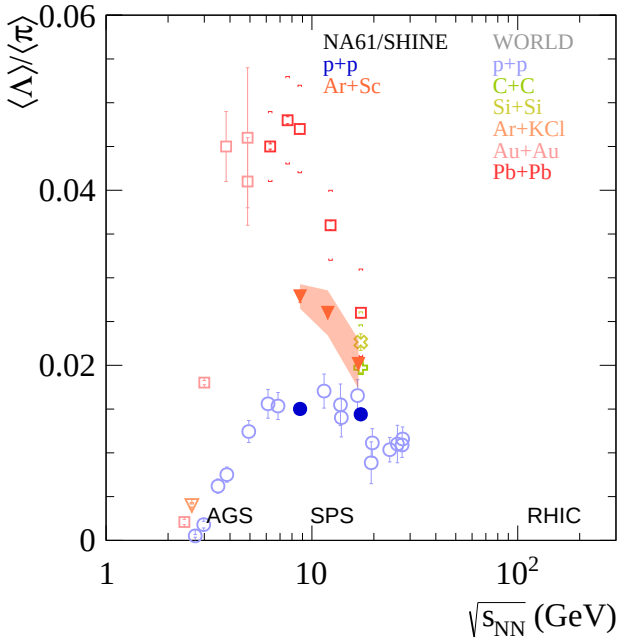

Figure 4.17: Energy dependence of the $\langle\Lambda\rangle/\langle\pi\rangle$ ratio. The systematic uncertainties of the Ar+Sc result are presented as a shaded band. Results for p+p (Λ: [81–102], $\pi^{\pm}$: [84, 105–114]), Ar+Sc (Λ: this thesis, $\pi^{\pm}$:[73]), C+C (Λ, $\pi^{\pm}$: [116]), Si+Si (Λ, $\pi^{\pm}$: [116]), Ar+KCl (Λ: [117], $\pi^{\pm}$: [119]), Au+Au(Λ: [120–124, 139], $\pi^{\pm}$: [131–134]), and Pb+Pb (Λ: [140], $\pi^{\pm}$: [43, 142]) are shown.

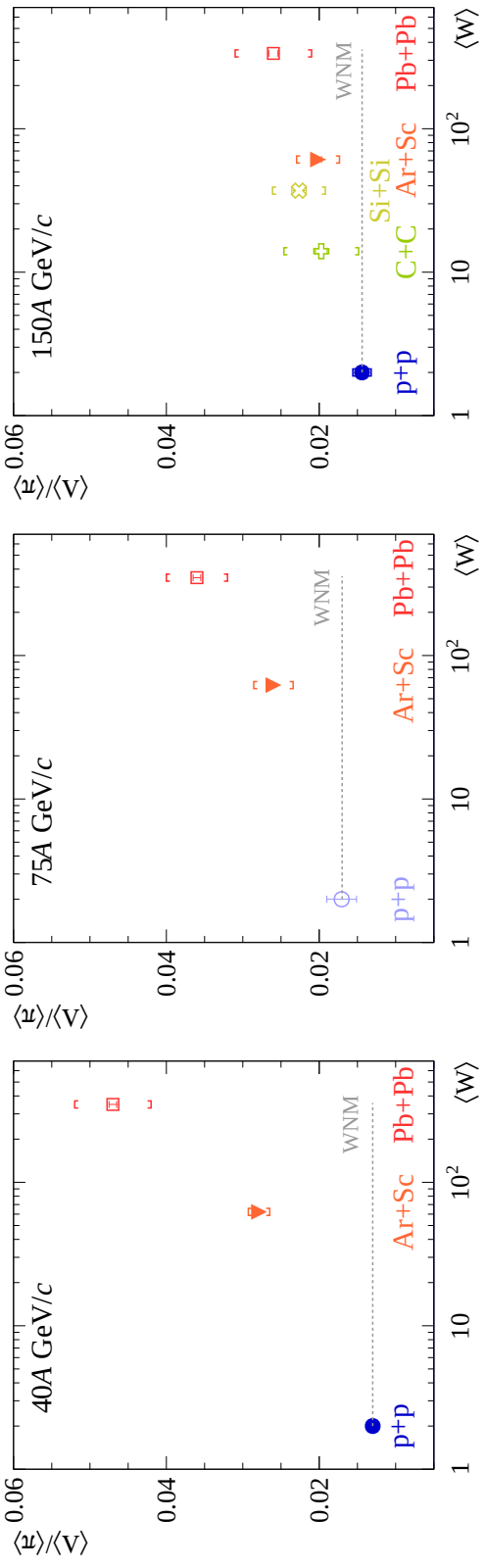

Figure 4.18: System size dependence of the $\langle\Lambda\rangle/\langle\pi\rangle$ ratio at 40A (*left*), 75A (*middle*), and 150A GeV/c (*right*). The mean number of wounded nucleons $\langle W\rangle$ is utilized as a system size measure. The dotted line shows the prediction of the Wounded Nucleon Model (WNM) [33] for reference. Results for p+p (Λ: [89, 100–102], $\pi^{\pm}$: [113, 114]), Ar+Sc (Λ: this thesis, $\pi^{\pm}$:[73]), C+C (Λ, $\pi^{\pm}$: [116]), Si+Si (Λ, $\pi^{\pm}$: [116]), and Pb+Pb (Λ: [140], $\pi^{\pm}$: [43, 142]) are shown.

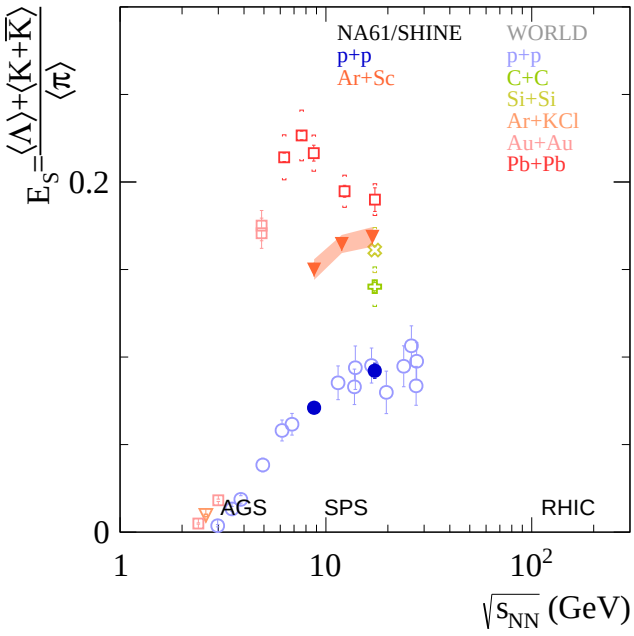

Figure 4.19: Energy dependence of total strangeness-to-entropy ratio E_S (see text for further details). The systematic uncertainties of the Ar+Sc result are presented as a shaded band. Results for p+p (Λ, K^0_s: [81–104], $\pi^{\pm}$: [84, 105–114]), Ar+Sc (Λ: this thesis, $K^{\pm}$, $\pi^{\pm}$:[73]), C+C (Λ, $K^{\pm}$, $\pi^{\pm}$: [116]), Si+Si (Λ, $K^{\pm}$, $\pi^{\pm}$: [116]), Ar+KCl (Λ: [117], $K^{\pm}$: [118], $\pi^{\pm}$: [119]), Au+Au (Λ: [120, 121, 123, 124, 139], K^0_s: [120, 121], $K^{\pm}$: [130] $\pi^{\pm}$: [131, 132, 134]), and Pb+Pb (Λ: [140], $K^{\pm}$, $\pi^{\pm}$: [43, 142]) are shown.

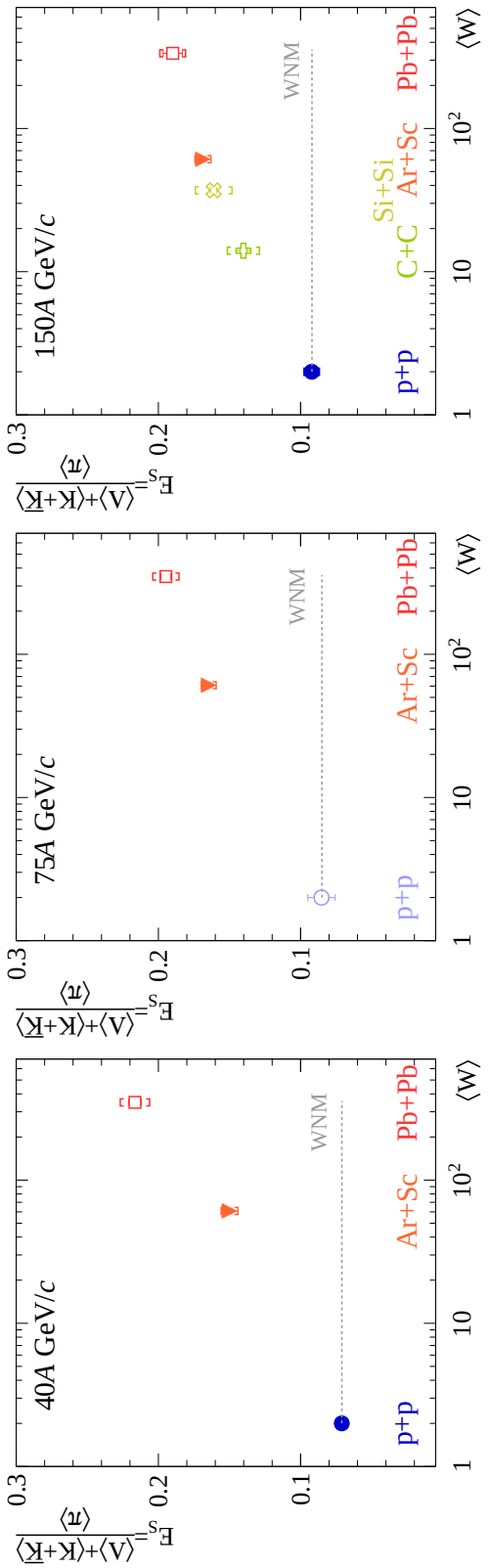

Figure 4.20: System size dependence of total strangeness-to-entropy ratio E_S (see text for further details) at 40A (*left*), 75A (*middle*), and 150A GeV/c (*right*). The mean number of wounded nucleons $\langle W \rangle$ is utilized as a system size measure. The dotted line shows the Wounded Nucleon Model (WNM) [33] prediction for reference. Results for p+p (Λ, K^0_s: [89, 100–104], $\pi^{\pm}$: [112, 114]), Ar+Sc (Λ: this thesis, $K^{\pm}$, $\pi^{\pm}$:[73]), C+C (Λ, $K^{\pm}$, $\pi^{\pm}$: [116]), Si+Si (Λ, $K^{\pm}$, $\pi^{\pm}$: [116]), and Pb+Pb (Λ: [140], $K^{\pm}$, $\pi^{\pm}$: [43, 142]) are shown.

Chapter 5

Summary and outlook

This thesis presents a study of Λ baryon production in 0-10% most central ^{40}Ar+^{45}Sc collisions at 40A, 75A, and 150A GeV/c ($\sqrt{s_{NN}}$ = 8.77, 11.94, and 17.3 GeV, respectively). The data was acquired by the NA61/SHINE experiment at CERN as part of a two-dimensional scan of the beam momentum and the system size, and analyzed as part of the main physics program of the experiment. It is the first measurement of Λ baryon production in a medium-size system such as Ar+Sc within the SPS energy range.

In this analysis, Λ baryons are identified by their weak decay channel $\Lambda \rightarrow p + \pi^-$. The reconstructed yields of Λ baryons are measured by fitting to the invariant mass of particle pairs considered as potential decay products. These results are corrected for various effects, such as losses due to the geometrical detector acceptance, reconstruction inefficiency, selections applied in the analysis, branching ratio and feed-down from the decays of heavier hyperons, using detailed Monte Carlo simulation. The main outcomes of this thesis are the double-differential spectra of Λ baryons in the rapidity-transverse momentum phase space, rapidity spectra and mean multiplicities of Λ baryons.

The obtained experimental results are compared to selected particle production models. The Epos1.99 model generally underestimates Λ baryon production properties in the mid-rapidity region, although it provides an almost accurate prediction of the multiplicity at mid-rapidity and mean multiplicity values for 150A GeV/c beam momentum. The Smash model predicts significantly lower values for the inverse slope parameter and yield of Λ baryons in the full rapidity range for all analyzed beam

momenta.

The energy and system-size dependencies of the Λ baryon production properties are explored across different collision systems. Overall, the system size dependencies of the studied variables usually exhibit linear dependence, yet the simple scaling of the results from p+p collisions underestimates the corresponding values for heavier systems. Both the values of the inverse slope parameter and multiplicities of Λ baryons for Ar+Sc collisions are much closer to those observed in heavier systems, such as Pb+Pb and Au+Au, rather than lighter p+p and C+C. Nevertheless, even though the values of the $\langle\Lambda\rangle/\langle\pi\rangle$ ratio for Ar+Sc collisions follow the trend of the results for Pb+Pb and Au+Au collisions, no maximum is observed in the total strangeness-to-entropy ratio for Ar+Sc collisions.

The analysis of Λ baryon production in Ar+Sc collisions at the lower beam momenta (13A-30A GeV/c) is crucial to confirm the existence of a maximum in the $\langle\Lambda\rangle/\langle\pi\rangle$ ratio. Moreover, the measurement of multi-strange (anti-)baryons in Ar+Sc collisions would deepen the understanding of the strangeness enhancement in medium-size systems. To further fill the knowledge gap between the results from p+p and Ar+Sc collisions and from Ar+Sc and Pb+Pb collisions, additional studies of Λ baryon production can be conducted. The existing NA61/SHINE experiment datasets from Be+Be and Xe+La collisions would be the first step in this direction. Moreover, the requests for B, O and Mg beams in Runs 3 and 4 [145, 146] have been submitted to extend the NA61/SHINE two-dimensional scan in beam momentum and system size. Together with the future results from HADES/CBM, STAR, PHENIX, LHCb FXT, and upcoming experiments [147, 148], an even more scrutinized study of the properties of strongly interacting matter will be possible.

Bibliography

[1] Laurie M. Brown et al. "The Rise of the Standard Model: 1964–1979". In: *The Rise of the Standard Model: A History of Particle Physics from 1964 to 1979*. Ed. by Lillian Hoddeson et al. Cambridge University Press, 1997, pp. 3–35.

[2] ATLAS collaboration, Georges Aad et al. "Observation of a new particle in the search for the Standard Model Higgs boson with the ATLAS detector at the LHC". In: *Phys. Lett. B* 716 (2012), pp. 1–29. DOI: 10.1016/j.physletb.2012.08.020. arXiv: 1207.7214 [hep-ex].

[3] CMS collaboration, Serguei Chatrchyan et al. "Observation of a New Boson at a Mass of 125 GeV with the CMS Experiment at the LHC". In: *Phys. Lett. B* 716 (2012), pp. 30–61. DOI: 10.1016/j.physletb.2012.08.021. arXiv: 1207.7235 [hep-ex].

[4] *Wikipedia, The Free Encyclopedia*. [Online; accessed 6-August-2024]. 2024. URL: https://en.wikipedia.org/.

[5] Albert Einstein. "Die Feldgleichungen der Gravitation". In: *Sitzungsberichte der Königlich Preussischen Akademie der Wissenschaften* (Jan. 1915), pp. 844–847.

[6] Particle Data Group collaboration, R. L. Workman et al. "Review of Particle Physics". In: *PTEP* 2022 (2022), p. 083C01. DOI: 10.1093/ptep/ptac097.

[7] Sheldon L. Glashow. "The renormalizability of vector meson interactions". In: *Nuclear Physics* 10 (1959), pp. 107–117. ISSN: 0029-5582. DOI: https://doi.org/10.1016/0029-5582(59)90196-8. URL: https://www.sciencedirect.com/science/article/pii/0029558259901968.

[8] Abdus Salam and John Clive Ward. "Weak and electromagnetic interactions". In: *Nuovo Cim.* 11 (1959), pp. 568–577. DOI: 10.1007/BF02726525.

[9] Steven Weinberg. "A Model of Leptons". In: *Phys. Rev. Lett.* 19 (21 Nov. 1967), pp. 1264–1266. DOI: 10.1103/PhysRevLett.19.1264. URL: https://link.aps.org/doi/10.1103/PhysRevLett.19.1264.

[10] F. Englert and R. Brout. "Broken Symmetry and the Mass of Gauge Vector Mesons". In: *Phys. Rev. Lett.* 13 (9 Aug. 1964), pp. 321–323. DOI: 10.1103/PhysRevLett.13.321. URL: https://link.aps.org/doi/10.1103/PhysRevLett.13.321.

[11] Peter W. Higgs. "Broken Symmetries and the Masses of Gauge Bosons". In: *Phys. Rev. Lett.* 13 (16 Oct. 1964), pp. 508–509. DOI: 10.1103/PhysRevLett.13.508. URL: https://link.aps.org/doi/10.1103/PhysRevLett.13.508.

[12] G. S. Guralnik, C. R. Hagen, and T. W. B. Kibble. "Global Conservation Laws and Massless Particles". In: *Phys. Rev. Lett.* 13 (20 Nov. 1964), pp. 585–587. DOI: 10.1103/PhysRevLett.13.585. URL: https://link.aps.org/doi/10.1103/PhysRevLett.13.585.

[13] Nicola Cabibbo. "Unitary Symmetry and Leptonic Decays". In: *Phys. Rev. Lett.* 10 (1963). [648(1963)], pp. 531–533. DOI: 10.1103/PhysRevLett.10.531.

[14] Makoto Kobayashi and Toshihide Maskawa. "CP Violation in the Renormalizable Theory of Weak Interaction". In: *Prog. Theor. Phys.* 49 (1973), pp. 652–657. DOI: 10.1143/PTP.49.652.

[15] LHCb collaboration, Roel Aaij et al. "Observation of the resonant character of the $Z(4430)^-$ state". In: *Phys. Rev. Lett.* 112.22 (2014), p. 222002. DOI: 10.1103/PhysRevLett.112.222002. arXiv: 1404.1903 [hep-ex].

[16] BESIII collaboration, M. Ablikim et al. "Observation of $Z_c(3900)^0$ in $e^+e^- \to \pi^0\pi^0 J/\psi$". In: *Phys. Rev. Lett.* 115.11 (2015), p. 112003. DOI: 10.1103/PhysRevLett.115.112003. arXiv: 1506.06018 [hep-ex].

[17] LHCb collaboration, Roel Aaij et al. "Observation of $J/\psi p$ Resonances Consistent with Pentaquark States in $\Lambda_b^0 \to J/\psi K^- p$ Decays". In: *Phys. Rev. Lett.* 115 (2015), p. 072001. DOI: 10.1103/PhysRevLett.115.072001. arXiv: 1507.03414 [hep-ex].

[18] LHCb collaboration, Roel Aaij et al. "Observation of a narrow pentaquark state, $P_c(4312)^+$, and of two-peak structure of the $P_c(4450)^+$". In: *Phys. Rev. Lett.* 122.22 (2019), p. 222001. DOI: 10.1103/PhysRevLett.122.222001. arXiv: 1904.03947 [hep-ex].

[19] John C. Collins and M. J. Perry. "Superdense Matter: Neutrons Or Asymptotically Free Quarks?" In: *Phys. Rev. Lett.* 34 (1975), p. 1353. DOI: 10.1103/PhysRevLett.34.1353.

[20] N. Cabibbo and G. Parisi. "Exponential Hadronic Spectrum and Quark Liberation". In: *Phys. Lett. B* 59 (1975), pp. 67–69. DOI: 10.1016/0370-2693(75)90158-6.

[21] Ulrich W. Heinz and Maurice Jacob. "Evidence for a new state of matter: An Assessment of the results from the CERN lead beam program". Jan. 2000. arXiv: nucl-th/0002042.

[22] Ulrich W. Heinz. "The Little bang: Searching for quark gluon matter in relativistic heavy ion collisions". In: *Nucl. Phys. A* 685 (2001). Ed. by W. Norenberg, D. Guerreau, and V. Metag, pp. 414–431. DOI: 10.1016/S0375-9474(01)00558-9. arXiv: hep-ph/0009170.

[23] STAR collaboration, John Adams et al. "Experimental and theoretical challenges in the search for the quark gluon plasma: The STAR Collaboration's critical assessment of the evidence from RHIC collisions". In: *Nucl. Phys. A* 757 (2005), pp. 102–183. DOI: 10.1016/j.nuclphysa.2005.03.085. arXiv: nucl-ex/0501009.

[24] BRAHMS collaboration, I. Arsene et al. "Quark gluon plasma and color glass condensate at RHIC? The Perspective from the BRAHMS experiment". In: *Nucl. Phys. A* 757 (2005), pp. 1–27. DOI: 10.1016/j.nuclphysa.2005.02.130. arXiv: nucl-ex/0410020.

[25] PHENIX collaboration, K. Adcox et al. "Formation of dense partonic matter in relativistic nucleus-nucleus collisions at RHIC: Experimental evaluation by the PHENIX collaboration". In: *Nucl. Phys. A* 757 (2005), pp. 184–283. DOI: 10.1016/j.nuclphysa.2005.03.086. arXiv: nucl-ex/0410003.

[26] PHOBOS collaboration, B. B. Back et al. "The PHOBOS perspective on discoveries at RHIC". In: *Nucl. Phys. A* 757 (2005), pp. 28–101. DOI: 10.1016/j.nuclphysa.2005.03.084. arXiv: nucl-ex/0410022.

[27] Johann Rafelski. "Connecting QGP-Heavy Ion Physics to the Early Universe". In: *Nucl. Phys. B Proc. Suppl.* 243-244 (2013). Ed. by Roberto Battiston and Sergio Bertolucci, pp. 155–162. DOI: 10.1016/j.nuclphysbps.2013.09.017. arXiv: 1306.2471 [astro-ph.CO].

[28] Heng-Tong Ding, Frithjof Karsch, and Swagato Mukherjee. "Thermodynamics of strong-interaction matter from Lattice QCD". In: *Int. J. Mod. Phys. E* 24.10 (2015), p. 1530007. DOI: 10.1142/S0218301315300076. arXiv: 1504.05274 [hep-lat].

[29] Y. Aoki et al. "The Order of the quantum chromodynamics transition predicted by the standard model of particle physics". In: *Nature* 443 (2006), pp. 675–678. DOI: 10.1038/nature05120. arXiv: hep-lat/0611014.

[30] Jana N. Guenther. "Overview of the QCD phase diagram: Recent progress from the lattice". In: *Eur. Phys. J. A* 57.4 (2021), p. 136. DOI: 10.1140/epja/s10050-021-00354-6. arXiv: 2010.15503 [hep-lat].

[31] *MADAI: Models and Data Analysis Initiative*. [Online; accessed 2-September-2024]. 2024. URL: https://madai.phy.duke.edu/index-2.html.

[32] Peter Braun-Munzinger and Benjamin Dönigus. "Loosely-bound objects produced in nuclear collisions at the LHC". In: *Nucl. Phys. A* 987 (2019), pp. 144–201. DOI: 10.1016/j.nuclphysa.2019.02.006. arXiv: 1809.04681 [nucl-ex].

[33] A. Bialas, M. Bleszynski, and W. Czyz. "Multiplicity Distributions in Nucleus-Nucleus Collisions at High-Energies". In: *Nucl. Phys. B* 111 (1976), pp. 461–476. DOI: 10.1016/0550-3213(76)90329-1.

[34] LHCb collaboration, Roel Aaij et al. "Centrality determination in heavy-ion collisions with the LHCb detector". In: *JINST* 17.05 (2022), P05009. DOI: 10.1088/1748-0221/17/05/P05009. arXiv: 2111.01607 [nucl-ex].

[35] Johann Rafelski and Berndt Muller. "Strangeness Production in the Quark - Gluon Plasma". In: *Phys. Rev. Lett.* 48 (1982). [Erratum: Phys.Rev.Lett. 56, 2334 (1986)], p. 1066. DOI: 10.1103/PhysRevLett.48.1066.

[36] P. Koch, Johann Rafelski, and W. Greiner. "Strange hadron in hot nuclear matter". In: *Phys. Lett. B* 123 (1983), pp. 151–154. DOI: 10.1016/0370-2693(83)90411-2.

[37] P. Koch, Berndt Muller, and Johann Rafelski. "Strangeness in Relativistic Heavy Ion Collisions". In: *Phys. Rept.* 142 (1986), pp. 167–262. DOI: 10.1016/0370-1573(86)90096-7.

[38] E802 collaboration, T. Abbott et al. "Comparison of p + A and Si + Au collisions at 14.6 GeV/c". In: *Phys. Rev. Lett.* 66 (1991), pp. 1567–1570. DOI: 10.1103/PhysRevLett.66.1567.

[39] NA35 collaboration, J. Bartke et al. "Neutral strange particle production in sulphur sulphur and proton sulphur collisions at 200 GeV/nucleon". In: *Z. Phys. C* 48 (1990), pp. 191–200. DOI: 10.1007/BF01554465.

[40] NA35 collaboration, T. Alber et al. "Strange particle production in nuclear collisions at 200 GeV per nucleon". In: *Z. Phys. C* 64 (1994), pp. 195–207. DOI: 10.1007/BF01557391.

[41] WA85 collaboration, F. Antinori et al. "Enhancement of strange and multi-strange baryons and anti-baryons in S W interactions at 200 GeV/c". In: *Phys. Lett. B* 447 (1999), pp. 178–182. DOI: 10.1016/S0370-2693(98)01561-5.

[42] NA57 collaboration, F. Antinori et al. "Enhancement of hyperon production at central rapidity in 158 A GeV/c Pb-Pb collisions". In: *J. Phys. G* 32 (2006), pp. 427–442. DOI: 10.1088/0954-3899/32/4/003. arXiv: nucl-ex/0601021.

[43] NA49 collaboration, C. Alt et al. "Pion and kaon production in central Pb + Pb collisions at 20 A and 30 A GeV: Evidence for the onset of deconfinement". In: *Phys. Rev. C* 77 (2008), p. 024903. DOI: 10.1103/PhysRevC.77.024903. arXiv: 0710.0118 [nucl-ex].

[44] Marek Gazdzicki and Mark I. Gorenstein. "On the early stage of nucleus-nucleus collisions". In: *Acta Phys. Polon. B* 30 (1999), p. 2705. arXiv: hep-ph/9803462.

[45] ALICE collaboration, Jaroslav Adam et al. "Enhanced production of multi-strange hadrons in high-multiplicity proton-proton collisions". In: *Nature Phys.* 13 (2017), pp. 535–539. DOI: 10.1038/nphys4111. arXiv: 1606.07424 [nucl-ex].

[46] Peter Koch, Berndt Müller, and Johann Rafelski. "From Strangeness Enhancement to Quark-Gluon Plasma Discovery". In: *Int. J. Mod. Phys. A* 32.31 (2017), p. 1730024. DOI: 10.1142/S0217751X17300241. arXiv: 1708.08115 [nucl-th].

[47] F. Becattini, J. Manninen, and M. Gazdzicki. "Energy and system size dependence of chemical freeze-out in relativistic nuclear collisions". In: *Phys. Rev. C* 73 (2006), p. 044905. DOI: 10.1103/PhysRevC.73.044905. arXiv: hep-ph/0511092.

[48] T2K collaboration, K. Abe et al. "The T2K Experiment". In: *Nucl. Instrum. Meth. A* 659 (2011), pp. 106–135. DOI: 10.1016/j.nima.2011.06.067. arXiv: 1106.1238 [physics.ins-det].

[49] MINERvA collaboration, L. Aliaga et al. "Design, Calibration, and Performance of the MINERvA Detector". In: *Nucl. Instrum. Meth. A* 743 (2014), pp. 130–159. DOI: 10.1016/j.nima.2013.12.053. arXiv: 1305.5199 [physics.ins-det].

[50] NOvA collaboration, D. S. Ayres et al. *The NOvA Technical Design Report*. Tech. rep. Oct. 2007. DOI: 10.2172/935497.

[51] DUNE collaboration, R. Acciarri et al. *Long-Baseline Neutrino Facility (LBNF) and Deep Underground Neutrino Experiment (DUNE): Conceptual Design Report, Volume 2: The Physics Program for DUNE at LBNF*. Tech. rep. Dec. 2015. arXiv: 1512.06148 [physics.ins-det].

[52] G. Navarra et al. "KASCADE-Grande: A large acceptance, high-resolution cosmic-ray detector up to 10**18-eV". In: *Nucl. Instrum. Meth. A* 518 (2004). Ed. by G. Batignani et al., pp. 207–209. DOI: 10.1016/j.nima.2003.10.061.

[53] IceCube collaboration, R. Abbasi et al. "IceTop: The surface component of IceCube". In: *Nucl. Instrum. Meth. A* 700 (2013), pp. 188–220. DOI: 10.1016/j.nima.2012.10.067. arXiv: 1207.6326 [astro-ph.IM].

[54] Telescope Array collaboration, T. Abu-Zayyad et al. "The surface detector array of the Telescope Array experiment". In: *Nucl. Instrum. Meth. A* 689 (2013), pp. 87–97. DOI: 10.1016/j.nima.2012.05.079. arXiv: 1201.4964 [astro-ph.IM].

[55] Pierre Auger collaboration, J. Abraham et al. "Properties and performance of the prototype instrument for the Pierre Auger Observatory". In: *Nucl. Instrum. Meth. A* 523 (2004), pp. 50–95. DOI: 10.1016/j.nima.2003.12.012.

[56] Yoann Genolini et al. "Current status and desired precision of the isotopic production cross sections relevant to astrophysics of cosmic rays: Li, Be, B, C, and N". In: *Phys. Rev. C* 98.3 (2018), p. 034611. DOI: 10.1103/PhysRevC.98.034611. arXiv: 1803.04686 [astro-ph.HE].

[57] Yoann Génolini et al. "Current status and desired precision of the isotopic production cross sections relevant to astrophysics of cosmic rays. II. Fluorine to silicon and updated results for Li, Be, and B". In: *Phys. Rev. C* 109.6 (2024), p. 064914. DOI: 10.1103/PhysRevC.109.064914. arXiv: 2307.06798 [astro-ph.HE].

[58] NA61 collaboration, N. Abgrall et al. "NA61/SHINE facility at the CERN SPS: beams and detector system". In: *JINST* 9 (2014), P06005. DOI: 10.1088/1748-0221/9/06/P06005. arXiv: 1401.4699 [physics.ins-det].

[59] Ewa Lopienska. "The CERN accelerator complex, layout in 2022. Complexe des accélérateurs du CERN en janvier 2022". In: (2022). General Photo. URL: https://cds.cern.ch/record/2800984.

[60] D Manglunki and S Maury. "Preparation of Light Ions for LHC and SPS Physics (S-LightIon Project)". In: (2011). URL: http://cds.cern.ch/record/1367429.

[61] NA61/SHINE collaboration, M Gazdzicki. *Status of the evidence for the onset of deconfinement and the urgent need for primary Ar beams*. Tech. rep. Geneva: CERN, 2011. URL: https://cds.cern.ch/record/1377835.

[62] D. Küchler et al. "Preparation of a primary argon beam for the CERN fixed target physics". In: *Review of Scientific Instruments* 85.2 (Jan. 2014), 02A954. ISSN: 0034-6748. DOI: 10.1063/1.4854275.

[63] D. Banas et al. "Influence of target material impurities on physical results in relativistic heavy-ion collisions". In: *Eur. Phys. J. Plus* 134.1 (2019), p. 44. DOI: 10.1140/epjp/i2019-12465-9. arXiv: 1808.10377 [nucl-ex].

[64] Piotr Podlaski. "Study of charged hadron production with tof-dE/dx identification method in central Ar+Sc collisions in NA61/SHINE experiment at CERN". PhD thesis. 2021. URL: https://cds.cern.ch/record/2799198.

[65] Klaus Werner, Fu-Ming Liu, and Tanguy Pierog. "Parton ladder splitting and the rapidity dependence of transverse momentum spectra in deuteron-gold collisions at RHIC". In: *Phys. Rev.* C74 (2006), p. 044902. DOI: 10.1103/PhysRevC.74.044902. arXiv: hep-ph/0506232 [hep-ph].

[66] T. Pierog and K. Werner. "EPOS Model and Ultra High Energy Cosmic Rays". In: *Nucl.Phys.Proc.Suppl.* 196 (2009), pp. 102–105. DOI: 10.1016/j.nuclphysbps.2009.09.017. arXiv: 0905.1198 [hep-ph].

[67] Antoni Aduszkiewicz. "Energy dependence of negatively charged pion production in proton-proton interactions at the CERN SPS". PhD thesis. 2016. URL: https://cds.cern.ch/record/2135329.

[68] GEANT4 collaboration, S. Agostinelli et al. "GEANT4–a simulation toolkit". In: *Nucl. Instrum. Meth. A* 506 (2003), pp. 250–303. DOI: 10.1016/S0168-9002(03)01368-8.

[69] J. Allison et al. "Recent developments in Geant4". In: *Nucl. Instrum. Meth. A* 835 (2016), pp. 186–225. DOI: 10.1016/j.nima.2016.06.125.

[70] NA61/SHINE collaboration, A. Acharya et al. "Spectra and mean multiplicities of π^- in central ^{40}Ar+^{45}Sc collisions at 13A, 19A, 30A, 40A, 75A and 150A GeV/c beam momenta measured by the NA61/SHINE spectrometer at the CERN SPS". In: *Eur. Phys. J. C* 81.5 (2021), p. 397. DOI: 10.1140/epjc/s10052-021-09135-3. arXiv: 2101.08494 [hep-ex].

[71] NA61/SHINE collaboration, A. Acharya et al. "Measurements of π^- production in ^{7}Be+^{9}Be collisions at beam momenta from 19A to 150A GeV/c in the NA61/SHINE experiment at the CERN SPS". In: *Eur. Phys. J. C* 80.10 (2020). [Erratum: Eur.Phys.J.C 81, 144 (2021)], p. 961. DOI: 10.1140/epjc/s10052-020-08514-6. arXiv: 2008.06277 [nucl-ex].

[72] Emil Aleksander Kaptur. "Analysis of collision centrality and negative pion spectra in ^{7}Be + ^{9}Be interactions at CERN SPS energy range". PhD thesis. 2018. URL: https://edms.cern.ch/document/2004086/1.

[73] NA61/SHINE collaboration, H. Adhikary et al. "Measurements of $\pi^{\pm}$, $K^{\pm}$, p and $\bar{p}$ spectra in ^{40}Ar+^{45}Sc collisions at 13A to 150A GeV/c". In: *Eur. Phys. J. C* 84.4 (2024), p. 416. DOI: 10.1140/epjc/s10052-024-12602-2. arXiv: 2308.16683 [nucl-ex].

[74] Wouter Verkerke and David Kirkby. *The RooFit toolkit for data modeling*. 2003. arXiv: physics/0306116 [physics.data-an].

[75] J. Podolanski and R. Armenteros. "III. Analysis of V-events". In: *The London, Edinburgh, and Dublin Philosophical Magazine and Journal of Science* 45.360 (1954), pp. 13–30. DOI: 10.1080/14786440108520416. URL: https://doi.org/10.1080/14786440108520416.

[76] Marek Gazdzicki, Mark Gorenstein, and Peter Seyboth. "Onset of deconfinement in nucleus-nucleus collisions: Review for pedestrians and experts". In: *Acta Phys. Polon. B* 42 (2011), pp. 307–351. DOI: 10.5506/APhysPolB.42.307. arXiv: 1006.1765 [hep-ph].

[77] Rene Brun and Fons Rademakers. "ROOT — An object oriented data analysis framework". In: *Nuclear Instruments and Methods in Physics Research Section A: Accelerators, Spectrometers, Detectors and Associated Equipment* 389.1 (1997). New Computing Techniques in Physics Research V, pp. 81–86. ISSN: 0168-9002. DOI: https://doi.org/10.1016/S0168-9002(97)00048-X.

[78] J Mohs, S Ryu, and H Elfner. "Particle production via strings and baryon stopping within a hadronic transport approach". In: *Journal of Physics G: Nuclear and Particle Physics* 47.6 (Apr. 2020), p. 065101. DOI: 10.1088/1361-6471/ab7bd1. URL: https://dx.doi.org/10.1088/1361-6471/ab7bd1.

[79] J. Weil et al. "Particle production and equilibrium properties within a new hadron transport approach for heavy-ion collisions". In: *Phys. Rev. C* 94 (5 Nov. 2016), p. 054905. DOI: 10.1103/PhysRevC.94.054905.

[80] Wojciech Bryliński. "Study of K^0_S Meson Production in Central Ar+Sc Collisions at SPS Energies". PhD thesis. 2023. URL: https://www.bip.pw.edu.pl/content/download/63045/584531/file/doktorat-Brylinski_B5_PDF.pdf.

[81] W. J. Fickinger et al. "p-p Interactions at 2 Bev. 1. Single-Pion Production". In: *Phys. Rev.* 125 (1962), pp. 2082–2090. DOI: 10.1103/PhysRev.125.2082.

[82] R. I. Louttit et al. "Production of Strange Particles in p-p Collisions at 2.85 Bev". In: *Phys. Rev.* 123 (1961), pp. 1465–1471. DOI: 10.1103/PhysRev.123.1465.

[83] E. Bierman, A. P. Colleraine, and U. Nauenberg. "Search for Dibaryon Resonant States". In: *Phys. Rev.* 147 (1966), pp. 922–931. DOI: 10.1103/PhysRev.147.922.

[84] G. Alexander et al. "Proton-Proton Interactions at 5.5 GeV/c". In: *Phys. Rev.* 154 (1967), pp. 1284–1304. DOI: 10.1103/PhysRev.154.1284.

[85] R. L. Eisner et al. "Λ and $K^0 0$ Production in Polarized p p Interactions at 6 GeV/c". In: *Nucl. Phys. B* 123 (1977), pp. 361–381. DOI: 10.1016/0550-3213(77)90173-0.

[86] M. Firebaugh et al. "Strange-particle production in 8-BeV/c proton-proton interactions". In: *Phys. Rev.* 172 (1968), pp. 1354–1369. DOI: 10.1103/PhysRev.172.1354.

[87] K. Jaeger et al. "Inclusive γ, π^0, K^0 and Λ Production in 12.4 GeV/c p p Interactions". In: *Phys. Rev. D* 11 (1975), p. 1756. DOI: 10.1103/PhysRevD.11.1756.

[88] Scandinavian Bubble Chamber collaboration, P. Aahlin et al. "Single-Particle Properties of $Lambda$ and K^0_S from 19 GeV/c Proton Proton Interactions". In: *Phys. Scripta* 21 (1980), pp. 12–16. DOI: 10.1088/0031-8949/21/1/002.

[89] V. V. Ammosov et al. "Neutral Strange Particle Production in p p Interactions at 69 GeV/c". In: *Nucl. Phys. B* 115 (1976), pp. 269–286. DOI: 10.1016/0550-3213(76)90257-1.

[90] Margaret Alston-Garnjost et al. "Neutral Particle Production in $\pi^+ p$ and pp Collisions at 100 GeV/c". In: *Phys. Rev. Lett.* 35 (1975), p. 142. DOI: 10.1103/PhysRevLett.35.142.

[91] J. W. Chapman et al. "Production of γ, Λ^0, K_S^0 and $\bar{\Lambda}^0$ in pp Collisions at 102 GeV/c." In: *Phys. Lett. B* 47 (1973), pp. 465–468. DOI: 10.1016/0370-2693(73)90116-0.

[92] Bonn-Hamburg-Munich collaboration, V. Blobel et al. "Multiplicities, topological cross-sections, and single particle inclusive distributions from p p interactions at 12 GeV/c and 24 GeV/c". In: *Nucl. Phys. B* 69 (1974), pp. 454–492. DOI: 10.1016/0550-3213(74)90449-0.

[93] D. Brick et al. "INCLUSIVE PRODUCTION OF NEUTRAL STRANGE PARTICLES BY 147 GeV/c $\pi^+/K^+/p$ INTERACTIONS IN HYDROGEN". In: *Nucl. Phys. B* 164 (1980), p. 1. DOI: 10.1016/0550-3213(80)90499-X.

[94] NA5 collaboration, J. Allday et al. "Annihilation and Topological Cross-sections for PP and $\bar{P}P$ Interactions at 200 GeV/c". In: *Z. Phys. C* 40 (1988), pp. 29–39. DOI: 10.1007/BF01559715.

[95] K. Jaeger et al. "Characteristics of V^0 and γ Production in pp Interactions at 205 GeV/c". In: *Phys. Rev. D* 11 (1975), p. 2405. DOI: 10.1103/PhysRevD.11.2405.

[96] F. Lopinto et al. "INCLUSIVE K^0, Λ^0, $K^{*\pm}(890)$, AND $\Sigma^{*\pm}(1385)$ PRODUCTION IN P P COLLISIONS AT 300 GEV/C". In: *Phys. Rev. D* 22 (1980), pp. 573–581. DOI: 10.1103/PhysRevD.22.573.

[97] EHS-RCBC, Bombay-CERN-Genoa-Innsbruck-Japan-Madrid-Mons-Rutgers-Serpukhov-Tennessee-Vienna collaboration, M. Asai et al. "Inclusive K_S^0, Λ and $\bar{\Lambda}$ Production in 360-GeV/cpp Interactions Using the European Hybrid Spectrometer". In: *Z. Phys. C* 27 (1985), p. 11. DOI: 10.1007/BF01642475.

[98] R. D. Kass et al. "CHARGED AND NEUTRAL PARTICLE PRODUCTION FROM 400 GEV/C P P COLLISIONS". In: *Phys. Rev. D* 20 (1979), pp. 605–614. DOI: 10.1103/PhysRevD.20.605.

[99] H. Kichimi et al. "Inclusive Study of Strange Particle Production in p p Interactions at 405 GeV/c". In: *Phys. Rev. D* 20 (1979), p. 37. DOI: 10.1103/PhysRevD.20.37.

[100] NA61/SHINE collaboration, A. Aduszkiewicz et al. "Production of Λ -hyperons in inelastic p+p interactions at 158 GeV/c". In: *Eur. Phys. J.* C76.4 (2016), p. 198. DOI: 10.1140/epjc/s10052-016-4003-2. arXiv: 1510.03720 [hep-ex].

[101] T. Susa. "Preliminary results on Lambda production in p+p @ 40 GeV/c". URL: https://twiki.cern.ch/twiki/bin/viewauth/NA61/Lambda_pp40.

[102] Marek Gazdzicki and Dieter Rohrich. "Strangeness in nuclear collisions". In: *Z. Phys. C* 71 (1996), pp. 55–64. DOI: 10.1007/s002880050147. arXiv: hep-ex/9607004.

[103] NA61/SHINE collaboration, N. Abgrall et al. "K^0_S meson production in inelastic p+p interactions at 31, 40 and 80 GeV/c beam momentum measured by NA61/SHINE at the CERN SPS". In: (Feb. 2024). arXiv: 2402.17025 [hep-ex].

[104] NA61/SHINE collaboration, A. Acharya et al. "K^0_S meson production in inelastic p+p interactions at 158 GeV/c beam momentum measured by NA61/SHINE at the CERN SPS". In: *Eur. Phys. J. C* 82.1 (2022), p. 96. DOI: 10.1140/epjc/s10052-021-09976-y. arXiv: 2106.07535 [hep-ex].

[105] H. Bøggild et al. "Some features of particle multiplicities and momentum spectra in inelastic proton-proton collisions at 19 GeV/c". In: *Nuclear Physics B* 27.2 (1971), pp. 285–313. ISSN: 0550-3213. DOI: https://doi.org/10.1016/0550-3213(71)90096-4. URL: https://www.sciencedirect.com/science/article/pii/0550321371900964.

[106] J. Erwin et al. "Multiplicities in 100 GeV/c π^+p and pp Interactions Using a Tagged Beam." In: *Phys. Rev. Lett.* 32 (1974), pp. 254–257. DOI: 10.1103/PhysRevLett.32.254.

[107] C. Bromberg et al. "Cross-Sections and Charged Particle Multiplicities at 102 GeV/c and 405 GeV/c." In: *Phys. Rev. Lett.* 31 (1973), pp. 1563–1566. DOI: 10.1103/PhysRevLett.31.1563.

[108] D. Brick et al. "Topological, total, and elastic cross sections for K^+p, π^+p, and pp interactions at 147 GeV/c". In: *Phys. Rev. D* 25 (11 June 1982), pp. 2794–2806. DOI: 10.1103/PhysRevD.25.2794. URL: https://link.aps.org/doi/10.1103/PhysRevD.25.2794.

[109] S. Barish et al. "Updated Charged-Particle Multiplicity Distribution from 205 GeV/c Proton-Proton Interactions". In: *Phys. Rev. D* 9 (1974), p. 2689. DOI: 10.1103/PhysRevD.9.2689.

[110] A. Firestone et al. "pp Interactions at 300 GeV/c: Measurement of the Charged Multiplicity, Total and Elastic Cross-Sections". In: *Phys. Rev. D* 10 (1974), p. 2080. DOI: 10.1103/PhysRevD.10.2080.

[111] EHS-RCBC collaboration, J. L. Bailly et al. "Topological Cross-sections and Charged Particle Multiplicities in pp Interactions at 360-GeV/c". In: *Z. Phys. C* 23 (1984), p. 205. DOI: 10.1007/BF01546186.

[112] NA61/SHINE collaboration, N. Abgrall et al. "Measurement of negatively charged pion spectra in inelastic p+p interactions at p_{lab} = 20, 31, 40, 80 and 158 GeV/c". In: *Eur. Phys. J. C* 74.3 (2014), p. 2794. DOI: 10.1140/epjc/s10052-014-2794-6. arXiv: 1310.2417 [hep-ex].

[113] NA61/SHINE collaboration, A. Aduszkiewicz et al. "Measurements of $\pi^{\pm}$, $K^{\pm}$, p and $\bar{p}$ spectra in proton-proton interactions at 20, 31, 40, 80 and 158 GeV/c with the NA61/SHINE spectrometer at the CERN SPS". In: *Eur. Phys. J. C* 77.10 (2017), p. 671. DOI: 10.1140/epjc/s10052-017-5260-4. arXiv: 1705.02467 [nucl-ex].

[114] M. Gazdzicki and D. Roehrich. "Pion multiplicity in nuclear collisions". In: *Z. Phys. C* 65 (1995), pp. 215–223. DOI: 10.1007/BF01571878.

[115] Ingrid Kraus. "Hyperonenproduktion in C+C- und Si+Si-Kollisionen bei 158 GeV pro Nukleon". Frankfurt U., 2004. URL: https://cds.cern.ch/record/1289145.

[116] NA49 collaboration, C. Alt et al. "System-size dependence of strangeness production in nucleus-nucleus collisions at $\sqrt{s_{NN}}$ = 17.3 GeV". In: *Phys. Rev. Lett.* 94 (2005), p. 052301. DOI: 10.1103/PhysRevLett.94.052301. arXiv: nucl-ex/0406031.

[117] HADES collaboration, G. Agakishiev et al. "Hyperon production in Ar+KCl collisions at 1.76A GeV". In: *Eur. Phys. J. A* 47 (2011), p. 21. DOI: 10.1140/epja/i2011-11021-8. arXiv: 1010.1675 [nucl-ex].

[118] HADES collaboration, G. Agakishiev et al. "Phi decay: A Relevant source for K- production at SIS energies?" In: *Phys. Rev. C* 80 (2009), p. 025209. DOI: 10.1103/PhysRevC.80.025209. arXiv: 0902.3487 [nucl-ex].

[119] HADES collaboration, P. Tlusty et al. "Charged pion production in C+C and Ar+KCl collisions measured with HADES". In: *47th International Winter Meeting on Nuclear Physics*. June 2009. arXiv: 0906.2309 [nucl-ex].

[120] HADES collaboration, J. Adamczewski-Musch et al. "Sub-threshold production of K^0_S mesons and Λ hyperons in Au+Au collisions at $\sqrt{s_{NN}} = 2.4$ GeV". In: *Phys. Lett. B* 793 (2019), pp. 457–463. DOI: 10.1016/j.physletb.2019.03.065. arXiv: 1812.07304 [nucl-ex].

[121] STAR collaboration. "Strangeness Production in $\sqrt{s_{\rm NN}} = 3$ GeV Au+Au Collisions at RHIC". July 2024. arXiv: 2407.10110 [nucl-ex].

[122] E895 collaboration, C. Pinkenburg et al. "Production and collective behavior of strange particles in Au + Au collisions at 2 A GeV – 8 A GeV". In: *Nucl. Phys. A* 698 (2002). Ed. by T. J. Hallman et al., pp. 495–498. DOI: 10.1016/S0375-9474(01)01412-9. arXiv: nucl-ex/0104025.

[123] S. Ahmad et al. "Lambda production by 11.6-A/GeV/c Au beam on Au target". In: *Phys. Lett. B* 382 (1996). [Erratum: Phys.Lett.B 386, 496–496 (1996)], pp. 35–39. DOI: 10.1016/0370-2693(96)00642-9.

[124] S. Albergo et al. "Λ spectra in 11.6 A GeV/c Au Au collisions". In: *Phys. Rev. Lett.* 88 (2002), p. 062301. DOI: 10.1103/PhysRevLett.88.062301.

[125] STAR collaboration, Jaroslav Adam et al. "Strange hadron production in Au+Au collisions at $\sqrt{s_{\rm NN}} = 7.7$, 11.5, 19.6, 27, and 39 GeV". In: *Phys. Rev. C* 102.3 (2020), p. 034909. DOI: 10.1103/PhysRevC.102.034909. arXiv: 1906.03732 [nucl-ex].

[126] STAR collaboration, M. M. Aggarwal et al. "Strange and Multi-strange Particle Production in Au+Au Collisions at $\sqrt{s_{NN}} = 62.4$ GeV". In: *Phys. Rev. C* 83 (2011). [Erratum: Phys.Rev.C 107, 049903 (2023)], p. 024901. DOI: 10.1103/PhysRevC.83.024901. arXiv: 1010.0142 [nucl-ex].

[127] STAR collaboration, C. Adler et al. "Midrapidity Λ and $\bar{\Lambda}$ production in Au + Au collisions at $\sqrt{s_{NN}} = 130$ GeV". In: *Phys. Rev. Lett.* 89 (2002), p. 092301. DOI: 10.1103/PhysRevLett.89.092301. arXiv: nucl-ex/0203016.

[128] PHENIX collaboration, K. Adcox et al. "Measurement of the Λ and $\bar{\Lambda}$ particles in Au+Au collisions at $\sqrt{s_{NN}} = 130$ GeV". In: *Phys. Rev. Lett.* 89 (2002), p. 092302. DOI: 10.1103/PhysRevLett.89.092302. arXiv: nucl-ex/0204007.

[129] STAR collaboration, J. Adams et al. "Scaling Properties of Hyperon Production in Au+Au Collisions at $\sqrt{s_{NN}}$ = 200 GeV". In: *Phys. Rev. Lett.* 98 (2007), p. 062301. DOI: 10.1103/PhysRevLett.98.062301. arXiv: nucl-ex/0606014.

[130] E-802 collaboration, L. Ahle et al. "Kaon production in Au+Au collisions at 11.6 AGeV/c". In: *Phys. Rev. C* 58 (1998), pp. 3523–3538. DOI: 10.1103/PhysRevC.58.3523.

[131] HADES collaboration, J. Adamczewski-Musch et al. "Charged-pion production in Au+Au collisions at $\sqrt{s_{NN}} = 2.4\ GeV$: HADES Collaboration". In: *Eur. Phys. J. A* 56.10 (2020), p. 259. DOI: 10.1140/epja/s10050-020-00237-2. arXiv: 2005.08774 [nucl-ex].

[132] Benjamin Noah Kimelman. "Baryon Stopping and Charged Hadron Production in Au+Au Fixed-Target Collisions at $\sqrt{s_{NN}}$ = 3.0 GeV at STAR". PhD thesis. 2022. URL: http://nuclear.ucdavis.edu/thesis/Kimelman_Dissertation_Final.pdf.

[133] E-895 collaboration, J. L. Klay et al. "Charged pion production in 2 to 8 A GeV central Au+Au collisions". In: *Phys. Rev. C* 68 (2003), p. 054905. DOI: 10.1103/PhysRevC.68.054905. arXiv: nucl-ex/0306033.

[134] E-802 collaboration, L. Ahle et al. "Particle production at high baryon density in central Au+Au reactions at 11.6A GeV/c". In: *Phys. Rev. C* 57.2 (1998), R466–R470. DOI: 10.1103/PhysRevC.57.R466.

[135] STAR collaboration, L. Adamczyk et al. "Bulk Properties of the Medium Produced in Relativistic Heavy-Ion Collisions from the Beam Energy Scan Program". In: *Phys. Rev. C* 96.4 (2017), p. 044904. DOI: 10.1103/PhysRevC.96.044904. arXiv: 1701.07065 [nucl-ex].

[136] STAR collaboration, C. Adler et al. "Kaon production and kaon to pion ratio in Au+Au collisions at $\sqrt{s_{NN}}$ = 130 GeV". In: *Phys. Lett. B* 595 (2004), pp. 143–150. DOI: 10.1016/j.physletb.2004.06.044. arXiv: nucl-ex/0206008.

[137] PHENIX collaboration, K. Adcox et al. "Centrality dependence of $\pi^{\pm}$, $K^{\pm}$, p and $\bar{p}$ production from $\sqrt{s_{NN}}$ = 13 GeV Au+Au collisions at RHIC". In: *Phys. Rev. Lett.* 88 (2002), p. 242301. DOI: 10.1103/PhysRevLett.88.242301. arXiv: nucl-ex/0112006.

[138] STAR collaboration, J. Adams et al. "Identified particle distributions in pp and Au+Au collisions at $\sqrt{s_{NN}}$ = 200 GeV". In: *Phys. Rev. Lett.* 92 (2004), p. 112301. DOI: 10.1103/PhysRevLett.92.112301. arXiv: nucl-ex/0310004.

[139] C. Blume and C. Markert. "Strange hadron production in heavy ion collisions from SPS to RHIC". In: *Prog. Part. Nucl. Phys.* 66 (2011), pp. 834–879. DOI: 10.1016/j.ppnp.2011.05.001. arXiv: 1105.2798 [nucl-ex].

[140] NA49 collaboration, C. Alt et al. "Energy dependence of Λ and Ξ production in central Pb+Pb collisions at 20A, 30A, 40A, 80A, and 158A GeV measured at the CERN Super Proton Synchrotron". In: *Phys. Rev. C* 78 (2008), p. 034918. DOI: 10.1103/PhysRevC.78.034918. arXiv: 0804.3770 [nucl-ex].

[141] NA57 collaboration, F. Antinori et al. "Energy dependence of hyperon production in nucleus nucleus collisions at SPS". In: *Phys. Lett. B* 595 (2004), pp. 68–74. DOI: 10.1016/j.physletb.2004.05.025. arXiv: nucl-ex/0403022.

[142] NA49 collaboration, S. V. Afanasiev et al. "Energy dependence of pion and kaon production in central Pb + Pb collisions". In: *Phys. Rev. C* 66 (2002), p. 054902. DOI: 10.1103/PhysRevC.66.054902. arXiv: nucl-ex/0205002.

[143] J. Bartke. *Introduction to Relativistic Heavy Ion Physics*. World Scientific, 2009.

[144] W. Florkowski. *Phenomenology of Ultra-Relativistic Heavy-Ion Collisions*. World Scientific, 2010.

[145] NA61/SHINE collaboration, M. Gazdzicki. *Addendum to the NA61/SHINE Proposal: Request for oxygen beam in Run 3*. Tech. rep. Geneva: CERN, 2022. URL: https://cds.cern.ch/record/2810689.

[146] NA61/SHINE collaboration, M. Mackowiak-Pawlowska. *Addendum to the NA61/SHINE Proposal: Request for light ions beams in Run 4*. Tech. rep. Geneva: CERN, 2023. URL: https://cds.cern.ch/record/2867952.

[147] J-PARC-HI collaboration, Takao Sakaguchi. "High density matter physics at J-PARC-HI". In: *PoS* CORFU2018 (2019). Ed. by Konstantinos Anagnostopoulos et al., p. 189. DOI: 10.22323/1.347.0189. arXiv: 1904.12821 [nucl-ex].

[148] CBM collaboration, Kshitij Agarwal. "The compressed baryonic matter (CBM) experiment at FAIR—physics, status and prospects". In: *Phys. Scripta* 98.3 (2023), p. 034006. DOI: 10.1088/1402-4896/acbca7.

List of Figures

List of Tables